The H1 First Level Fast Track Trigger

by

Y. H. Fleming

Thesis submitted for a degree of
Doctor of Philosophy

School of Physics and Astronomy
The University of Birmingham
September 2003

Abstract

The HERA collider has recently been upgraded to produce a factor of approximately 5 more luminosity. In parallel, upgrades to the H1 detector and trigger have been necessary. One of the projects was the design of an improved Fast Track Trigger (FTT) which should replace the old track trigger and is based on the central drift chambers of the H1 experiment. This work describes the design and expected performance of the FTT. Special emphasis is put on the design of a fast pipelined track segment finding algorithm which is the heart of the first level of the trigger. With the FTT having been designed to perform online particle identification for the first time at H1, the triggering on exclusive final state particles is possible. The expected performance for exclusive vector meson production is investigated here. It is shown that the FTT is able to reconstruct diffractive J/ψ events in photoproduction with an efficiency of 94% with acceptable trigger rates. Diffractive ρ^0 electroproduction events with a four-momentum transfer squared, $t = -15$ GeV^2, can be triggered with an efficiency of 72% with acceptable trigger rates. Finally, the expected trigger performance of charged current events is investigated here. It is shown that the use of additional FTT tracking information allows a rate reduction of a factor of 5 for the present charged current triggers if a minor acceptable loss in efficiency with respect to the HERA I efficiency is taken into account. It is further shown, that a re-designed trigger built specifically to select charged current events with a low missing transverse momentum between 12 and 15 GeV is possible at an acceptable trigger rate.

A Note on the Author's Contribution

Whilst this thesis has entirely been written by myself, and the work presented herein is my own, I received invaluable input from several people from the H1 Collaboration. Here, I would like to acknowledge specific contributions from a number of people.

Although the track segment finding algorithm was implemented by myself, the algorithm design was performed in collaboration with Dr. André Schöning. Furthermore, the design and implementation of the L1 linker algorithm presented in this thesis has been developed by Dr. André Schöning and the programming of the algorithms run on the "back FPGA" is currently being performed by Raphael Baldinger.

The FTT performance studies described in chapter 5 as well as the vector meson and charged current trigger studies described in chapters 6 and 7 respectively were entirely done by myself. For the ρ^0 and J/ψ analysis, I would like to thank Olaf Behrendt for providing me with his code to read out the Spacal trigger information. I would also like thank Ethan Woehrling for providing me with a sample of selected Neutral Current data events. This data sample is used in chapters 5 and 7.

I am also grateful to Dr. Paul Newman, Dr. Ian Kenyon, Dr. Paul Thompson, Dr. André Schöning and Dr. Eram Rizvi for proof-reading all or part of this thesis and for making many helpful suggestions.

A Note on Units

In this work, a system of natural units will be used, whereby $\hbar = c = 1$. Hence, energies, momenta and masses are quoted in GeV.

Between October 1999 and September 2002, this work was supported financially by the UK Particle Physics and Astronomy Research Council, P.P.A.R.C. (tuition fees) and the University of Birmingham. Between October 2002 and January 2003, further financial support was provided by the H.E.P. Group in Birmingham as well as the Caroline Harrold Fund.

Contents

1 HERA Physics **3**

1.1 Introduction 3

1.2 Deep-Inelastic Scattering 3

1.2.1 Kinematics 3

1.2.2 The Quark Parton Model 5

1.3 Deep Inelastic Scattering Cross-Section 6

1.4 Quantum Chromodynamics 8

1.4.1 The QPM and Bjorken Scaling 8

1.4.2 Quantum Chromodynamics 10

1.5 QCD Evolution 10

1.5.1 The DGLAP Evolution Mechanism 11

1.5.2 The BFKL Evolution Mechanism 12

1.6 Photoproduction 13

1.7 The Gluon Density of the Proton 13

1.8 Diffractive Vector Meson Production at HERA 14

1.9 Decay Modes of ρ^0 and J/ψ Vector Mesons 19

1.10 Summary 20

2 The H1 Experiment at HERA **22**

2.1 Introduction 22

2.2 The HERA Storage Ring 22
2.3 The HERA II Luminosity Upgrade 23
2.4 The H1 Detector 24
2.5 Tracking at H1 26
2.5.1 The Central Tracking Detector 28
2.5.2 The Central Proportional Chambers 29
2.5.3 The Forward Tracking Detector 30
2.5.4 The Backward Proportional Chamber 30
2.6 Calorimetry 30
2.6.1 The Liquid Argon Calorimeter 30
2.6.2 The Spaghetti Calorimeter 32
2.6.3 The PLUG Calorimeter 32
2.7 Muon Detection 33
2.7.1 The Central Muon Detector 33
2.7.2 The Forward Muon Detector 33
2.8 Time of Flight Detectors 33
2.9 The H1 Luminosity system 34
2.10 The H1 Trigger System 34
2.10.1 Level 1 35
2.10.2 Level 2 36
2.10.3 Level 3 36
2.10.4 Event Filtering and Online Reconstruction 37
2.10.5 Prescale Factors 37

3 The Fast Track Trigger 38

3.1 Introduction 38
3.2 Motivation for the Fast Track Trigger 38

3.3 Basic Principle of the Fast Track Trigger 39
3.4 The FTT Hardware 41
3.5 Principal Algorithms at L1 45
3.5.1 Q-t Analysis 45
3.5.2 The Track Segment Linking at L1 46
3.6 Definition of the FTT-L2 Tracks 49

4 The Track Segment Finding Algorithm 50
4.1 Introduction 50
4.2 Devices and Technologies 50
4.2.1 Field Programmable Gate Arrays 50
4.2.2 Content Addressable Memories 51
4.2.3 Shift Registers 51
4.3 Description of Algorithm 52
4.3.1 The Pre-L1Keep Phase 53
4.3.2 The Post-L1Keep Phase 55
4.4 Generation of Valid Track Segment Masks 57
4.5 Required Resources 59
4.5.1 Resources on Front FPGA 59
4.5.2 Resources on Back FPGA 61
4.6 The Main Control Unit of the Track Segment Finder 61
4.7 The Timing of the L1 Trigger Chain 64
4.8 Timing of the Track Segment Finder during the Post-L1Keep Phase 66
4.9 Summary 67

5 Simulated FTT Performance Studies 68
5.1 Introduction 68

5.2 Monte-Carlo Simulation 68
5.2.1 Monte-Carlo Event Generators 68
5.2.2 Detector Simulation 69
5.3 FTT Track Resolutions 69
5.3.1 Level 1 Track Resolutions 69
5.3.2 Level 2 Track Resolutions 72
5.3.3 Performance of L1 Linker 72
5.4 FTT Track Efficiencies and Purities 76
5.4.1 L1 Track Efficiency 76
5.4.2 L2 Track Efficiency and Purity 76
5.5 The FTT T0 Trigger Element 82
5.6 Summary 84

6 A Study to Trigger Low Multiplicity Processes with the FTT 87

6.1 Introduction 87
6.2 Considerations for Developing a New Trigger 87
6.3 Determination of the Trigger Efficiency and Evaluation of its Rate 88
6.4 Kinematic Reconstruction Methods 89
6.5 Reconstruction of the Invariant Mass and Mandelstam $|t|$ 90
6.6 Triggering J/ψ Events with the FTT 90
6.6.1 The Final Trigger Algorithm 93
6.6.2 Trigger Efficiency 95
6.6.3 Trigger Rates 95
6.6.4 Conclusion 97
6.7 Triggering ρ^0 Mesons in Electro-production 99
6.7.1 Reconstruction of the Invariant Mass 101
6.7.2 Reconstruction of Mandelstam $|t|$ 101

6.7.3 Trigger Efficiency 104
6.7.4 The Trigger Rates 107
6.7.5 Conclusion 108
6.8 Summary 108

7 The Design of a New Charged Current Trigger for the H1 Experiment 109
7.1 Introduction 109
7.2 The Charged Current Sub-Triggers 109
7.2.1 Trigger Elements used to Trigger CC Events at HERA I 110
7.3 Triggering Charged Current Events at HERA II 112
7.3.1 Trigger Efficiencies for Appropriate Cut Variables 112
7.3.2 Rate Reductions of Sub-Triggers ST66 and ST77 115
7.3.3 Conclusion 118
7.4 A Redesigned Low P_t^{miss} Trigger 119
7.4.1 Conclusion 125
7.5 Summary 126

A The Main Control unit of the Track Segment Finder 128
A.1 VHDL programming 128
A.2 The Program 128

List of Figures

1.1 A Feynman diagram of a NC DIS event together with the main kinematic variables is shown in (a). A generic CC process is illustrated in (b). 4

1.2 Schematic diagram of an ep interaction in the Quark Parton Model. 5

1.3 The NC (circles) and CC (squares) cross-sections are shown as a function of Q^2 for e^+p and e^-p scattering. 8

1.4 The proton structure function F_2 is shown as a function of Q^2. The solid points show the 94-00 e^+p data from H1, whereas the open points show previously published low Q^2 data. 9

1.5 Diagram of QCD splitting functions $P_{qq}(x/y)$ in (a) and $P_{qg}(x,y)$ in (b). In figure (a), the quark with momentum y splits into a gluon and a quark with momentum x, the latter of which interacts with the photon. In figure (b), the gluon with momentum y splits into a quark with momentum x and a non-interacting quark. 11

1.6 A parton ladder diagram contributing to the structure function $F_2(x,Q^2)$ at low x is shown in (a). In the DGLAP regime, the partons are ordered in transverse momentum, k_T, whereas in the BFKL evolution scheme the gluons are ordered in x. The equations are formed by summing the squared amplitudes as illustrated in (b). 12

1.7 The extracted gluon distribution from the inclusive F_2 measurement is shown as a function of x for different values of Q^2. 14

1.8 The leading order boson-gluon fusion process for heavy quark production is shown in the case of charm production. Whereas the direct process involves the photon interacting in a point-like way in (a), the gluon originating from the photon interacts with the proton in the resolved case shown in (b). . . 15

1.9 The gluon density of the proton determined from the measurement of the $D^\star$ cross-section in DIS and photo-production is shown. 15

1.10 Diffractive vector meson production at HERA. The Mandelstam variable t is the energy transferred at the proton vertex. In the elastic regime, the proton remains intact whereas in the inelastic regime the proton breaks up into the final state Y. 16

1.11 Overview of the photon-proton cross-section compared to the cross-section of the different vector meson particles measured at HERA. All cross-sections are shown with respect to the hadronic mass $W_{\gamma p}$. 17

1.12 The elastic ρ cross-section ($\gamma^* p \to \rho^0 p$) is plotted as a function of $W_{\gamma p}$ for different values of Q^2. 18

1.13 The measured diffractive J/ψ cross-section σ in the kinematic range $50 < W < 150$ GeV is shown as a function of the Mandelstam variable W. . . . 18

1.14 Strong decay of ρ^0 vector meson to $\pi^+\pi^-$ pair. 19

1.15 The two decay modes of the J/ψ vector meson are shown: (a) the strong decay into three pions as well as (b) the electromagnetic decay into two leptons. 20

2.1 The HERA accelerator and its pre-accelerator, PETRA. 23

2.2 Side view of the H1 detector. 25

2.3 Side view of the H1 tracking system 27

2.4 The CIP is used together with the COP to reconstruct tracks originating from the nominal vertex. 29

2.5 Side view of the LAr calorimeter in the $y-z$ plane. Only the upper part of the LAr calorimeter is shown as the detector is symmetric about the z-axis. 31

2.6 Side view of the Spacal detector in the $y-z$ plane. 32

2.7 ToF system after the upgrade 2000. 34

2.8 Top view of the H1 luminosity system after the upgrade 2000. 35

2.9 The H1 trigger concept. 35

3.1 CJC $r-\phi$ projection, showing the 4 trigger layers. 39

3.2 Projection in $r-\phi$, showing the 3 trigger layers in CJC1. 40

3.3 The FTT concept is based on a three level trigger system. 41

3.4 The hardware layout of the FTT. 42

3.5 Schematic drawing of the Front End Module. 43

3.6 The FTT-L3 trigger system. 44

3.7 Figure (a) shows the digitised pulses from each end of a drift wire. Figure (b) shows the DOS signal after the summing of both digitised signals. . . . 45

3.8 The determination of the z-coordinate through charge division. With the z-co-ordinate closer to the positive end of the wire, the amplitude of the charge arriving at the positive side of the wire is larger tan the one arriving at the side of the wire. 46

3.9 Flow diagram of the L1 linking algorithm. 47

3.10 Definition of the FTT-L2 track parameters. 49

4.1 The above figure shows (a) the unencoded and (b) the encoded modes of the CAM search functions. In the unencoded mode, the CAM output is composed of a series of bits where each bit corresponds to a specific row. The bit is set if the input word was found in its corresponding row. In the encoded mode, the address of the matches that are found are sent out in series. The CAM search starts at position 0 and stops at position 31. . . . 52

4.2 Overview of the track segment finding algorithm. 53

4.3 Hits emerging from two different space points which are equidistant from the trigger wire have exactly the same drift time. 54

4.4 The generation of valid track segments is performed by checking all possible track segment masks for their validity. The sampling of the drift times is done at 20, 80 as well as 320 MHz. 58

4.5 In figure (a), valid track segment combinations stored in the upper half of the CAM should be identified. The high input pattern is composed of selected sections from the three relevant shift registers and the low input pattern is composed of a series of '1's. As more than a single valid track segment may be identified, "don't care" bits, pictured as 'X', are used instead of '0's in the stored track segment patterns inside the CAMs. As the "don't care" bits accept '1's or '0's as a valid input, the low input pattern would automatically validate all unencoded output bits. Hence, the high input pattern decides which one of the 32 output bits is validated. In figure (b), the process is similar to the process shown in figure (a) except that valid track segment combinations stored in the lower half of the CAM should be identified in this case. Here, the low input pattern decides which one of the 32 output bits is validated. 60

4.6 This figure shows a flow diagram of the track-segment finding algorithm. Each of the different boxes illustrates a particular control unit. 62

4.7 The control unit of the track segment finder uses the incoming control signals 'PiEn', 'FClr_N' and 'busy' to determine the sequence of states. The 10.4 MHz HERA clock as well as the HERA clock (Clk10), which is synchronised to the 83.2 MHz clock (Clk80), is shown. The outgoing 'Status' bits are used by the track segment finding algorithm to switch tasks if necessary. 65

5.1 The $\frac{1}{p_T}$ resolution of tracks from NC events are shown in different bins of p_T. 70

5.2 The L1 resolutions in the ϕ coordinate are shown for (a) $\gamma p \rightarrow J/\psi\, p$ data sample as well as (b) for NC events. 71

5.3 L2 resolutions of the parameters (a) θ, (b) $\frac{1}{p_T}$ and (c) ϕ of the FTT reconstructed tracks relative to the offline reconstructed tracks are shown for the elastic $J/\psi \rightarrow \mu^+\mu^-$ photo-production sample. 73

5.4 L2 resolutions of the parameters (a) θ, (b) $\frac{1}{p_T}$ and (c) ϕ of the FTT reconstructed tracks relative to the offline reconstructed tracks are shown for the CC data sample. 74

5.5 The fraction of offline reconstructed tracks associated to FTT reconstructed L1 tracks with the same curvature sign (dots) as well as the fraction of offline reconstructed tracks associated to L1 tracks with the opposite curvature sign (triangles) are shown as a function of the p_T of the associated offline track. 75

5.6 The L1 track efficiency is shown as a function of the offline transverse momentum. 77

5.7 The L2 track finding efficiencies are shown as a function of the track parameters (a) θ, (b) p_T and (c) ϕ for low multiplicity events. 78

5.8 The L2 track purities are shown as a function of the track parameters (a) θ, (b) p_T and (c) ϕ for low multiplicity events. 79

5.9 The L2 track finding efficiencies are shown as a function of the track parameters (a) θ, (b) p_T and (c) ϕ for high multiplicity events. 80

5.10 The L2 track purities are shown as a function of the track parameters (a) θ, (b) p_T and (c) ϕ for high multiplicity events. 81

5.11 (a) The track finding efficiency and (b) the efficiency to find the electron track are shown as a function of the offline track multiplicity in the event. A data sample of selected NC events, that were triggered by the independent LAr Calorimeter based monitor trigger, was used. 82

5.12 (a) The number of FTT reconstructed tracks and (b) the number of offline tracks also found by the FTT, shown against the number of offline reconstructed tracks in the acceptance region of the FTT. 83

5.13 Ratio of tracks with negative and positive track curvature shown as a function of the offline reconstructed p_T. 83

5.14 The number of events with a t_0 validated track is shown as a function of the Bunch Crossing relative to the nominal one in the cases of (a) the ρ^0 MC sample, (b) the selected NC data sample and (c) the selected CC data sample. If an event incorporates several tracks each of which is t_0 validated for a different bunch crossing, the event enters the bunch crossing bin where the first t_0 validated track was found. 85

5.15 The efficiency to obtain a t_0 validation of an event in the nominal bunch crossing is shown against the track parameter p_T for the low multiplicity process $\gamma^\star p \to \rho^0\ Y$. The proton-dissociative ρ^0 MC was used. 86

6.1 Number of tracks reconstructed by the FTT at L1 in $\gamma p \to J/\psi\ p$ events. . 92

6.2 Number of tracks reconstructed by the FTT at L2 in $\gamma p \to J/\psi\ p$ events. . 92

6.3 The invariant J/ψ mass reconstructed from the two muons at the FTT-L3 trigger level as well as offline. 93

6.4 The difference between the generated and reconstructed J/ψ mass is shown. The dots represent the offline reconstructed mass difference and the triangles represent the FTT reconstructed mass difference. 94

6.5 The reconstructed Mandelstam variable t is compared to the generated one in both the FTT reconstruction (triangles) and the offline reconstruction (dots). 94

6.6 The trigger efficiency of the algorithm searching for elastic J/ψ events in photo-production as a function of the Mandelstam variable $-t_{offline}$. . . . 96

6.7 The trigger efficiency of the algorithm searching for elastic J/ψ events in photo-production as a function of Mandelstam $|t|$ as measured offline if the cut $-t_{FTT} > 0.1$ is applied on trigger level. 96

6.8 L3 Rate of FTT validated sub-trigger ST15 as a function of $p^{cut}_{T,\ FTT}$. 97

6.9 L3 Rate of FTT validated sub-trigger ST15 as a function of $\Delta M_{cut,\ FTT}$. . 98

6.10 L3 Rate of FTT validated sub-trigger ST15 as a function of $t_{cut,\ FTT}$. . . . 98

6.11 Proton-dissociative $\rho^0 \to \pi^+\pi^-$ tracks reconstructed by the FTT at L1. . . 100

6.12 The number of $\rho \rightarrow \pi^+\pi^-$ tracks reconstructed by the FTT at L2. The ρ^0 Monte-Carlo selection was used for this study. 100

6.13 The FTT reconstructed invariant mass of the ρ^0 meson in electro-production. The elastic electro-production MC was used. 101

6.14 The electron track is reconstructed using the position of the hit cluster in the Spacal. The track is assumed to originate from the nominal vertex position in the H1 coordinate system. 102

6.15 The resolution on the reconstructed Mandelstam variable t was investigated using the elastic ρ^0 Monte-Carlo in electro-production. 103

6.16 The resolution on the reconstructed Mandelstam variable t was investigated using the proton-dissociative ρ^0 Monte-Carlo in electro-production. 104

6.17 Trigger efficiency of the algorithm searching for proton dissociative ρ^0 vector mesons as a function of $-t_{offline}$. The algorithm required exactly two tracks to perform the search. 105

6.18 Trigger efficiency of the algorithm searching for proton dissociative ρ^0 vector mesons as a function of $-t_{offline}$. The algorithm required a minimum of two and a maximum of three tracks to perform the search. 106

6.19 Trigger efficiency of the FTT validated ST0 as a function of $|t_{offline}|$. The algorithm required a minimum of two and a maximum of three tracks to perform the search. A further cut $|t| > 0.2$ GeV^2 was applied in the FTT reconstruction. 106

6.20 L3 Rate of FTT validated Sub-trigger ST0 as a function of $\Delta M_{cut,\ FTT}$. Exactly two FTT reconstructed tracks were required by the trigger algorithm. 107

7.1 Side view of the LAr calorimeter in the $y - z$ plane. Only the upper part of the LAr calorimeter is shown as it is symmetric about the z-axis. The thick lines show the borders of the different big towers 110

7.2 The correlation between the generated missing transverse momentum (V_{gen}) and the missing transverse momentum measured by the FTT (V_{FTT}) is shown for CC events where the hadronic final state is scattered in the central region. 113

7.3 The $V_{ap} - V_p$ phase space is shown for (a) CC events, (b) NC events and (c) photo-production events. 114

7.4 The efficiency of the FTT trigger elements "at least one track found by the FTT" (open circles), $V_{ap} \leq 2$ GeV (triangles) and $V_{ap} \leq 1$ GeV (full circles) is shown as a function of the highest p_T track found in the polar acceptance region of the FTT. 115

7.5 The efficiency of the FTT trigger elements $V_{ap} < 2$ GeV (full circles) and $V_{ap} < 1$ GeV (triangles) is shown as a function of the FTT measured on V_p cut variable. The CC Monte-Carlo was used. 116

7.6 (a) The rate reduction of an FTT validated ST66 is shown as a function of the cut on V_p that is measured by the FTT. (b) The rate reduction of an FTT validated ST77 is shown as a function of the cut on V_p that is measured by the FTT. 117

7.7 Rate reduction of FTT validated charged current sub-triggers ST66 and ST77 as a function of the cut on the highest p_T track as measured by the FTT. 118

7.8 The efficiency of sub-trigger S71 is shown against γ_h (left) and the missing P_T (right). It can be seen that the efficiency is around 40 to 60% at low values of missing P_T. 119

7.9 The trigger efficiency of the LAr_Etmiss trigger element is shown as a function of (a) the offline reconstructed transverse momentum of the hadronic final state P_t^{miss} and (b) the net polar angle of the hadronic final state γ_h. The trigger efficiency is shown for $LAr_Etmiss > 0$ (open circles), $LAr_Etmiss > 1$ (full circles) and $LAr_Etmiss > 2$ (triangles) 120

7.10 The trigger efficiency is shown for the DCRPh_Tc trigger element (open squares), the requirement of finding at least 1 FTT reconstructed track (open circles) and the requirement of finding at least 3 FTT reconstructed tracks (full circles). The trigger efficiency is shown as a function of the cut on the highest p_T track found in the FTT acceptance region. 121

7.11 The trigger efficiency is shown for sub-trigger ST32 (open squares) and for the requirements of at least 3 FTT reconstructed tracks as well as a z-vertex significance peak and the requirement that $V_{ap} \leq 1$ GeV (full circles). The trigger efficiency is shown as a function of the missing transverse momentum P_t^{miss}. 122

7.12 The trigger efficiency is shown as a function of the missing transverse momentum P_t^{miss} for the requirement of finding at least 3 FTT reconstructed tracks as well as a z-vertex significance peak and the requirement that $V_{ap} \leq 1$ GeV in all three cases. Additionally, a V_p cut as well as a cut on the highest p_T track were required. 122

7.13 The rate reduction of the L1 trigger element combination belonging to sub-trigger ST71 due to the Big_T_miss TE (open circles) and the Et_miss> 0 TE (full circles) is shown as a function of the highest p_T track found by the FTT. 123

7.14 The rate of an FTT validated ST77 is shown as a function of the cut on the highest p_T online reconstructed track in the FTT acceptance region. Here, ST77 was used as a monitor trigger. 124

7.15 (a) The rate of the potential redesigned CC sub-trigger is shown as a function of the cut on V_p as measured by the FTT. (b) The corresponding trigger efficiencies are shown as a function of the offline measured missing transverse momentum P_t^{miss} 125

List of Tables

1.1 Overview of the three generations of quarks as defined in the Standard Model. 6

2.1 Comparison of the HERA I and HERA II design parameters. 24

2.2 The main H1 detector components. 26

3.1 CJC wires associated to different trigger layers. 39

4.1 The number of valid masks that are found in the various trigger layers. . . 58

4.2 This table shows the resource usage of all tasks performed by the track segment finding algorithm on the front FPGA in terms of logic elements (LEs) and embedded system blocks (ESBs). 61

4.3 This table shows the time resource usage of all tasks performed by the track segment finding algorithm on the front FPGA. The timing to get the z-information from charge division is not included. 64

4.4 This table shows the time resource usage of all tasks performed by the track segment finding algorithm on the front FPGA. 66

5.1 The above table lists the p_T values of the lower and upper bin edges used to define the L1 linking histogram. 71

6.1 Monitor trigger used for calculating the L3 rate of the FTT. 91

6.2 Cuts performed in order to predict the efficiency of the J/ψ trigger algorithm. 95

6.3 Monitor trigger used for calculating the L3 rate of the FTT. 99

6.4 Cuts performed in order to predict the efficiency and rate of the ρ^0 trigger algorithm. 105

7.1 The main CC sub-triggers at HERA I. 110

7.2 The combination of trigger elements used by sub-trigger ST32. 120

7.3 The trigger levels and the corresponding trigger elements used by the proposed CC trigger are shown above. 125

Introduction

At the beginning of the twentieth century, the general consensus was that the atom was constituted of electrons that flow in positively charged matter as proposed by Thomson [1]. However, when, in the year 1911, Rutherford and his colleges Geiger and Marsden collided α particles with a thin gold foil, they were surprised to see that some of the heavy α particles were heavily deflected [2]. This was contrary to their expectation as only small deflections are allowed if the atom mainly consists of positively charged matter. Thus, Rutherford came to the conclusion, that the force exerted on the α particle was due to a small positively charged nucleus in the centre of the atom. At the same time, he concluded that the nucleus has a size of approximately 10^{-15} m and carries 99.9% of the atom's mass. The nucleus was later understood to be built from protons and neutrons. In 1956, Hofstader [3] found evidence that the protons and neutrons themselves have finite size by studying the scattering of electrons from a hydrogen target.

With higher energies available, experiments at the Stanford Linear Collider (SLAC) showed the first direct evidence for the presence of sub-structure inside the nucleon [4] [5]. The nucleon is probed with a resolution, which is related to the square of the four-momentum transferred, Q^2. It was noticed at SLAC that inelastic scattering showed little dependence on the relevant scale at fixed values of Bjorken-x* other than the $\frac{1}{Q^4}$ propagator term, a property known as scale invariance. This was a sign that there are point-like 'partons' inside the nucleon which were later described as quarks.

It was soon discovered that there were small deviations from the perfect scaling. The theory of Quantum Chromodynamics (QCD) was developed in order to describe the detailed behaviour. In this theory, the interaction between quarks takes place though the exchange of gluons.

With the world's first electron-proton collider, HERA, the theory of QCD can be investigated in more detail. Thus, the recent luminosity upgrade allows for higher statistics at large Q^2 values. Here, effects due to $W^{\pm}$ and Z^0 exchange become visible.

As not only high Q^2 events should be investigated in greater detail but also low x physics where the cross-section is comparatively large, new challenges are posed to the H1 trigger system. Hence, it was decided to improve the trigger system of the H1 experiment for the HERA II running period. One of the projects involved the design and implementation of a new track based trigger in the central region of the H1 detector, the Fast Track Trigger

*In the infinite momentum frame of the proton, Bjorken-x can be thought of as the momentum carried by the struck parton.

(FTT) .

This thesis is concerned with the design and the performance of the Fast Track Trigger. In the first chapter, a theoretical overview of the deep-inelastic scattering process is given. In this chapter, some of the processes for which the FTT will enhance the data yield are described. A motivation for the measurement of the corresponding cross-sections is also included. Next, the HERA accelerator and the H1 detector are described. In the third chapter, a detailed description of the FTT with emphasis on the first trigger level of the FTT is given. The chapter which follows describes the track segment finding algorithm, which is used at the first and second levels, in detail. Here, its speed after the implementation in hardware is assessed. Thereafter, the fifth chapter shows some FTT performance studies. The L1 and L2 resolutions as well as the corresponding track finding efficiencies are presented. The sixth chapter is concerned with improving the trigger efficiencies of current diffractive J/Ψ photo-production triggers as well as ρ^0 triggers using the FTT. The aim was to trigger on ρ^0 proton-dissociative events produced at high $|t|$ in order to investigate overlap between the "soft" regime where the physics processes cannot be calculated perturbatively and "hard" regime. Finally, the seventh chapter presents the trigger efficiencies for charged-current triggers achieved with the help of the FTT, as well as a re-designed low-P_t^{miss} charged-current trigger.

Chapter 1

HERA Physics

1.1 Introduction

Deep inelastic scattering (DIS) has played a vital role in the extension of our knowledge about the structure of matter. Since the lepton is point-like, the structure of a nucleon can be investigated in lepton-nucleon scattering processes. The main goal of the H1 experiment at HERA is to investigate the proton structure. This is done using many different physics channels.

This chapter gives a short overview of the physics that is investigated at HERA. To start with, the kinematics of the deep-inelastic scattering process are explained. Next, a short overview of the cross-sections measured at HERA is presented and their relation to the proton structure functions is briefly described. After that, a short outline of the theory of strong interactions is presented. To set the scene of this thesis, examples of channels for which the FTT will enhance the data yield by a large factor are discussed. This description starts with channels that are used to extract the gluon density in the proton. Thereafter, the underlying dynamics of vector meson production are also discussed.

1.2 Deep-Inelastic Scattering

1.2.1 Kinematics

At HERA, electrons* are collided with protons at high energies in order to study DIS processes. As shown in figure 1.1, the incoming electron e emits an electro-weak gauge boson which is used to probe the structure of the proton p. Depending on the exchanged particle, two kinds of interaction processes can be distinguished.

In the case of a *neutral current* (NC) DIS process, either a photon (γ) or a neutral Z^0 is

*The term "electron" generically refers to both electrons and positrons here.

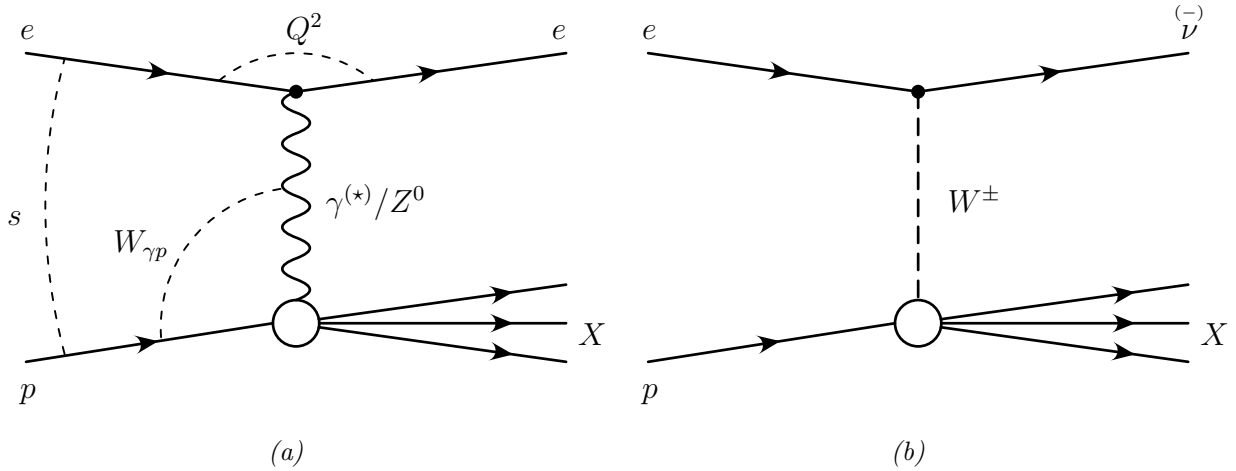

Figure 1.1: A Feynman diagram of a NC DIS event together with the main kinematic variables is shown in (a). A generic CC process is illustrated in (b).

exchanged. The neutral current process is of the form

$$e^{\pm}p \to e^{\pm\prime}X, \tag{1.1}$$

where X corresponds to the final state system of hadronic particles. In the case of a *charged current* (CC) DIS process, the mediator is a charged $W^{\pm}$ boson. CC processes are of the form

$$e^{\pm}p \to \overset{(-)}{\nu}_e X, \tag{1.2}$$

where the $e^{\pm}$ converts into an (anti-)neutrino $\overset{(-)}{\nu}_e$ and X is the hadronic final state. The kinematics of the above processes can be described using combinations of the four-vectors.

In both NC and CC processes, the mediator bosons are propagated with a four-momentum q. The negative square of this transferred gauge boson is given by

$$Q^2 = -q^2, \tag{1.3}$$

where Q^2 is called the *virtuality* of the boson. In the case that Q^2 is much larger than the square of the proton mass m_p^2, the photon is highly virtual and can be used to resolve the constituents of the proton. The centre of mass energy squared of the initial ep system is defined as follows:

$$s = (k + p)^2 \simeq 4E_e E_p, \tag{1.4}$$

where k is the four-momentum of the incoming lepton and p is the four momentum of the incoming proton. The approximation $s = 4E_e E_p$ is appropriate at HERA energies where the mass of the electron and proton are much less than the centre of mass energy. At fixed centre of mass energies $\sqrt{s}$ and ignoring azimuthal degrees of freedom, the kinematics of the scattering process can be completely described in terms of two dimensionless Lorentz invariant variables, usually chosen to be Q^2 and *Bjorken-x*. In the infinite proton momentum frame, Bjorken-x is the fraction of the proton's momentum carried by the interacting quark. It can be calculated from

$$x = \frac{Q^2}{2p \cdot q}. \qquad (0 \leq x \leq 1) \tag{1.5}$$

A further dimensionless variable y, the fractional energy lost by the lepton in the proton rest frame, can be calculated as follows

$$y = \frac{p \cdot q}{p \cdot k}. \qquad (0 \leq y \leq 1) \tag{1.6}$$

The virtuality is related to x and y via

$$Q^2 = x\, y\, s. \tag{1.7}$$

From this relationship it can be deduced that the maximum value of Q^2 at HERA, where the electron and proton beam energies are 27.5 GeV and 920 GeV respectively, is equal to the value of $s = 101200$ GeV^2. The centre of mass energy of the photon-proton system $W_{\gamma p}$ is given by:

$$W^2_{\gamma p} = (p + q)^2. \tag{1.8}$$

It denotes the invariant mass of the hadronic final state and is therefore often called the hadronic mass.

1.2.2 The Quark Parton Model

In the *Quark Parton Model (QPM)*, the proton is considered to consist of non-interacting and point-like *partons*, which can be identified as *quarks*. Figure 1.2 shows a diagram of an interaction process described by the QPM. Here it is assumed that the interaction takes place between a single parton and the electron through the exchange of an electro-weak gauge boson.

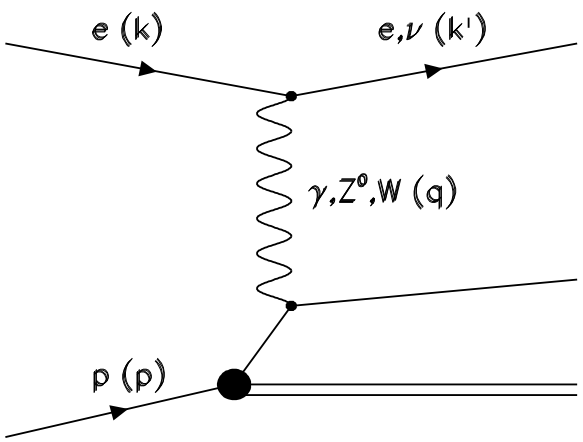

Figure 1.2: Schematic diagram of an *ep* interaction in the Quark Parton Model.

Table 1.1 shows the three generations of quarks that have been identified in the Standard Model. As the proton is a baryon, it is composed of a combination of three quarks, two u quarks and a d quark.

generation	quark	charge	mass
1^{st}	d (down)	-1/3	3 to 9 MeV
	u (up)	2/3	1 to 5 MeV
2^{nd}	s (strange)	-1/3	75 to 175 MeV
	c (charm)	2/3	1.15 to 1.45 GeV
3^{rd}	b (beauty)	-1/3	4 to 4.4 GeV
	t (top)	2/3	174.3 ± 5.1 GeV

Table 1.1: Overview of the three generations of quarks as defined in the Standard Model. The charge and mass definitions are taken from [6].

1.3 Deep Inelastic Scattering Cross-Section

If only electromagnetic interactions are considered, the double differential cross-section for electron-proton scattering is given by the product of a linear combination of two independent structure functions F_1 and F_2 with a propagator term:

$$\frac{\mathrm{d}^2\sigma_{ep}}{\mathrm{d}x\,\mathrm{d}Q^2} = \frac{4\pi\alpha_{em}^2}{x\,Q^4} \cdot [y^2\,x\,F_1 + (1-y)\,F_2], \tag{1.9}$$

where $\alpha_{em} = e^2/4\pi$ is the fine structure constant, F_1 is proportional to the transversely polarised cross-section σ_T and is mediated via transversely polarised photons, and $F_2 \propto \sigma_T + \sigma_L$. These structure functions are related to the (anti-) quark distribution inside the proton. The probability of finding a quark q with a momentum fraction x inside the proton is given by the quark density functions $q(x, Q^2)$ and $\bar{q}(x, Q^2)$. In the QPM, the structure functions $F_1(x, Q^2)$ and $F_2(x, Q^2)$ are built up from the density functions:

$$F_1(x, Q^2) = \frac{1}{2} \cdot \sum_{partons\ q} e_q^2\,[q(x, Q^2) + \bar{q}(x, Q^2)], \tag{1.10}$$

$$F_2(x, Q^2) = x \cdot \sum_{partons\ q} e_q^2\,[q(x, Q^2) + \bar{q}(x, Q^2)], \tag{1.11}$$

where the variable e_q denotes the charge of the partons. From the requirement that the entities struck inside the proton have spin $\frac{1}{2}$, Callan-Gross deduced that $F_2 = 2\,x\,F_1$ [7] as can be seen from equations 1.10 and 1.11. Hence, the cross-section can be re-written as:

$$\frac{\mathrm{d}^2\sigma_{ep}}{\mathrm{d}x\,\mathrm{d}Q^2} = \frac{2\pi\alpha_{em}^2}{x \cdot Q^4} \cdot [(1 + (1-y)^2)\,F_2]. \tag{1.12}$$

At Q^2 values approaching M_Z^2, the contribution from Z^0 boson exchange starts to become important and the double differential NC cross-section for electron-proton scattering $e^{\pm}p \to e^{\pm}X$ is given by:

$$\frac{\mathrm{d}^2\sigma_{NC}}{\mathrm{d}x\,\mathrm{d}Q^2}(e^{\pm}p) = \frac{2\pi\alpha_{em}^2}{x \cdot Q^4} \cdot [Y_+\widetilde{F}_2 \mp Y_- x\widetilde{F}_3], \tag{1.13}$$

where $Y_\pm = 1 \pm (1-y)^2$ is called the helicity factor. The generalised structure function $\widetilde{F}_2$ is an extension of the QED F_2 and can be decomposed as follows:

$$\widetilde{F}_2 \equiv F_2 - v_e\frac{\kappa_w Q^2}{Q^2 + M_Z^2}F_2^{\gamma Z} + (v_e^2 + a_e^2)\left(\frac{\kappa_w Q^2}{Q^2 + M_Z^2}\right)^2 F_2^Z, \tag{1.14}$$

with

$$\kappa_w^{-1} = 4\frac{M_W^2}{M_Z^2}(1 - \frac{M_W^2}{M_Z^2}). \tag{1.15}$$

The quantities v_e and a_e are the respective vector and axial-vector weak couplings of the electron to the Z^0 boson. The contributions from Z^0 boson exchange to the generalised structure functions are described by the F_2^Z function. The resulting γZ interference contributions to $\widetilde{F}_2$ are described by the functions $F_2^{\gamma Z}$. The structure function $\widetilde{F}_3$ consists of the following functions:

$$x\widetilde{F}_3 \equiv -a_e\frac{\kappa_w Q^2}{Q^2 + M_Z^2}xF_3^{\gamma Z} + (2v_e a_e)\left(\frac{\kappa_w Q^2}{Q^2 + M_Z^2}\right)^2 xF_3^Z \tag{1.16}$$

and contains parity violating terms. The contributions due to Z^0 boson exchange to the generalised structure function is described by the F_3^Z function and the γZ interference contribution to $x\widetilde{F}_3$ is described by the function $F_3^{\gamma Z}$. In the QPM, the generalised parity violating structure function $x\widetilde{F}_3$ can be re-written as follows:

$$x \cdot \widetilde{F}_3 \propto x \sum_{partons\ q} [q(x) - \bar{q}(x)]. \tag{1.17}$$

From equation 1.13 and 1.17 it can be deduced that the cross-section becomes sensitive to the valence quark component (i.e. $q - \bar{q}$) in the proton at high values of y.

The CC cross-section starts to become important at large values of Q^2 near the squared mass of the W boson M_W^2. In the simple QPM , the cross-sections may be interpreted as sums of quark and anti-quark densities that depend on the lepton beam charge. Hence the cross-section of the $e^+p \to \bar{\nu}X$ can be written as follows:

$$\frac{\mathrm{d}^2\sigma_{CC}^+}{\mathrm{d}x\ \mathrm{d}Q^2} = \frac{G_F^2}{2\pi x}\left(\frac{M_W^2}{Q^2 + M_W^2}\right)^2 [\bar{u} + \bar{c} + (1 - y)^2(d + s)], \tag{1.18}$$

where u, c, d and s are the quark density functions and G_F is the Fermi constant:

$$G_F = \frac{g^2}{4\sqrt{2}M_W^2} \tag{1.19}$$

with g being the electroweak coupling constant. At high values of x, the d valence quark density makes the dominant contribution to the cross-section. By contrast, in $e^-p \to \nu X$, the cross-section is sensitive to the u valence quark density at high values of x:

$$\frac{\mathrm{d}^2\sigma_{CC}^-}{\mathrm{d}x\ \mathrm{d}Q^2} = \frac{G_F^2}{2\pi}\left(\frac{M_W^2}{Q^2 + M_W^2}\right)^2 [u + c + (1 - y)^2(\bar{d} + \bar{s})]. \tag{1.20}$$

The CC processes are heavily suppressed at low Q^2 values compared with the NC cross-section due to the heavy W boson mass. Figure 1.3 compares the NC and CC cross-sections with the predictions of the Standard Model. At high values of Q^2, the difference between the cross-sections becomes small, which indicates that electro-weak unification is valid in the space-like (HERA) as well as the time-like (LEP) regime.

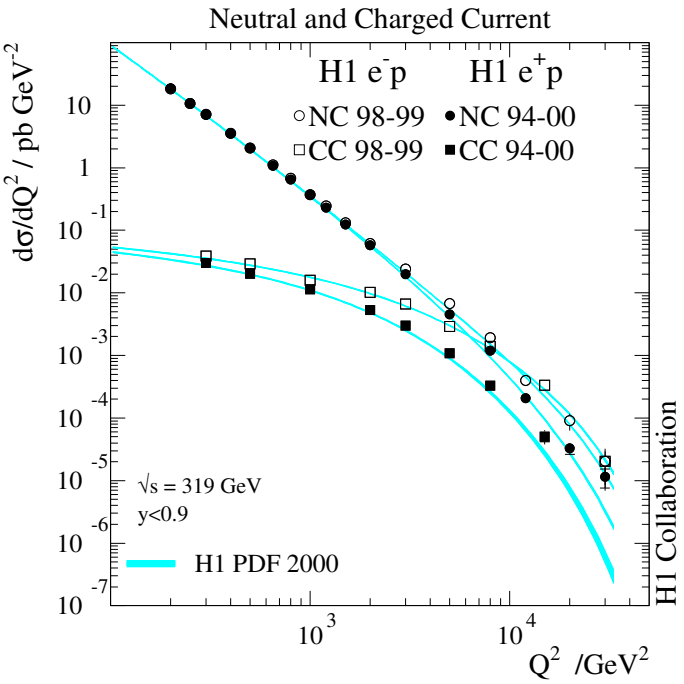

Figure 1.3: The NC (circles) and CC (squares) cross-sections are shown as a function of Q^2 for e^+p and e^-p scattering. The results are compared with the corresponding Standard Model expectations determined from the H1 PDF 2000 fit (error bands) (from [8]).

1.4 Quantum Chromodynamics

1.4.1 The QPM and Bjorken Scaling

In elastic scattering, the Rutherford scattering formula [9] describes a scattering process between two point-like objects. The Rutherford cross-section is not dependent on any unit of length and therefore is said to "scale". Based on the assumption that DIS is a scattering process between a point-like electron and a single constituent of a nucleon, Bjorken predicted in the year 1969 that at large values of Q^2 the structure functions of the DIS cross-sections are independent of the 4-momentum transferred Q^2 [10]. Hence, the structure functions are said to be "scale invariant".

Measurements from early DIS experiments [5] confirmed this statement. However, subsequent fixed target lepton-nucleon experiments [11] found that the structure function F_2 exibited scaling violations. Figure 1.4 shows the structure function F_2 measured by the H1 Collaboration [8]. The structure function is shown for fixed values of x as a function of Q^2. For values of $x \lesssim 0.1$, positive scaling violations are seen whereas for values of $x \gtrsim 0.1$, negative scaling violations are clearly visible. This indicates that quarks in the proton interact with one another.

Based on the initial assumptions of QPM, the sum of the momenta of all three quarks

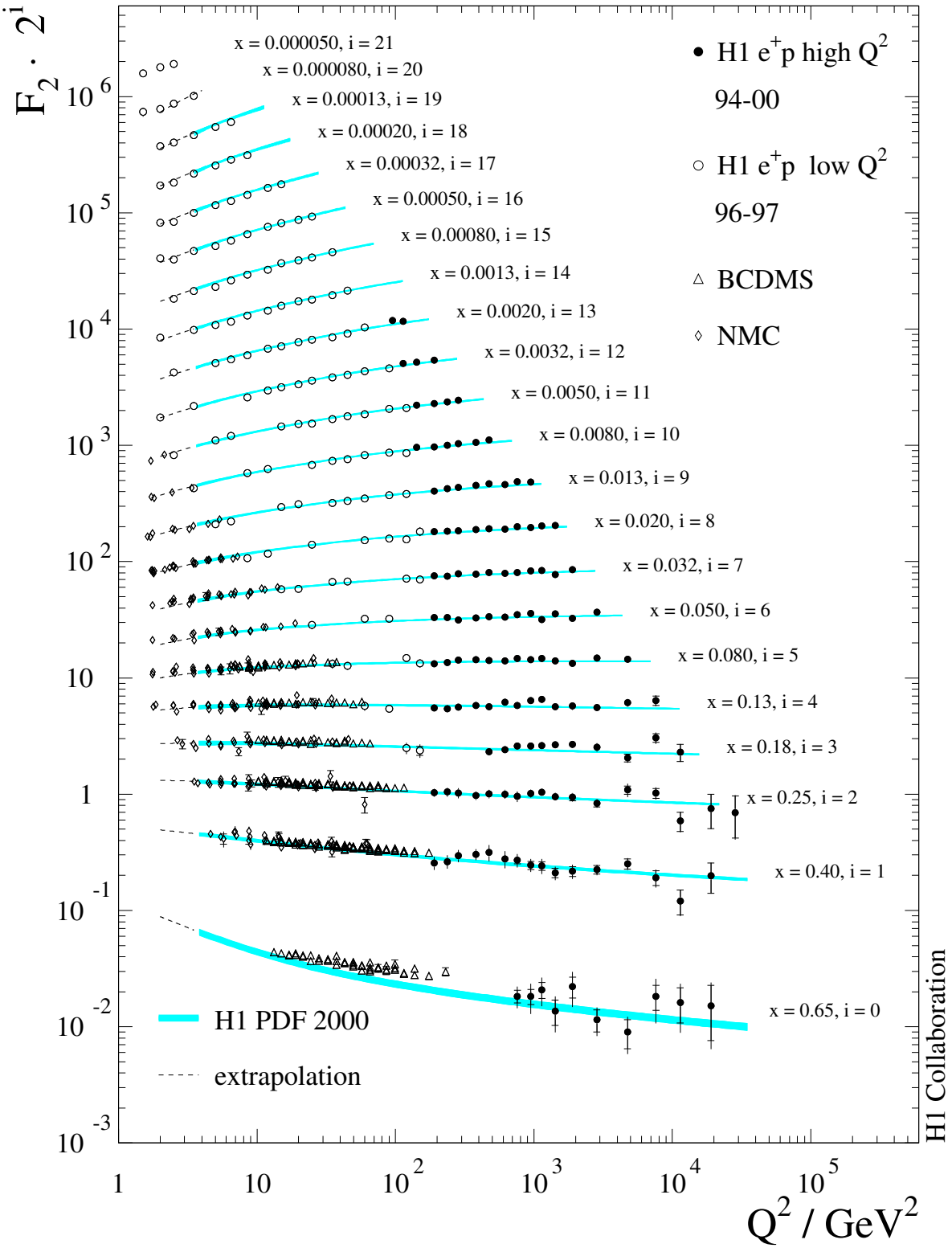

Figure 1.4: The proton structure function F_2 is shown as a function of Q^2. The solid points show the 94-00 e^+p data from H1, whereas the open points show previously published low Q^2 data. The results are compared to the expectation from the Standard Model determined from the H1 PDF 2000 fit (error bands) (from [8]).

should equal that of the proton:

$$\sum_{quarks\ q_i} \int_0^1 \mathrm{d}x\ x \cdot [q_i(x) + \bar{q}_i(x)] = 1 \tag{1.21}$$

Measurements of this sum from the structure functions gave a result of around $\frac{1}{2}$ showing that only approximately half of the proton's momentum was carried by quarks. This was a another observation showing that quarks could not be the only constituents of the proton.

1.4.2 Quantum Chromodynamics

The gauge theory of strong interactions known as *Quantum Chromodynamics* (QCD) is part of the standard model and describes the interaction between quarks and anti-quarks through the exchange of *gluons*.

In an analogous way to the creation of an e^+e^- pair from a photon in QED, the gluon is able to fluctuate into a quark-anti-quark pair. The crucial difference between QED and QCD is that the latter is non-abelian. Thus, the gluon is able to couple to other gluons whereas the photon is not self coupling. Each of the quarks carries an additional quantum number, the *colour charge*. The massless gluons carry combinations of colour and anti-colour and thus gluon exchange will alter the colour charge of a quark. The gluon splittings mean that in addition to the three *valence* quarks from the QPM, the proton contains a sea of quark-anti-quark pairs and gluons. As a consequence, the QPM can be seen as describing the lowest order processes of QCD. The introduction of the gluon leads to a specific dependence of the strong coupling constant α_s on Q^2. At leading order, it is given by:

$$\alpha_s = \frac{12 \cdot \pi}{(33 - 2 \cdot N_f) \cdot \ln(Q^2/\Lambda^2_{QCD})}, \tag{1.22}$$

where N_f is the number of quark flavours with $m_q^2 < Q^2$ and Λ^2_{QCD} is a scale parameter that has to be determined from experiments [12]. As can be seen from equation 1.22, α_s is much smaller than unity at high values of Q^2. Here, quarks can be considered as free, non-interacting particles. This property is generally known as *asymptotic freedom*. As the value of Q^2 decreases and approaches Λ^2_{QCD}, the coupling strength becomes large. As Λ_{QCD} is around 200 MeV, this happens at low values of Q^2. In this situation quarks are tightly bound, which is known as *confinement*. Once α_s is sufficiently below unity, perturbative QCD (pQCD) is effective because the perturbative expansion converges rapidly.

1.5 QCD Evolution

In pQCD where $\alpha_s \ll 1$, a full expansion of a given order n for the evolution of the structure functions with Q^2 would contain terms of order $\alpha_s^n \ln^m(Q^2)$ and $\alpha_s^n \ln^m(1/x)$, where $m \leq n$. However, a full QCD expansion is not manageable. As different terms in the

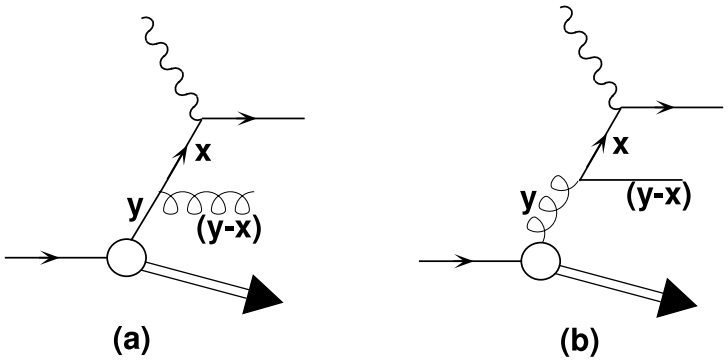

Figure 1.5: Diagram of QCD splitting functions $P_{qq}(x/y)$ in (a) and $P_{qg}(x,y)$ in (b). In figure (a), the quark with momentum y splits into a gluon and a quark with momentum x, the latter of which interacts with the photon. In figure (b), the gluon with momentum y splits into a quark with momentum x and a non-interacting quark.

expansion dominate in different kinematic regions, a number of different approximations and analytic treatments are possible. The dynamics in each case are expressed in terms of evolution equations, relating parton distributions at one point of the kinematic plane to parton distributions at others.

1.5.1 The DGLAP Evolution Mechanism

In the kinematic region of fixed target experiments, the Dokshitzer-Gribov-Lipatov-Altarelli-Parisi (DGLAP) formalism [13] describes the measured cross-sections in this comparatively large x region well.

The DGLAP equation describes the interaction between the quark and the photon with the use of splitting functions, two examples of which are shown in figure 1.5. An iteration of splitting processes is performed such that Feynman diagrams as shown in figure 1.6(a) contribute as well. The sum of all contributions then give the final result. This approach is valid for the case where $\ln(1/x) \ll \ln(Q^2/Q_0^2)$ and powers of $\ln(1/x)$ can be neglected. The reduction of the full expansion to terms in $\alpha_s^n \ln(Q^2/Q_0^2)^n$ is known as the leading log approximation (LLA(Q^2)). The evolution with Q^2 of the quark density functions $q(x,Q^2)$ and the gluon density distribution $g(x,Q^2)$ is given by:

$$\frac{\mathrm{d}q(x,Q^2)}{\mathrm{d}\ln Q^2} = \frac{\alpha_s(Q^2)}{2\pi} \cdot \int_x^1 \frac{dy}{y}[q(x,Q^2) \cdot P_{qq}(\frac{x}{y}) + g(x,Q^2) \cdot P_{qg}(\frac{x}{y})] \tag{1.23}$$

and

$$\frac{\mathrm{d}g(x,Q^2)}{\mathrm{d}\ln Q^2} = \frac{\alpha_s(Q^2)}{2\pi} \cdot \int_x^1 \frac{dy}{y}[q_i(x,Q^2) \cdot P_{gq}(\frac{x}{y}) + g(x,Q^2) \cdot P_{gg}(\frac{x}{y})], \tag{1.24}$$

where P_{ab} are the splitting functions. They give the probability for parton b with momentum fraction y to produce parton a with momentum fraction x. The Feynman diagrams

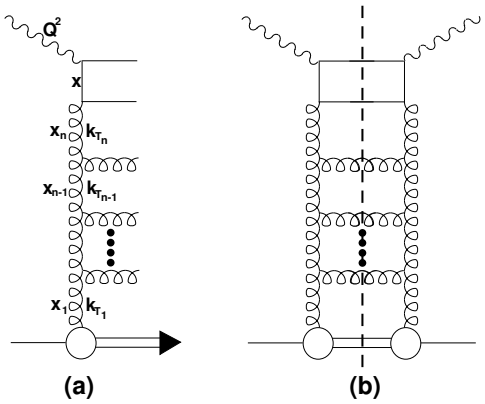

Figure 1.6: A parton ladder diagram contributing to the structure function $F_2(x,Q^2)$ at low x is shown in (a). In the DGLAP regime, the partons are ordered in transverse momentum, k_T, whereas in the BFKL evolution scheme the gluons are ordered in x. The equations are formed by summing the squared amplitudes as illustrated in (b).

corresponding to the two splitting functions P_{qq}, P_{qg} are shown in figure 1.5.

An essential feature of the DGLAP formalism is the strong ordering in transverse momenta:

$$Q^2 \gg k^2_{T,n} \gg k^2_{T,n-1} \gg \cdots \gg k^2_{T,1} \gg Q^2_0. \tag{1.25}$$

Hence the largest contribution comes from the parton closest to the photon, whose transverse momentum is equal to $k_{T,n}$ (see figure 1.6).

At present, the parton density functions (PDFs) are incalculable in QCD, and therefore must be determined from data. The dynamic evolution of partons in x within the framework of BFKL evolution equations also becomes relevant.

1.5.2 The BFKL Evolution Mechanism

At very low x, where $\ln(Q^2/Q_0^2) \ll \ln(1/x)$, terms of $\alpha_s^n ln(1/x)^n$ can no longer be neglected. Where terms in $\alpha_s^n \ln(Q^2/Q_0^2)^n$ are unimportant, the QCD expansion is approximated by terms in $\alpha_s^n \ln(1/x)^n$ (LLA$(1/x)$). In this region of phase space, the Baltitsky-Fadin-Kuraev-Lipatov (BFKL) formalism assumes that the interaction between the quark and the photon is dominated by the $g \to gg$ splitting process. The gluon density function g is related to the unintegrated gluon distribution in the proton f

$$xg(x,Q^2) = \int_0^{Q^2} \frac{\mathrm{d}k_T^2}{k_T^2} f(x,k_T^2,Q^2). \tag{1.26}$$

From this formalism, the BFKL equation is deduced and can be written as follows:

$$x \cdot \frac{\mathrm{d}f(x,k_T^2,Q^2)}{\mathrm{d}x} \equiv K_L \otimes f(x,k_T^2,Q^2) = \lambda f, \tag{1.27}$$

where K_L is the Lipatov kernel which includes the summation over all powers of $\alpha_s \ln(1/x)$. In contrast to DGLAP, there is no strong ordering in transverse momenta though there is an ordering in x:

$$Q^2 \sim k^2_{T,n} \sim k^2_{T,n-1} \sim \cdots \sim k^2_{T,1} \sim Q^2_0. \tag{1.28}$$

One of the examples of a typical BFKL process can be seen in figure 1.6. At present, there is no firm evidence yet at HERA that any more than DGLAP is needed. Currently, the low x HERA results are still consistent with the BFKL model. In order to find some discrepancy between both models, the final hadronic state of exclusive vector mesons has to be investigated (see section 1.8).

1.6 Photoproduction

In the region where $Q^2 \simeq 0$, a quasi-real photon interacts with the proton. Since the ep cross-section is inversely proportional to Q^4 at large Q^2, it is dominated by *photoproduction* events. In the absence of high p_T jets or heavy flavour to provide a hard scale, perturbative QCD is no longer applicable in this region of phase space. However, another theory developed by *Regge* [14] is able to describe the "soft" photo-production scattering processes. For such processes, the γp centre of mass energy, $W_{\gamma p}$, can be approximated as:

$$W^2_{\gamma p} = y \cdot s. \tag{1.29}$$

1.7 The Gluon Density of the Proton

The H1 collaboration has extracted the gluon distribution from the scaling violations of the structure function F_2. As can be seen from figure 1.7, the gluon content inside the proton is dependent on x and Q^2. In order to complement this measurement and test the consistency between different HERA data, single channels can be used to measure the gluon distribution. As the valence quarks inside the proton are u and d quarks, it is impossible to extract the gluon distribution from processes which are constrained to such quarks only. In heavy quark production, hadronic final state particles with c or b content can be created. The leading order diagram for heavy quark production is the boson-gluon fusion process shown in figure 1.8. The cross-section is proportional to the gluon density.

One of the most important production processes that can be used to measure the gluon distribution is *open charm production*. The most precise results have been obtained from the production of $D^\star$ mesons. As the $D^\star$ only contains one single $c(\bar{c})$ quark (anti-quark), a potential second candidate may be produced in the event. The $D^\star$ can decay though several channels. The golden charm decay is the most important one:

$$D^{\star +} \rightarrow D^0 \pi^+ \rightarrow K^- \pi^+ \pi^+_{slow}$$

From figure 1.9, it can be seen that the gluon distribution has already been measured

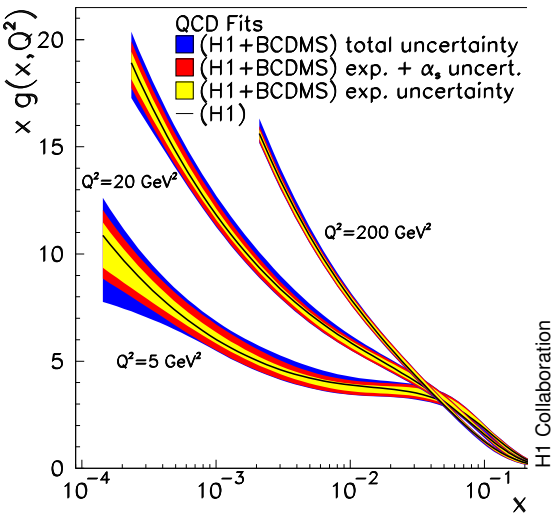

Figure 1.7: The extracted gluon distribution from the inclusive F_2 measurement is shown as a function of x for different values of Q^2.

using this channel. However, the errors on the measurement are statistically dominated, especially in the low x region. In order to minimise statistical errors, a high number of $D^\star$ events need to be triggered.

Apart from extracting the gluon distribution from the $D^\star$ cross-section, it can also be extracted from the J/ψ ($c\bar{c}$) cross-section. The J/ψ vector meson decays leptonically into a pair of electrons or muons (see section 1.9).

1.8 Diffractive Vector Meson Production at HERA

One way to investigate parton dynamics at low x values as well as the transition between the perturbative and non-perturbative regimes is to look at exclusive vector meson production. This process can be either elastic ($e\,p \to e\,V\,p$) or proton dissociative ($e\,p \to e\,V\,Y$). Vector mesons (VM) are mesons with $J^{PC} = 1^{--}$, where J is the spin of the vector meson. They change sign under a parity transformation or charge conjugation. A diffractively produced VM is shown in figure 1.10. In this process, the Mandelstam variable t can be defined as:

$$t = (p - p')^2, \tag{1.30}$$

where p is the four-momentum of the incoming proton and p' is the four momentum of the final state proton or its excitation, Y. In the Regge theory of strong interactions [17], where the proton interacts diffractively, the interaction occurs through the exchange of a colourless object, a Pomeron, which possesses the quantum numbers of vacuum ($J^{PC} = 0^{++}$). Where $s \gg |t|$, the elastic cross-section, can be written as:

$$\frac{\mathrm{d}\sigma_{el}}{\mathrm{d}t} \propto \left(\frac{s}{s_0}\right)^{2\alpha_{I\!P}(t)-2}, \tag{1.31}$$

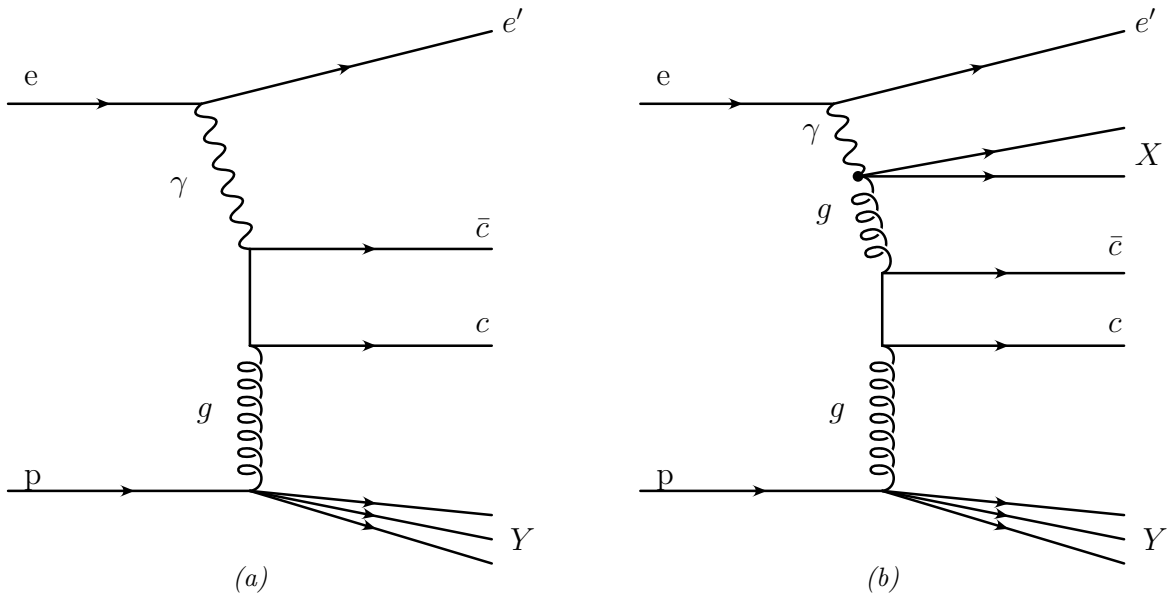

Figure 1.8: The leading order boson-gluon fusion process for heavy quark production is shown in the case of charm production. Whereas the direct process involves the photon interacting in a point-like way in (a), the gluon originating from the photon interacts with the proton in the resolved case shown in (b).

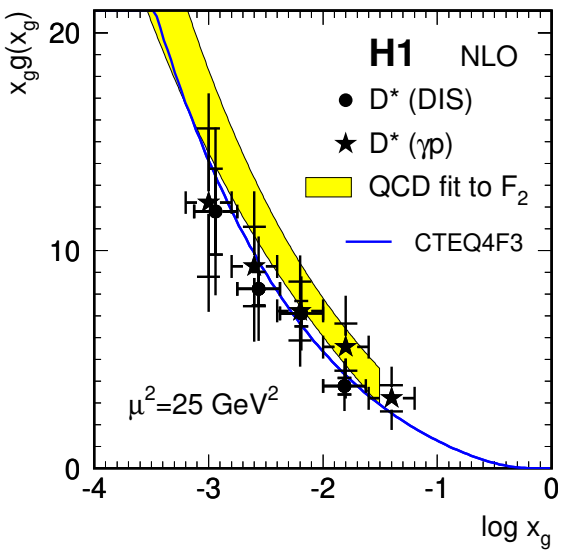

Figure 1.9: The gluon density of the proton determined from the measurement of the $D^\star$ cross-section in DIS and photo-production is shown. The data are compared to the result of the H1 QCD analysis of F_2 (shaded band) as well as the CTEQ4F3 [15] parametrisation (from [16]).

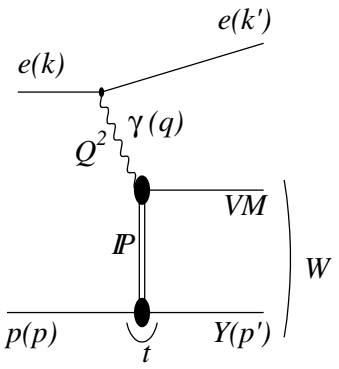

Figure 1.10: Diffractive vector meson production at HERA. The Mandelstam variable t is the energy transferred at the proton vertex. In the elastic regime, the proton remains intact whereas in the inelastic regime the proton breaks up into the final state Y.

where $\alpha_{I\!P}(t) = \alpha_{I\!P}(0) + \alpha'_{I\!P}\, t$ is the pomeron trajectory and s_0 is an energy scale. As the pomeron is exchanged in the region of phase space that in non calculable in pQCD ("soft"), is called a soft pomeron. In the region where diffraction occurs, the intercept $\alpha_{I\!P}(0)$ for this soft pomeron was extracted from fitting elastic hadron-hadron cross-sections [18] which rise slowly as s increases. This is due to low $|t|$ exchanges predominantly. The intercept was found to be $\alpha_{I\!P}(0) = 1.08$.

It can also be shown [19] that the elastic amplitude at $t = 0$ is related to the total photoproduction cross-section $\gamma\, p \to X$, such that:

$$\sigma_{tot} \propto s^{\alpha_{I\!P}(0)-1} \tag{1.32}$$

Using equation 1.29, equation 1.31 can be re-written as follows:

$$\frac{d\sigma_{el}}{\mathrm{d}t} \propto \left(\frac{W}{W_0}\right)^{\delta}, \tag{1.33}$$

with $\delta \equiv 4\,\alpha_{I\!P}(t) - 4$. Figure 1.11 shows that all vector meson photoproduction cross-sections are well described by the relation predicted by Regge theory. However, the exponent δ increases as the mass of the VM increases. Indeed, for all light vector mesons, $\rho(770)$, $\omega(783)$ and $\phi(1020)$, figure 1.11 and other data shows that the data are well described by a trajectory $\alpha_{I\!P}(t) = 1.08 + 0.25\,t$, similar to that for the total elastic cross-section. Thus, the total photo-production cross-section and the light vector meson cross-sections involve "soft" pomeron exchange. However, the J/ψ cross-section shows a much steeper $W_{\gamma p}$ dependence and the intercept $\alpha_{I\!P}(0)$ is required to be 1.20 [21]. Hence, the elastic vector meson cross-section requires a harder pomeron when the mass of the vector meson is large. The mass of the VM appears to provide a "hard scale".

The heavy vector meson cross-sections are well described in the framework of perturbative QCD [22]. In pQCD, the virtual photon fluctuates into a quark-anti-quark pair which interact diffractively with the proton by exchanging a pair of gluons.

However, not only the mass of the vector meson seems to play a role in determining whether a process is "hard" or "soft". The behaviour of vector mesons at different values

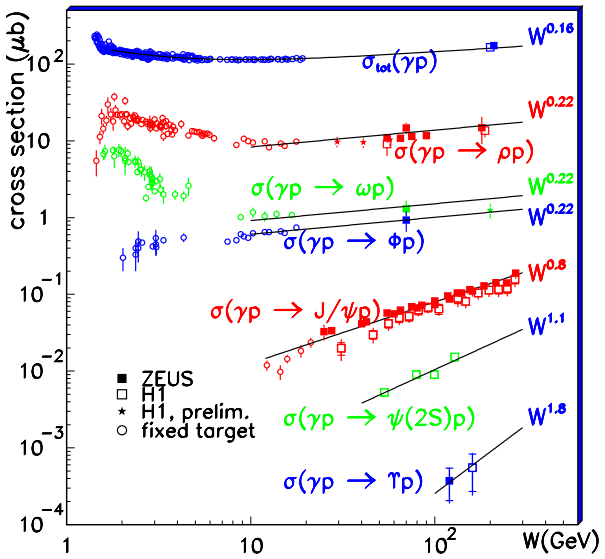

Figure 1.11: Overview of the photon-proton cross-section compared to the cross-section of the different vector meson particles measured at HERA. All cross-sections are shown with respect to the hadronic mass $W_{\gamma p}$ (from [20]).

of Q^2 was determined in the case of elastic ρ^0 mesons in electro-production. In figure 1.12, the cross-section of the elastic ρ^0 channel is shown as a function of $W_{\gamma p}$ for different values of Q^2. As Q^2 rises, the energy dependence of the cross-section becomes stronger.

In e^+p interactions, the differential $\gamma^* p \to \rho^0 Y$ cross-section $\frac{\mathrm{d}\sigma}{\mathrm{d}t}$ was measured for $|t| < 12$ GeV^2 [24]. It was found that this variable, Mandelstam $|t|$, may serve as a "hard" scale and thus $|t|$ can also be used to investigate the transition between perturbative and non-perturbative QCD. During the HERA I running period, a measurement of the $\gamma^\star p \to \rho^0\ Y$ cross-section at high $|t|$ was not possible at H1 because of the high prescale factors of the corresponding triggers. With the help of the Fast Track Trigger, the design of such a high $|t|$ ρ^0 trigger would allow the H1 collaboration perform this measurement at HERA II.

A continuing discussion at HERA concerns the regions of validity of the QCD evolution schemes such as BFKL and DGLAP. In the case of the J/ψ meson, where the mass already provides a "hard" scale at $|t| = 0$ GeV^2, a measurement of the cross-section of J/ψ mesons with a large momentum transfer squared $|t|$ in the proton-dissociative channel was performed by the H1 collaboration. This measurement is shown in figure 1.13 as a function of the γp centre of mass system W. At large $|t|$, it was found that the results of this measurement seem to have a better agreement with the predictions from the BFKL equation which indicates that BFKL effects start to become important in this region of phase space and that a "hard" BFKL-like pomeron is involved in the exchange.

Currently, the statistics of such processes are still poor. At HERA II, vector mesons produced via such a production mechanism can be triggered with the help of the FTT,

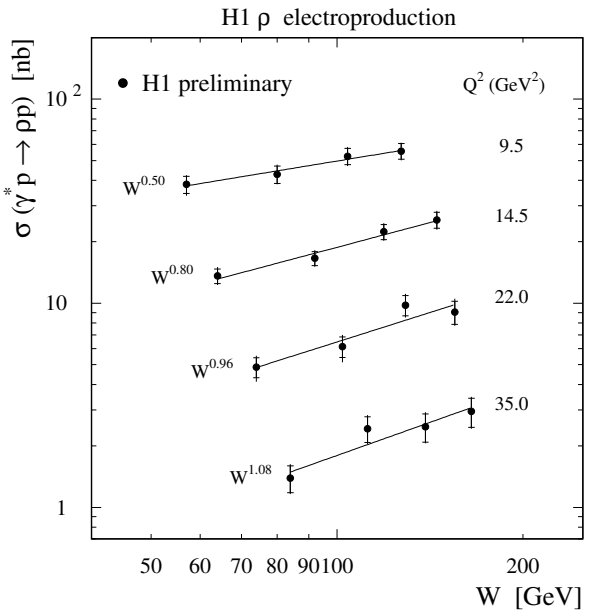

Figure 1.12: The elastic ρ cross-section ($\gamma^* p \to \rho^0 p$) is plotted as a function of $W_{\gamma p}$ for different values of Q^2 [23]. The corresponding fits are of form $\sigma(W) \propto W_{\gamma p}^{\delta}$.

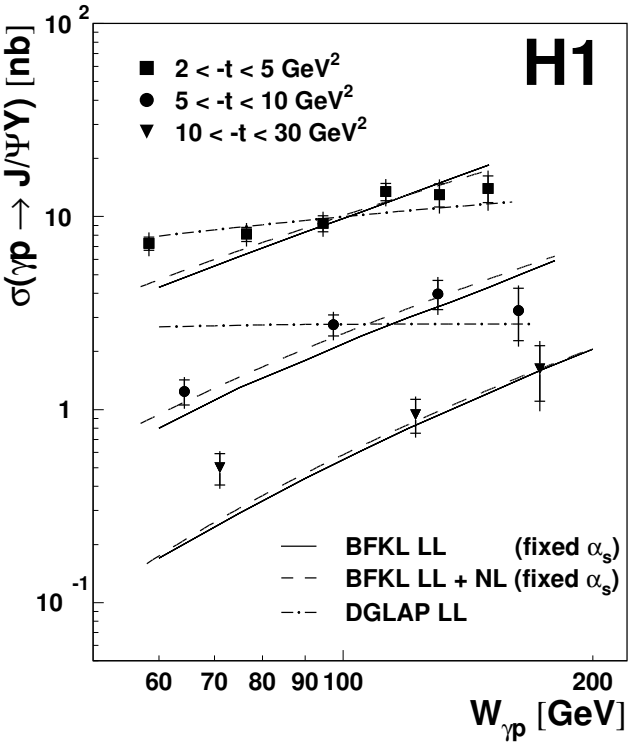

Figure 1.13: The measured diffractive J/ψ cross-section σ in the kinematic range $50 < W < 150$ GeV is shown as a function of the Mandelstam variable W. The inner error bars correspond to the statistical errors of the measurement. The outer ones are the sum of the statistical and the systematic errors (from [25]).

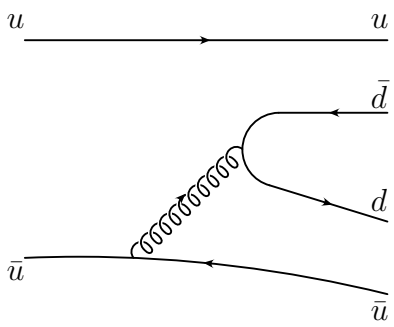

Figure 1.14: Strong decay of ρ^0 vector meson to $\pi^+\pi^-$ pair.

which was specifically designed to trigger on exclusive final state particles. With increased statistics a more precise statement of how well BFKL works is possible.

1.9 Decay Modes of ρ^0 and J/ψ Vector Mesons

From the Heisenberg uncertainty principle the lifetime τ of a particle is related to the resonant width Γ:

$$\tau = \frac{\hbar}{\Gamma}, \tag{1.34}$$

where $\hbar$ is the reduced Planck constant[†].

The ρ^0 meson has a broad width of 150.7 ± 1.2 MeV [6], characteristic of decays through the strong interaction, and thus has a short lifetime of $(4.3677 \pm 0.0348) \cdot 10^{-24}$ s. Due to the low mass of the ρ^0 meson (768.5 ± 0.6 MeV [6]), this specific vector meson decays hadronically into two pions as shown in figure 1.14. This happens over 99 % of the time.

The J/ψ has a mass of (3096.88 ± 0.04) MeV [6]. Despite the fact that it can decay hadronically, it has a very narrow width $\Gamma_{J/\psi} = (87 \pm 5)$ keV [6]. Hence it has a lifetime of $(7.6 \pm 0.1) \cdot 10^{-21}$ s. From the fact that there is no colourless gluon, the J/ψ decay via a single gluon exchange is not observed. Thus, the J/ψ vector meson can only annihilate into a minimum of three gluons as shown in figure 1.15(a) owing to its spin parity being 1^{--}. Hence, this decay is Zweig suppressed. The most common hadronic decay that is observed is the decay to five pions. The J/ψ decay to three pions via a three gluon exchange is shown in figure 1.15(a).

$$\begin{aligned} BR(J/\psi \to 2(\pi^+\pi^-)\ \pi^0) &= (3.37 \pm 0.26)\ \% \\ BR(J/\psi \to 3(\pi^+\pi^-)\ \pi^0) &= (2.9 \pm 0.6)\ \% \\ BR(J/\psi \to \pi^+\pi^-\pi^0) &= (1.50 \pm 0.20)\ \% \end{aligned} \tag{1.35}$$

The electromagnetic decay of the J/ψ takes place via a single photon exchange as shown in figure 1.15(b). As can be seen from equations 1.36, the branching ratios of both $J/\psi \to \mu^+\mu^-$ and $J/\psi \to e^+e^-$ are roughly the same due to lepton universality.

[†] $\hbar \equiv \frac{h}{2\cdot\pi}$, where h corresponds to Planck's constant.

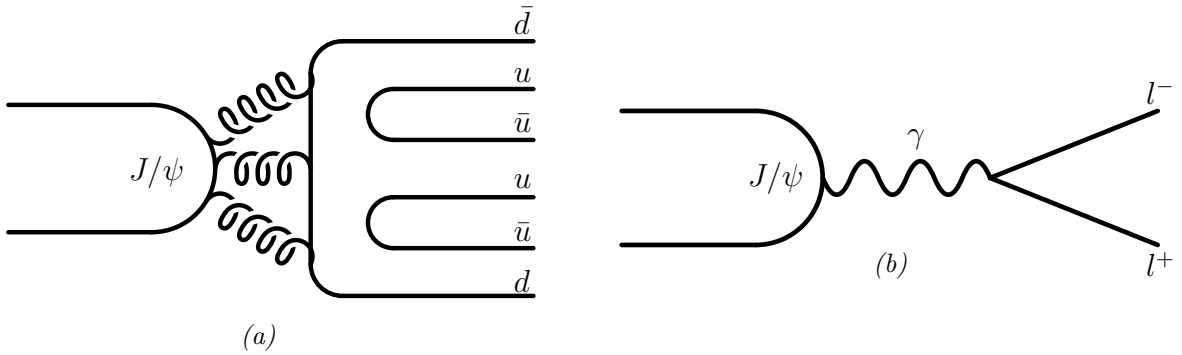

Figure 1.15: The two decay modes of the J/ψ vector meson are shown: (a) the strong decay into three pions as well as (b) the electromagnetic decay into two leptons.

$$\begin{aligned} BR(J/\psi \to e^+e^-) &= (5.93 \pm 0.10)\ \% \\ BR(J/\psi \to \mu^+\mu^-) &= (5.88 \pm 0.10)\ \% \end{aligned} \tag{1.36}$$

The lifetime of a J/ψ meson decaying to muons is $(1.25 \pm 0.11) \cdot 10^{-19}$ s, which is much longer than the unsuppressed ρ^0 decay.

1.10 Summary

With the recent luminosity upgrade, the very high Q^2 region can be explored in further detail. At this new "energy frontier", new discoveries are possible. Furthermore, the precision measurement of the structure functions allows the extraction of precise parton density functions.

Through the analysis of exclusive final states, HERA data will provide a detailed testing ground for QCD dynamics over a large range of the kinematical phase-space. Thus, complementary to the gluon extraction from the scaling violations in the measurement of the inclusive F_2 structure function, the triggering of $D^\star$ mesons in open charm production can be used to extract the gluon distribution inside the proton.

The measurement of vector meson cross-sections is another important physics area at HERA. Vector meson cross-section measurements show that the cross-section is not only dependent on the mass of the vector meson that is considered but also on the value of Q^2 and $|t|$ at which the measurement is performed. Hence, measuring the differential cross-sections of various vector mesons with respect to $|t|$ allows the investigation of the transition between the perturbative and non-perturbative regimes. Considering proton-dissociative vector meson processes, like $\gamma p \to J/\psi\, Y$, also allow the determination of the regions of validity of QCD evolution schemes. Thus, it was found that at high values of $|t|$, BFKL effects start to become important in the $\gamma p \to J/\psi\, Y$ process.

Evidently VM production is a rich source of information to test and explore QCD at the overlap between the perturbative and non-perturbative regimes. It is therefore of interest

to retain a high yield of VM events during HERA II. This was one of the reasons for developing the FTT.

Chapter 2

The H1 Experiment at HERA

2.1 Introduction

The "Hadron Elektron Ring Anlage" (*HERA*) at the "Deutsches Elektron Synchrotron" (*DESY*) laboratory in Hamburg, Germany is a unique *ep* collider. This chapter starts with an overview of the HERA collider. A brief description of the recent HERA luminosity upgrade follows. The H1 detector is introduced followed by a description of its main components. In the last section, the H1 trigger system is presented. The discussion of the H1 trigger strategy at HERA II that is included in this section sets the scene for the following chapters.

2.2 The HERA Storage Ring

The HERA collider consists of two accelerators in a circular ring tunnel with a circumference of 6336 metres. As can be seen from figure 2.1, electrons are accelerated in the clockwise direction up to energies of 27.6 GeV while the protons are accelerated in the anti-clockwise direction. Between 1992 and 1997, the proton beam energy was 820 GeV. In 1998 it was increased to 920 GeV, which resulted in an increase of the centre-of-mass energy from 300 GeV to 318 GeV.

The electron and proton beams are brought into collision in the two interaction regions of the ZEUS and H1 experiments. These are located at the South and North Halls respectively. A further two fixed target experiments called HERMES and HERA-B are located on the East and West sides of the accelerator respectively (also shown in figure 2.1). HERMES utilises the electron beam, which is polarised during the passage through HERMES, colliding with a polarised hydrogen, helium or deuterium gas target. In this way the HERMES experiment is able to investigate the proton and neutron spin structure functions. The aim of HERA-B was initially to investigate CP violation in the $\bar{B}^0 B^0$ system with the b quarks obtained by inserting a tungsten wire target into the proton beam halo.

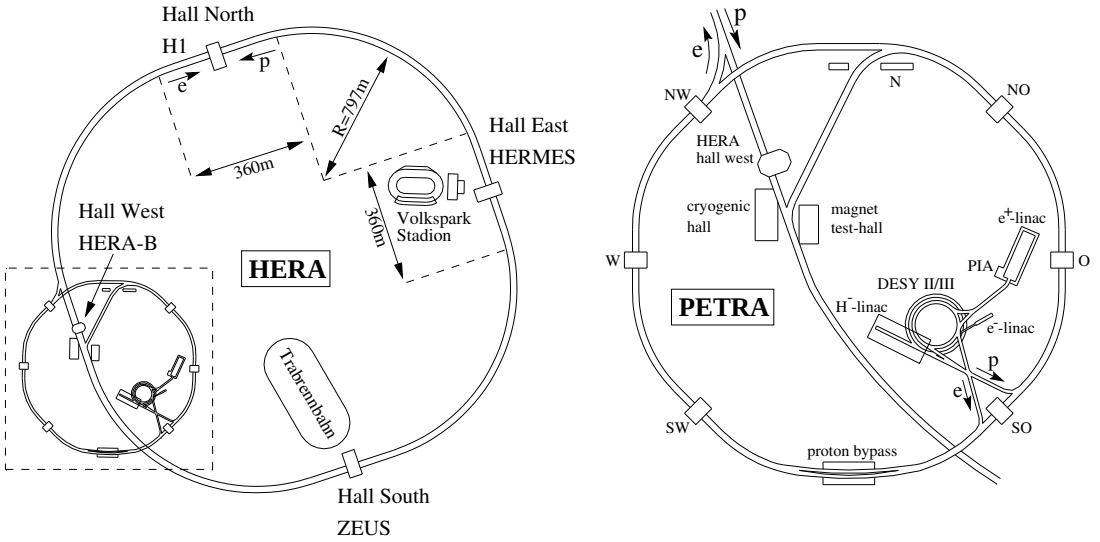

Figure 2.1: The HERA accelerator and its pre-accelerator, PETRA.

As the cross-section for $e - p$ interactions is small, very high fluxes are needed. Both, the electron and proton beams are made up of approximately 180 packets (*bunches*) which contain of the order of 10^{10} particles each. A small number of these bunches (*pilot bunches*) are non-colliding and are used to study background induced by interactions of the beam with the wall of the beam pipe (*beam-wall interactions*) or with residual gas from within the beam pipe (*beam-gas interactions*). Every 96 ns, two bunches collide within the detectors, defining a bunch-crossing frequency of 10.4 MHz.

2.3 The HERA II Luminosity Upgrade

The instantaneous luminosity L is related to the electron current I_e as shown from the following equation:

$$L \propto \frac{I_e N_p}{\sigma_x \sigma_y}, \tag{2.1}$$

where N_p is the number of proton particles per bunch, σ_x and σ_y are the lateral coordinate widths of the bunches in the interaction region.

From September 2000 until July 2002, HERA shut down for a extensive upgrade project to upgrade the luminosity. As can be seen from equation 2.1, several parameters can be changed to upgrade the luminosity. The most direct, which is to raise the beam currents, would mean that the accelerator would have had to be modified significantly [26]. Therefore, the improvement of the focusing of the beam currents in the interaction region was preferred. For this purpose superconducting focusing magnets have been designed and installed within the H1 detector [26]. Due to the change in focusing of the electron beam, synchrotron radiation is expected to increase and some of the H1 detector parts had to be modified appropriately. It was necessary to introduce an elliptical beam pipe and radiation masks within the H1 experiment. New collimators were included within the

detector in order to shield the detector parts from the proton beam because of focusing. A comparison between the HERA I and HERA II design parameters is shown in table 2.1.

	HERA I (2000)		**HERA II**	
	e-beam	p-beam	e-beam	p-beam
Energy	27.5 GeV	920 GeV	27.5 GeV	920 GeV
# bunches total/colliding	189/174	180/174	189/174	180/174
Particles per bunch	$3.5 \cdot 10^{10}$	$7.3 \cdot 10^{10}$	$4.0 \cdot 10^{10}$	$10.3 \cdot 10^{10}$
Beam current	50 mA	100 mA	58 mA	140 mA
Beam size $\sigma_x \times \sigma_y$	192 μm $\times$ 50 μm	189 μm $\times$ 50 μm	112 μm $\times$ 30 μm	112 μm $\times$ 30 μm
Luminosity	$1.69 \cdot 10^{31}\text{cm}^{-2}\text{s}^{-1}$		$7.57 \cdot 10^{31}\text{cm}^{-2}\text{s}^{-1}$	
Specific luminosity	$0.66 \cdot 10^{30}\text{cm}^{-2}\text{s}^{-1}\text{mA}^{-2}$		$1.82 \cdot 10^{30}\text{cm}^{-2}\text{s}^{-1}\text{mA}^{-2}$	
Luminosity increase	4.5			

Table 2.1: Comparison of the HERA I and HERA II design parameters (from [27]).

At the same time, the H1 collaboration took the opportunity to upgrade a number of their detector parts and trigger systems. In order to be able to trigger on exclusive final state processes, one of the upgrade projects was to replace the existing central drift chamber trigger ($DCr - \phi$), which is based on signals from the central tracking chambers, by the Fast Track Trigger(FTT). A detailed description of this project will be given in chapter 3. Other H1 upgrade projects are discussed in the following description of the H1 detector.

2.4 The H1 Detector

The H1 Experiment uses a multi-purpose detector which is designed to look at all aspects of *ep* scattering. A side view of the H1 detector is shown in figure 2.2. This also shows the three dimensional coordinate system used at H1, whose origin is chosen to be at the nominal interaction point [1]. Based on the right-handed coordinate system, the z-axis is defined to point in the outgoing proton beam direction and the x-axis points towards the centre of the HERA ring. The polar angle θ is defined with respect to the proton beam direction. As shown on the figure, the azimuthal angle ϕ is defined with respect to the x-axis. The end of the detector in the outgoing proton (electron) direction is referred to as the *forward* (*backward*) region. The fact that beams of different energies are collided at HERA leads to an asymmetric detector design with a more densely instrumented forward region where the proton fragments enter. Around the interaction point lie the tracking detectors consisting of the central and forward track detectors. The Liquid Argon Calorimeter (LAr) surrounds the tracking detectors in the central and forward regions. It is designed to give excellent reconstruction for particles at very high transverse momentum ($P_T > 25$ GeV) [28]. The electromagnetic [15] and hadronic [16] sections of the SpaCal complete the calorimetric coverage in the backward region. The superconducting solenoid [18] is able to bend charged tracks with its strong magnetic field of 1.15 T and therefore allows the determination of the momentum from tracks of charged particles in the trackers. The iron yoke [19] of the magnet is instrumented with streamer tubes which are used to measure the hadronic energy leaking out of the LAr. Muons are also detected by the streamer tubes. The forward muon detector [20] identifies muons in the forward region.

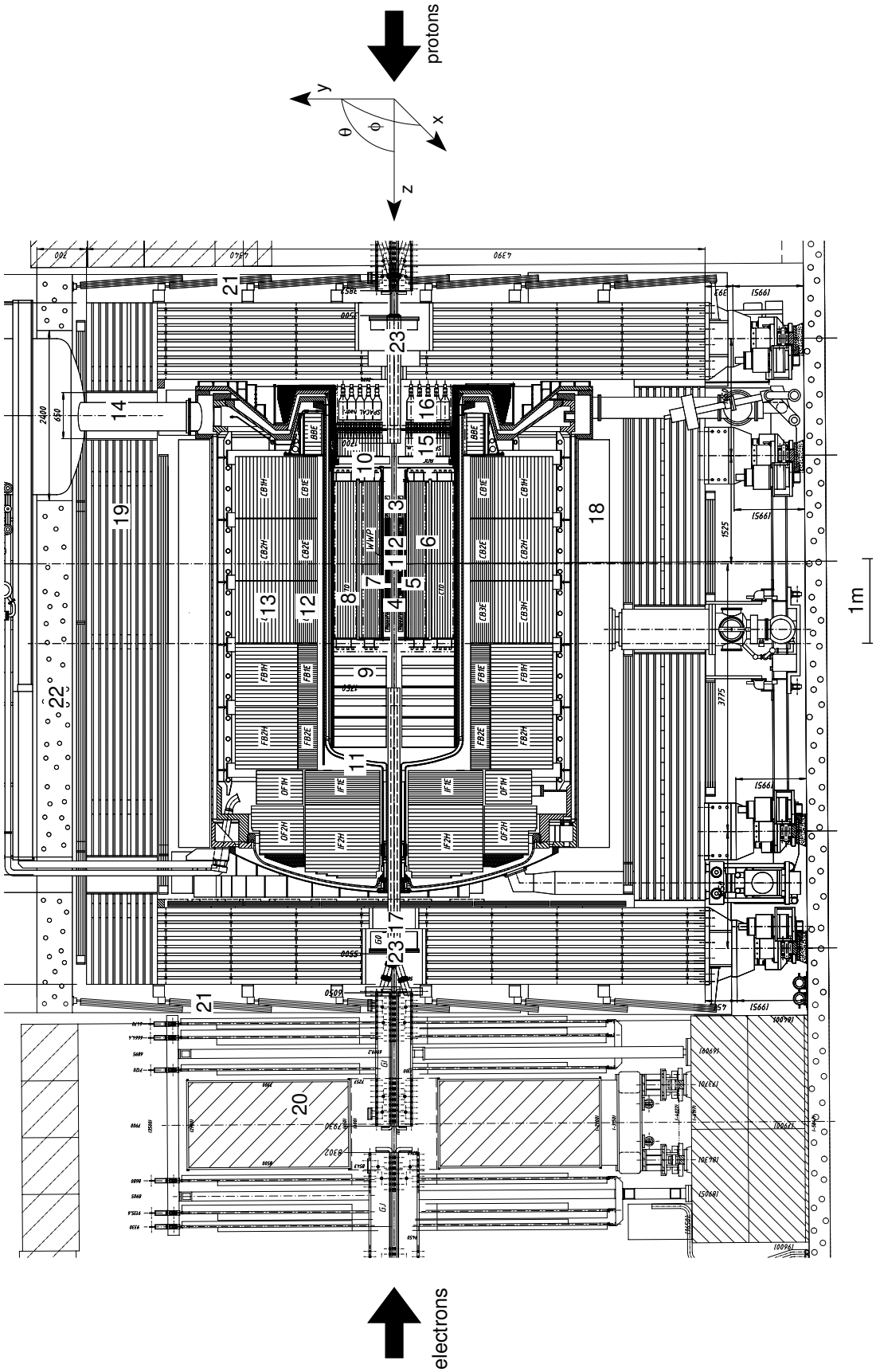

Figure 2.2: A cut through the H1 detector as it appears after the luminosity upgrade; see table 2.2 for the different sub-detectors. The coordinate system used in H1 is shown on top.

	Detector component	Abbreviation
1	Nominal interaction point	IP
	Tracking detectors	
2	Central silicon tracker	CST
3	Backward silicon tracker	BST
4	Forward silicon tracker	FST
5	Central inner proportional chamber	CIP
6	Central outer proportional chamber	COP
7	Inner central jet chamber	CJC1
8	Outer central jet chamber	CJC2
9	Forward tracking detectors	FTD
10	Backward proportional chamber	BPC
	Calorimeters	
11	Liquid argon container	
12	Liquid argon electromagnetic calorimeter	LAr elm.
13	Liquid argon hadronic calorimeter	LAr hadr.
14	Liquid argon cryogenics system	
15	Electromagnetic spaghetti calorimeter	SpaCal elm.
16	Hadronic spaghetti calorimeter	SpaCal hadr.
17	Plug calorimeter	Plug
18	Superconducting solenoid	
	Muon detectors	
19	Instrumented iron (central muon / tail catcher)	CMD/TC
20	Forward muon detector (incl. toroid magnet)	FMD
21	Veto wall / time of flight system	ToF
22	Concrete shielding	
23	New superconducting focusing magnets	GO/GG

Table 2.2: The main components of the H1 detector - legend to figure 2.2.

2.5 Tracking at H1

The tracking detectors are located closest to the nominal interaction point. They have been designed to give very a accurate measurement of the transverse momentum of charged particles with a transverse momentum p_T below 25 GeV. A further task is to separate closely spaced charged particles inside jets of hadrons. At H1, the tracking system consists of three different types of detectors.

Silicon strip detectors often consist of n-type bulk silicon, where the front side is implanted with closely spaced p-type silicon strips. When a charged particle passes through the silicon substrate, the ionisation frees electrons from the atoms inside the n-type bulk silicon leaving them with an electron vacancy. Electron/hole pairs are created. The voltage applied across the substrate drifts those pairs towards the surface where they are detected. The minimum energy to create an electron/hole pair is just 3.6 eV. The net effect of primary and secondary ionisation is around 80 electron/hole pairs per μm for a

minimum ionising particle.

Drift chambers contain anode and cathode wires that create a nearly uniform electric field inside the chamber. After a charged particle has passed through the chamber, the ionised electrons in the gas drift towards the anode wire plane at nearly constant speed. The drift velocity is measured, so that the time taken by the ionised electrons to reach the sense wire can be used to calculate the original position where the ionisation took place. The digitisation of the drift chamber signals is done using Flash Analogue to Digital converters (FADCs) at 104 MHz. This corresponds to a timing resolution * of 2.78 nanoseconds. With a drift velocity of 50 μm/ns and a bunch crossing frequency of 10.4 MHz, the longest path that can be travelled within one bunch crossing is 0.48 cm.

Proportional chambers consist of many closely spaced anode wires lying between cathode plates. When a particle passes through, the contained gas is ionised. The ionised electrons then drift toward the closest anode wire. Due to the strong electric field close to the anode, the ionised electrons cause secondary ionisation. The signal received on the anode is proportional to the initial ionisation. These signals are fast enough for easy use in triggering, and give position accuracies of the order of the wire spacing ($\sim$ mm).

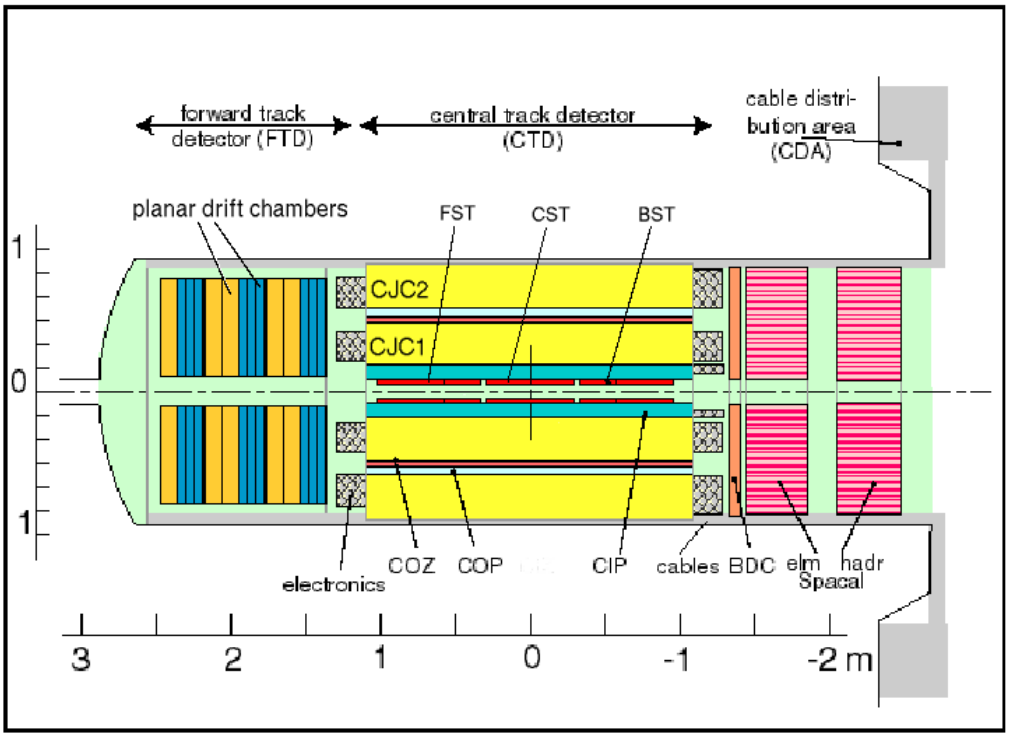

Figure 2.3: Side view of the H1 tracking system

As can be seen in figure 2.3, the central tracking detector is composed of several subsystems. Moving radially out, they are displayed as follows:

- The silicon trackers (BST, CST, FST)

*The timing resolution σ is calculated from the equation $\sigma = \frac{a}{\sqrt{12}}$, where a is the time between two consecutive samplings.

- The central inner proportional chamber (CIP)
- The central jet chamber 1(CJC1)
- The central outer z-chamber (COZ)
- The central outer proportional chamber (COP)
- The central jet chamber 2 (CJC2)

2.5.1 The Central Tracking Detector

The Silicon Trackers

The central silicon tracker [2] was added into the H1 design in order to aid the identification of primary and secondary vertices [29]. The CST covers the range $20° < \theta < 150°$ and is centred around the nominal interaction point. The BST [3] is intended to improve the reconstruction of backward going electrons. It is composed of eight planes of silicon detector strips, each with a 16-fold segmentation in ϕ. Its angular range of $162° < \theta < 176°$ corresponds to a Q^2 range between 2 and 100 GeV^2, allowing precision measurements of low x and low Q^2 DIS events.

The forward silicon tracker (FST) [4] was added in the year 2000 upgrade in order to improve the tracking in the forward direction. With a range $8° \leq \theta \leq 16°$, high momentum heavy quark physics can be extended to the large x region and electrons scattered at very high Q^2 can be better reconstructed.

The Central Jet Chambers

The Central Jet Chambers [30] CJC1 [7] and CJC2 [8] are drift chambers with sense wires strung in parallel to the beam direction, such that tracks are best measured in the r and ϕ coordinate plane. The inner jet chamber, CJC1, includes 30 cells with 24 sense wires and measures tracks with polar angle $22.5° < \theta < 157.5°$. The outer central jet chamber CJC2 covers a polar angle range of $39° < \theta < 141°$. It contains 60 cells each of which include 32 sense wires. The drift cells are inclined by 30° to the radial direction. Due to the magnetic field of 1.15 T, the ionised electrons interact with the magnetic field according to equation 2.2 and drift with a given drift or Lorentz angle to the electric field.

$$\vec{F} = q \cdot (\vec{E} + \vec{v} \wedge \vec{B}), \tag{2.2}$$

where $\vec{F}$ is the force exerted on the ionised particle, q and $\vec{v}$ are the ionised particle's charge and velocity respectively and $\vec{B}$ is the magnetic field. The CJC is filled with a mixture of $Ar/CO_2/CH_4$ (89:10:1) gas and at present, the Lorentz angle is 42°. Hence, the drift direction for high momentum tracks is never far from perpendicular to the track direction. Tracks with a transverse momentum higher than 400 MeV cross the sense wire plane at least once. As the distance to the wire plane is less than 50 ns, such a track can

be associated to a specific bunch crossing. Once the transverse momentum of the track is above $\sim$ 800 MeV, they will also cross cell boundaries. In addition to sense wires, the CJC includes drift, voltage and cathode wires. As only timing information can be collected at the readout state, a left-right ambiguity of track segments is apparent. The problem is resolved by staggering the sense wires around the sense wire plane by 150 μm. Two voltage wires are placed between neighbouring sense wires to prevent pick-up from adjacent sense wires. According to [30], the possibility that part of an electron avalanche hits the wrong sense wire is then reduced by a factor of two. The z-coordinate measurement from the CJC is done by charge division and has a resolution varying between around 3 cm for pions and 22 cm for minimally ionising particles (eg. muons).

2.5.2 The Central Proportional Chambers

The main purpose of the two multiwire proportional chambers CIP [5] and COP [6] is to provide fast trigger information on the vertex from which tracks originate. The basic principle of the z-vertex trigger is shown in figure 2.4. Lines are drawn to join COP and CIP hits and extended to the z-axis. The z-axis intersections over the central 2.2 m are entered into a histogram which comprises 15 bins. Although the z-vertex histogram is symmetric around the nominal interaction point, the flexible design, which is based on programmable chips, allows for a shift of the histogram along the z-axis. This provides an effective way to identify *ep* vertices in the nominal interaction region and to reject proton induced background.

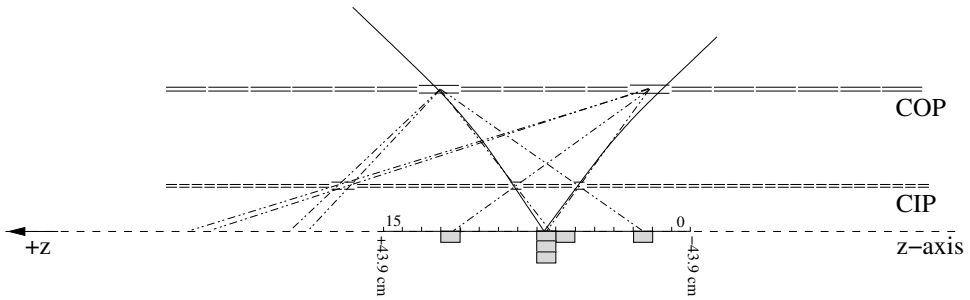

Figure 2.4: The CIP is used together with the COP to reconstruct tracks originating from the nominal vertex. At the same time, tracks due to beam-gas background for example can be identified on the basis of their vertex position and used to reject background events.

The Central Outer z-Chamber

The Central Outer z-Chamber is a drift chamber with sense wires perpendicular to the beam direction, which improves the measurement of the z-coordinate to a resolution of 260 μm.

2.5.3 The Forward Tracking Detector

Further track detection is needed to cope with the high track multiplicity in the forward direction. The FTD [9] is used to cover the angular range $5^\circ < \theta < 25^\circ$ and consists of three supermodules. The two supermodules which are closest to the nominal vertex incorporate three small modules and two larger modules. The most forward supermodule includes only one large module and three small modules. The smaller modules include four layers of planar chambers each, whereas the larger modules are composed of eight layers of planar chambers. The single hit resolutions of the planar drift chambers are 170 μm [31].

2.5.4 The Backward Proportional Chamber

The Backward Proportional Chamber [32] consists of three layers of hexagonal proportional chambers overlaid in order to measure the hit co-ordinate of a particle track with high accuracy. The BPC is installed in between the Spagetti Calorimeter and the central trackers.

2.6 Calorimetry

2.6.1 The Liquid Argon Calorimeter

Apart from the CJC, the Liquid Argon (LAr) Calorimeter [33] is the other principal component of the H1 detector. Its angular acceptance is $3.4^\circ < \theta < 153^\circ$. It is a sampling calorimeter that uses liquid argon as the active medium. Due to the fact that the gas has to be cooled in order to keep it in liquid form†, all the constituents of the LAr Calorimeter are incorporated within a cryostat. The advantages of argon are that it is radiation resistant, and impurities which would absorb the ionising particles are frozen out. The LAr Calorimeter is subdivided into eight wheels in z, each of which comprises eight octants in ϕ. The different wheels are named according to their nominal position with respect to the interaction point as seen in figure 2.5. The abbreviations are explained below:

- BBE: Backward Barrel Electromagnetic Calorimeter;
- CB1, CB2, CB3 : Central Barrel Calorimeter;
- FB1, FB2: Forward Barrel Calorimeter;
- OF1, OF2: Outer Forward Calorimeter;
- IF1, IF2: Inner Forward Calorimeter.

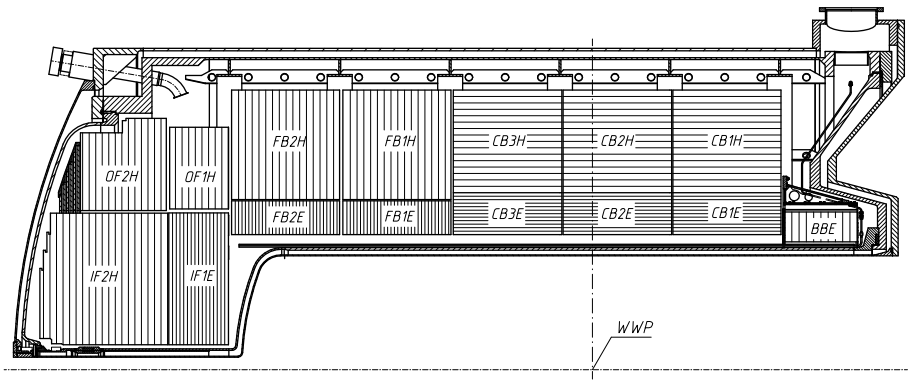

Figure 2.5: Side view of the LAr calorimeter in the $y-z$ plane. Only the upper part of the LAr calorimeter is shown as the detector is symmetric about the z-axis. The different modules are labelled.

In order to distinguish electromagnetic showers from hadronic showers, the calorimeter is subdivided into an electromagnetic [12] and a hadronic [13] section with the exception of the BBE region. The electromagnetic section of the calorimeter has lead plates and higher granularity to cope with electromagnetic showers. The hadronic section has a lower granularity and has iron plates.

The segmentation of the calorimeter into 44351 cells ensures a good spatial and energy resolution. Each cell consists of absorber plates supplemented by high voltage and readout electrodes as well as a liquid argon layer. The primary particle originating from the interaction point interacts with the absorber material to generate particle avalanches. The showers of secondary particles ionise the argon and thus make the energy measurement possible. The showers of secondary particles result from distinct electromagnetic and hadronic interaction mechanisms. In the electromagnetic part, the showers are formed due to bremsstrahlung as well as electron pair production, whereas in the hadronic part the inelastic interaction between the the primary particle and the nuclei of the absorber material creates the hadronic showers.

In the electromagnetic part, the absorber material is lead. Its total depth is equivalent to between 20 and 30 radiation lengths (X_0). The absorber material of the hadronic section is stainless steel and its depth is equivalent to between 5 and 8 interaction lengths (Λ). Test beam measurements of the different LAr modules have revealed that the energy resolution in the electromagnetic part is $\sigma(E_e)/E_e = 11\%/\sqrt{E_e} \oplus 1\%$ and $\sigma(E_h)/E_h = 50\%/\sqrt{E_h} \oplus 2\%$ in the hadronic part.

The detector response to hadronic showers is approximately 30% lower than for electromagnetic showers. In order to take into account this *non-compensation* effect, special software algorithms were developed to correct for this.

[†]The boiling point of liquid argon is 87.5 K.

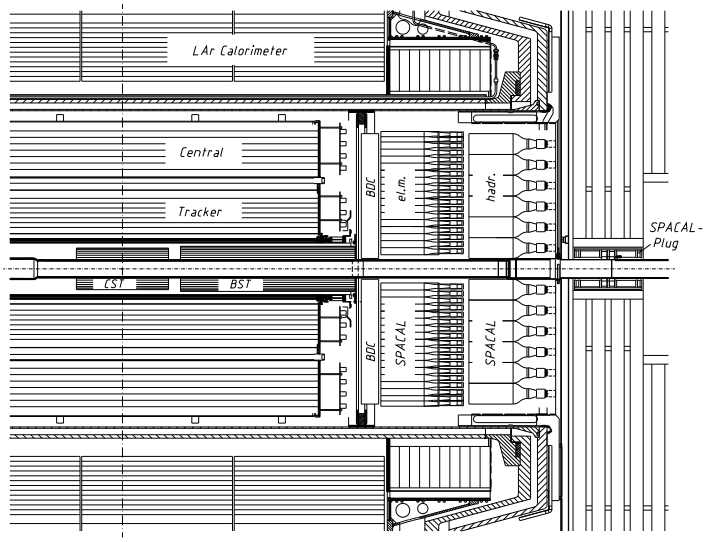

Figure 2.6: Side view of the Spacal detector in the $y - z$ plane.

2.6.2 The Spaghetti Calorimeter

The Spaghetti Calorimeter (SpaCal) [34] has been designed to identify electrons efficiently and to measure their energy and angle accurately. The range covered by the SpaCal has been altered from $153° < \theta < 177.5°$ down to $153° < \theta < 175°$ during the upgrade due to the insertion of the superconducting focusing magnet in the backward region. After the upgrade, the Q^2 range corresponds to $4 < Q^2 < 100$ GeV^2. Like the LAr calorimeter, the SpaCal consists of an electromagnetic [15] and an hadronic [16] calorimeter, but in this case both parts use lead as the absorbing material. Scintillating fibres are embedded in the absorber material (see figure 2.6). The incident particles shower in the lead and cause the fibres to scintillate and the light produced is collected by photomultiplier tubes.

The energy resolution of the electromagnetic part is $7\ \%/\sqrt{E/GeV} \oplus 1\ \%$. Due to the high granularity, a spacial resolution of 3 mm can be reached. The depth of the electromagnetic part is 28 radiation lengths. With a timing resolution of 1 nanosecond, the SpaCal is used in the trigger as a veto against out-of-time beam-induced background and it plays an important role in triggering electron candidates.

2.6.3 The PLUG Calorimeter

The PLUG Calorimeter [17] is located in the forward region of the detector. It is situated close to the beam pipe. The PLUG Calorimeter measures the missing transverse momentum of hadrons by closing the gap in between the beam pipe and the LAr calorimeter [35].

2.7 Muon Detection

2.7.1 The Central Muon Detector

The instrumented ion yoke [19] of the main solenoid is used for the detection of muons. It consists of a forward and backward barrel as well as forward and backward endcaps. From cosmic muon studies it has been shown that the efficiency for triggering muons with a transverse momentum above 2 GeV is approximately 90% [36]. Due to the high hadronic activity in the forward direction, it is often difficult to distinguish muons found in the central muon system alone from the hadronic background. In order to distinguish tracks from ep interactions from proton beam halo or cosmic muons, the forward muon detector is also utilised.

2.7.2 The Forward Muon Detector

The Forward Muon Detector (FMD) [20] [37] has been built to help the triggering and reconstruction of muons in the forward region. It is situated beyond the return yoke and covers a range $3^\circ < \theta < 17^\circ$. It consists of six double layers of drift chambers, three of which are situated on either side of a toroidal magnet. The drift chamber layers that are used are either theta or phi measuring layers. Both types are present on either side of the magnet so that the momenta p of the muons can be determined in the range $5 < p < 100$ GeV by measuring the θ and ϕ angles of each track before and after the interaction with the toroid's magnetic field. The spatial resolution of the detector is approximately 250 μm.

The Forward Muon Trigger (FMT) [38] uses the theta layers of the FMD to perform an independent fast reconstruction for triggering purposes under the assumption that the tracks originate from the interaction vertex.

2.8 Time of Flight Detectors

Time of Flight (ToF) detectors [21] are used to reject beam induced background events. Due to the large backgrounds, they play an essential role at H1. The ToF systems rely on the fact that the time of arrival for particles from the nominal interaction point at a specific space point in the H1 detector differs from the time of arrival for particles originating from background interactions elsewhere in the detector. Scintillator material is used by the ToF systems to give accurate timing (< 1 ns). The ToF detectors are placed close to the beam pipe and are located next to the PLUG calorimeter (PToF) and behind the backward endcap of the muon detector (BToF). Another ToF detector designed to not only reject proton beam–wall and beam–gas background but also to reject photoproduction background is situated inside the SpaCal (SToF). The additional FTi system has been installed during the upgrade program. One component, FTi1 is placed in

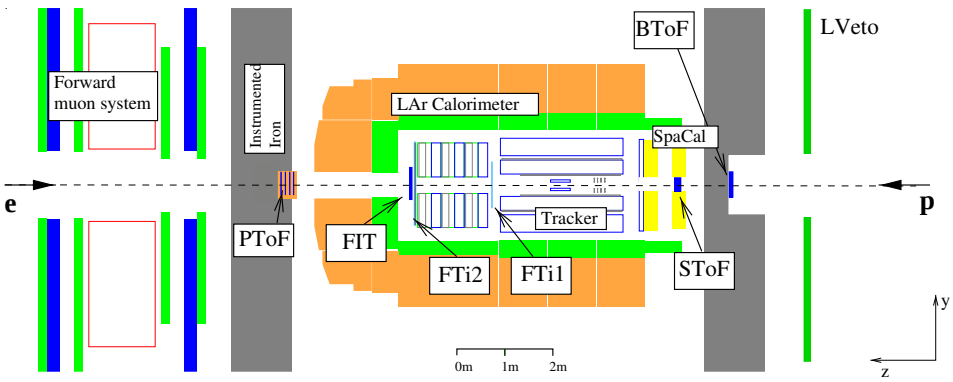

Figure 2.7: ToF system after the upgrade 2000.

between the central and forward tracking devices at $z = 1.4$ m. The second component, FTi2 is situated in front of the forward tracker at $z = 2.65$ m. The FIT which was already installed in 1998 is placed in front of FTi2. The large veto wall (LVeto) is placed at $z = -6.50$ m. It is used to detect particles from the proton beam halo as well as background from the proton beam generated upstream. Further details about the ToF system can be found in [39]. It is illustrated in figure 2.7.

2.9 The H1 Luminosity system

For a precise measurement of physics cross-sections, it is essential to determine the luminosity accurately. This is done using the H1 luminosity system, which is situated in the backward direction in the accelerator tunnel.

The H1 Luminosity system consists of an electron tagger and a photon detector (PD) [40]. The luminosity is extracted from the rate of the Bethe-Heitler Bremsstrahlung process ($ep \rightarrow ep\gamma$), which has a well known cross-section [41]. The tagger and the PD are Cherenkov calorimeters which contain an array of rectangular crystals. The H1 luminosity system is shown in figure 2.9. This system also tags "photoproduction" events at very low Q^2 ($Q^2 \lesssim 10^{-4}$ GeV^2) using two further electron taggers.

2.10 The H1 Trigger System

At HERA II design luminosity, the background rate can be up to a factor of a 1000 higher than the true ep interaction rate of approximately 1 kHz. Since events can only be written to tape at a rate of 10 Hz, a huge reduction rate that filters out background events as well as uninteresting physics events is needed. The fact that all drift chambers in the

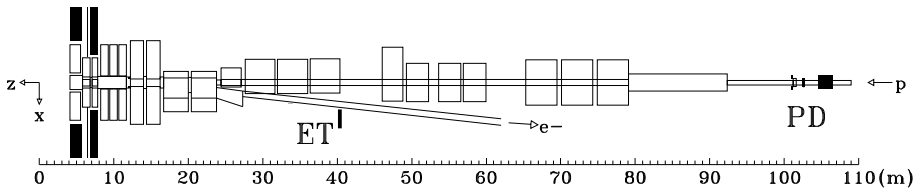

Figure 2.8: The H1 luminosity system after the upgrade 2000 as seen from the top. The e-tagger (ET) as well as the PD are clearly displayed. The H1 co-ordinate system is shown as well.

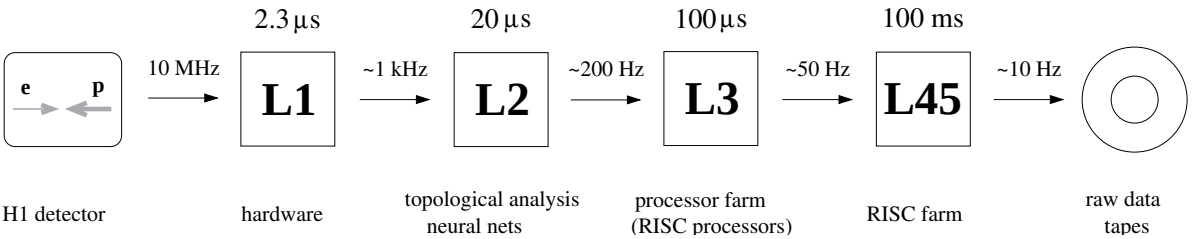

Figure 2.9: The H1 trigger concept.

H1 experiment have much longer response and readout times than the bunch crossing frequency is a further difficulty. Both these constraints make it a real challenge to read out all the relevant information without creating a large dead time fraction for the H1 experiment.

To solve these tasks successfully, a trigger concept, which resulted in the design of a multiple level trigger, was developed and is shown in figure 2.9.

At H1, almost every sub-detector is linked to at least one trigger system. The different levels of the trigger system are described in the following subsections. In order to reduce dead time significantly, the concept of pipelining was introduced. With this procedure the event information is stored in memory for 24 bunch crossings for each sub-detector which is in the trigger system, while the trigger remain sensitive to new information.

2.10.1 Level 1

At each bunch crossing, all sub-detectors involved send either 8 or 16 bits of information, called *trigger elements* (TE), to the First Level Central Trigger Logic (CTL1). These trigger elements must arrive within 22 bunch crossings [‡] (2.1 μs) of the event of interest [§]. The CTL1 then has 2 bunch crossings to take a decision. The present 200 trigger elements are logically combined to 128 sub-triggers which are designed to trigger the interesting

[‡]The time of 22 bunch crossings is set by the LAr calorimeter, which has the longest response and readout time in H1.

[§]This means that the longest path travelled within a drift chamber within the CTL1 latency is approximately equal to 10 cm assuming that the drift velocity is 50 μm ns^{-1}.

physics processes or to be used for monitor purposes. If at least one sub-trigger is set, a *L1KEEP* signal is sent to all sub-detectors. The pipelines of each sub-detector are then halted and dead time starts. All pipelines are rewound by 24 bunch crossings and the event of interest is read out. Once the pipelines are stopped, the second stage of the trigger system begins.

2.10.2 Level 2

The $L2$ system consists of three independent systems:

- the Neural Network trigger ($L2NN$) [42]
- the Topological Trigger ($L2TT$) [43] [44]
- the second level of the Fast Track Trigger.

At the second level, which has a latency time of 20 μs, the L1 trigger decision is refined. In a first step, L2TT as well as L2NN receive L1 trigger elements and revalidate the L1 validated sub-triggers using additional information that was not sent to the CTL1. In a second step, fast algorithms produce a set of 16 second level trigger elements for both the L2NN and the L2TT triggers. The use of this additional L2 information allows the reduction of prescales for some high rate L1 sub-triggers (see subsection 2.10.5). In the case of a positive decision, a *L2KEEP* signal is issued and the readout process of the whole detector information is started. In the case that an event is rejected ($L2REJECT$), the pipelines are cleared and re-enabled and deadtime ends.

The FTT also has an independent second level trigger as described in chapter 3. A more detailed description of the second level FTT algorithms can be found in [45].

2.10.3 Level 3

During the HERA I running period, the L3 trigger system was not in operation. In the HERA II running, data from various sub-systems can be collected to perform a preliminary event reconstruction on a PowerPC processor farm. Each processor analyses the data for a specific event signature. The result is communicated to the central trigger logic, which is able to handle up to 32 third level trigger elements. These $L3$ trigger elements are thus used to validate $L1$ sub-triggers. If all $L3$ analyses give a negative result, an *L3REJECT* signal is issued and causes the readout as well as the event reconstruction to be stopped immediately and the pipelines to be restarted. With the pipelines re-enabled, deadtime finishes. The aim at HERA II is to restrict the deadtime to 7 %.

2.10.4 Event Filtering and Online Reconstruction

The decision to finally keep or reject an event is taken by the $L4/5$ trigger system, which runs asynchronously to the HERA clock. For this task, a conventional Linux farm is used. At first, the event filtering is performed by classifying the events into categories of potential interest. Events that cannot be classified are rejected. A small fraction of these rejected events are kept for control purposes. The data passing the $L45$ conditions are then passed to the data logging system which transfers the data (L45 output) for permanent tape storage to Production Output Tapes *(POTs)* containing both the raw and reconstructed event information. Another output stream writes the compressed event information onto Data Summary Tapes *(DST)*, which are stored on disks. On DST, 10 kByte are needed on average to store one event. The DST enables much faster and easier access to the event information.

During the HERA I era, the $L45$ system used to be subdivided into the two independent sub-systems [46] L4 and L5. The event classification was done at $L4$ with a simplified version of the event reconstruction program relative to that used at $L5$. At Hera II, the two systems will be merged.

2.10.5 Prescale Factors

The input rate of the $L45$ trigger system should ideally be distributed more or less evenly over the 128 L1 sub-triggers. $L1$ sub-triggers which are re-validated at $L2$ and at $L3$ only enter $L4/5$ after validation. It may happen though, that a few of the sub-triggers accept events with a much higher rate than others and thus stop other interesting events from being triggered. To prevent this from happening, prescale factors are allocated to such sub-triggers. A prescale of factor "x" means that only each xth event is accepted. As far as possible, prescale factors should be avoided because the trigger efficiency of a sub-trigger with a prescale of factor "x" is effectively lowered by the same factor.

Chapter 3

The Fast Track Trigger

3.1 Introduction

In this chapter, the Fast Track Trigger (FTT) is presented. The presentation begins with a short account of the motivation for the Fast Track Trigger. The following section explains the FTT design, followed by the description of the hardware design including a description of the FTT L2 and L3 trigger levels. After the introduction of the important algorithms run by the FTT at L1, the FTT-L2 track parameters, used as a basis to perform on-line particle identification at FTT-L3, are defined.

3.2 Motivation for the Fast Track Trigger

After the upgrade, the high background together with a physics rate above 1 kHz will make it difficult to access data in the low x region. The only processes that can be triggered by pre-upgrade H1 triggers at acceptable rates are high Q^2 deep inelastic scattering events and processes with very high transverse momentum particles. As the maximum data taking rate at the third trigger level is 50 Hz, it is impossible to take all data and any simple sub-triggers to access low Q^2 data will have to be prescaled. Hence, the measurements of many exclusive processes would suffer from large prescales and would be recorded at rates that leave the statistical errors above the systematic. In order to improve statistics, a new trigger based on information from the Central Jet Chambers (CJC), was necessary. With the FTT, on-line particle identification is possible at early stages of the trigger algorithm for the first time at H1. By analysing the hadronic final state on-line, prescaling can be avoided.

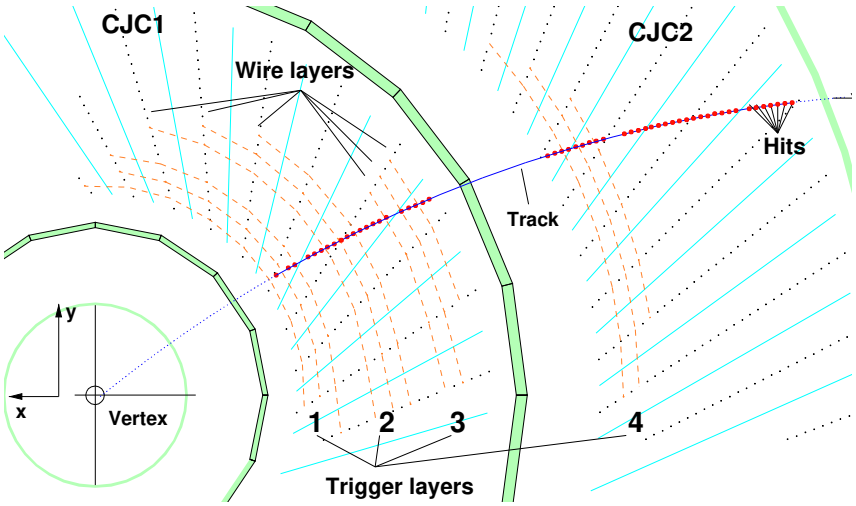

Figure 3.1: CJC $r-\phi$ projection, showing the 4 trigger layers. Within CJC1 each cell consists of three trigger groups and each cell in CJC2 only holds one trigger group.

3.3 Basic Principle of the Fast Track Trigger

The Fast Track Trigger (FTT) is integrated into the first three levels of the H1 trigger. The FTT uses the analogue signals from selected wires of the central drift chambers (CJC). Four different *trigger layers* are defined to reconstruct tracks. Each trigger layer consists of three *wire layers*. As shown in figure 3.1, three of these trigger layers are situated in CJC1 and one of them is situated in CJC2. Each trigger layer is sub-divided into *trigger groups*. A diagram of such a trigger group is shown in figure 3.2. Per cell and layer, a single trigger group is defined via the position of its middle wire. It consists of the three trigger wires forming a single trigger layer within the cell, which form the 'in cell' combination. Additionally, the outer wire of the left adjacent cell as well as the inner wire of the right adjacent cell are added such that a trigger group consists of five wires in total. In all cases, up to three valid hit combinations are possible. They are formed from one hit on the outer wire (either the basic outer wire or the outer wire from the left adjacent cell), one hit on the middle wire of the group and one hit on an inner wire (either the basic inner wire or the inner wire from the right adjacent cell) of the trigger group.

In the event that a large number of wires are broken, it is possible to reconfigure the FTT to use different wire layers as part of the trigger layer. The radii of the default trigger layers as well as the wires are listed in table 3.1.

Trigger layer	Chamber	wire layers	average radius (cm)	number of cells
1	CJC1	3,5,7	25.1	30
2	CJC1	10,12,14	31.3	30
3	CJC1	18,20,22	38.7	30
4	CJC2	4,5,8	58.7	60

Table 3.1: CJC wires associated to different trigger layers.

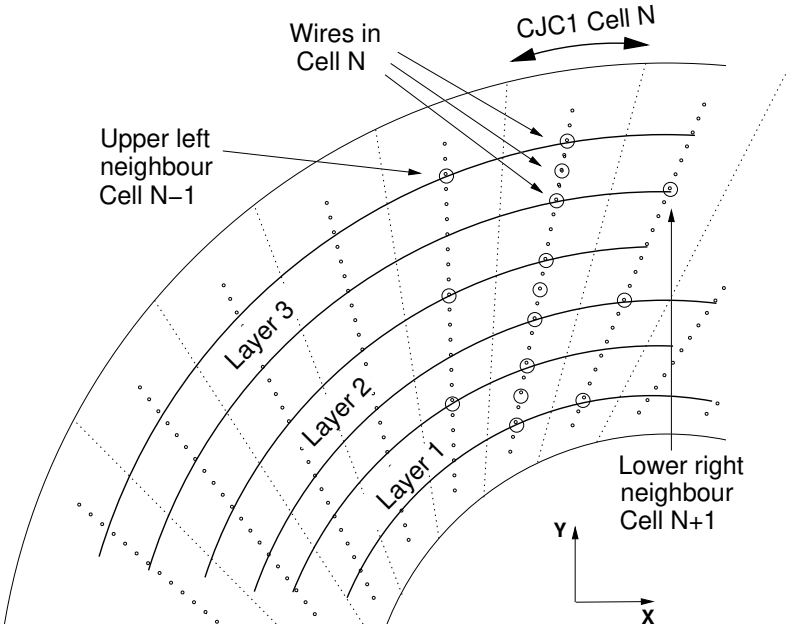

Figure 3.2: Projection in $r - \phi$, showing the 3 trigger layers in CJC1. One trigger group consists of three 'in cell' wires as well as the upper and lower wire of the left and right neighbouring cells respectively.

The different tasks of the FTT which are performed at the different trigger levels are summarised in figure 3.3. The first level algorithm has to make a trigger decision within the latency period of 2.3 μs. In the CJC, the maximum drift time is 1.1 μs. This means that less than 1.2 μs remain to perform the actual L1 algorithm. During this time, a comparison between the drift times of the hits that are found at L1 and the drift times of pre-programmed track segments from potential valid tracks, is performed. This comparison is done using a fast pattern recognition process. The coarse track segments that are identified in each layer are then combined into tracks by the L1 linker. The trigger decision is based on track multiplicities and the transverse momenta of tracks. The FTT-L1 trigger elements are sent to the central trigger, where the final decision is taken. Within a latency period of 20 μs after the L1Keep has been set, refined track segments are used by the FTT-L2 linker to perform a more precise track search. The refined track segments are then linked into tracks. After the linking process, the L2 linked tracks are fitted assuming that they originate from the vertex region. The fit drastically improves the resolution of the FTT. The L2 reconstructed tracks are used as a basis for the on-line particle identification of many exclusive final states. At L3, a full on-line event reconstruction for events with up to 48 tracks is possible allowing more sophisticated decisions to be made. The L3 algorithms take approximately 100 μs before a trigger decision is possible.

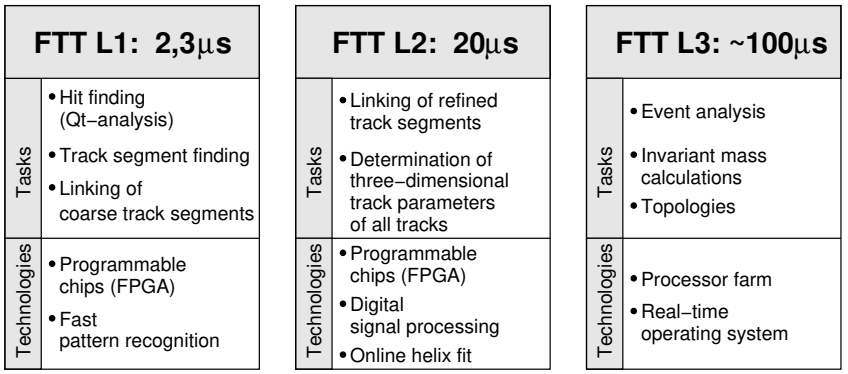

Figure 3.3: The FTT concept is based on a three level trigger system.

3.4 The FTT Hardware

The FTT hardware layout can be separated into three different parts as shown in figure 3.4. Each part corresponds to one of the three trigger levels. The communication between the different parts of the FTT is achieved via LVDS* signal lines. This standard assures the quick and safe transfer of data. The main components of the first level of the FTT are the 30 *Front End Modules* (FEMs). Each FEM processes data from 5 adjacent trigger groups. The different components on the FEM are 5 "front FPGAs†", 1 "back FPGA" as well as a VME interface (see figure 3.5). After the digitisation of the incoming analogue signals using 10 bit FADC of type AD9218-80 [47], the Q-t Analysis determining the timing of the hit and its position along the drift chamber wire, as well as the track segment finding take place on the front and back FPGAs. Both chips are Altera Apex20K400E devices [48]. The transfer of the valid track segments to the L1 and L2 Linker cards is done via intermediate merger cards. The z positions of the valid track segment hits, evaluated using the charge division technique, are also transfered to the z trigger card, an option proposed in [49].

If the L1Keep signal is set by the central trigger, the second level trigger of the FTT starts with the processing of data. Validated track segments with higher resolution are taken from the track segment finder to perform the linking on the L2 Linker card. Sorted by trigger group, the track segments are filled into 4 different histograms, each of which is associated to a specific trigger layer. Each of the histograms consists of 40 bins in κ ($\propto \frac{1}{p_T}$) and 640 bins in ϕ. During the linking step, pre-defined 5×5 regions are searched for coincidences of track segments. This is done by using a 3×3 sliding window. Each bin in the sliding window incorporates a specific weight. These weights are then used to find a peak in the 5×5 region. A linked track is defined when a coincidence with the same ϕ and κ values has been found in at least 2 trigger layers.

Once the first track segments have been successfully linked to tracks, they are sent on to the L2 Fitter chain consisting of 6 Fitter Boards. The 4 DSPs‡ on each Fitter board

*Low Voltage Differential Signal.

†Field Programmable Gate Arrays. see section 4.2.1

‡Digital signal processors.

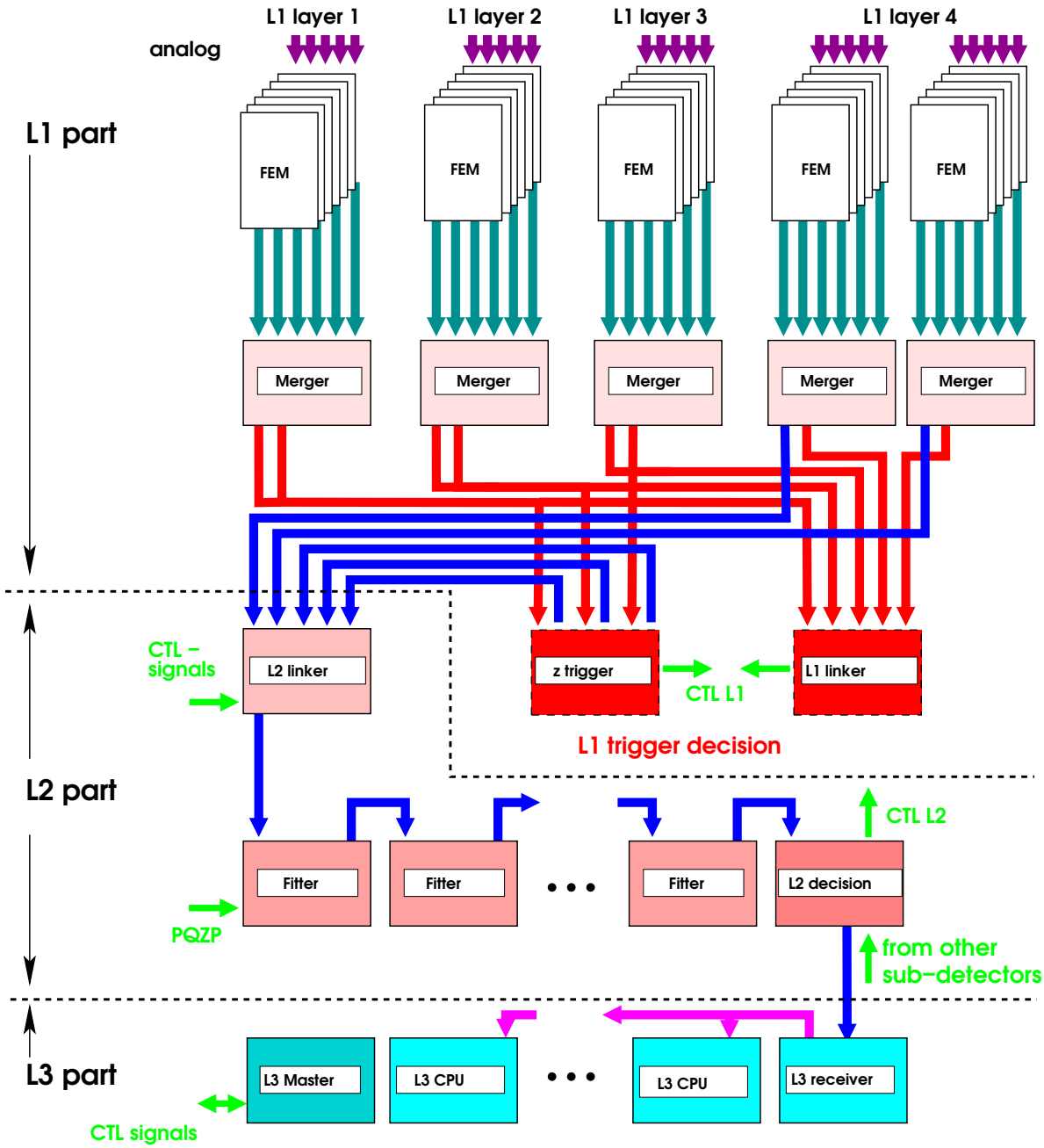

Figure 3.4: The hardware layout of the FTT.

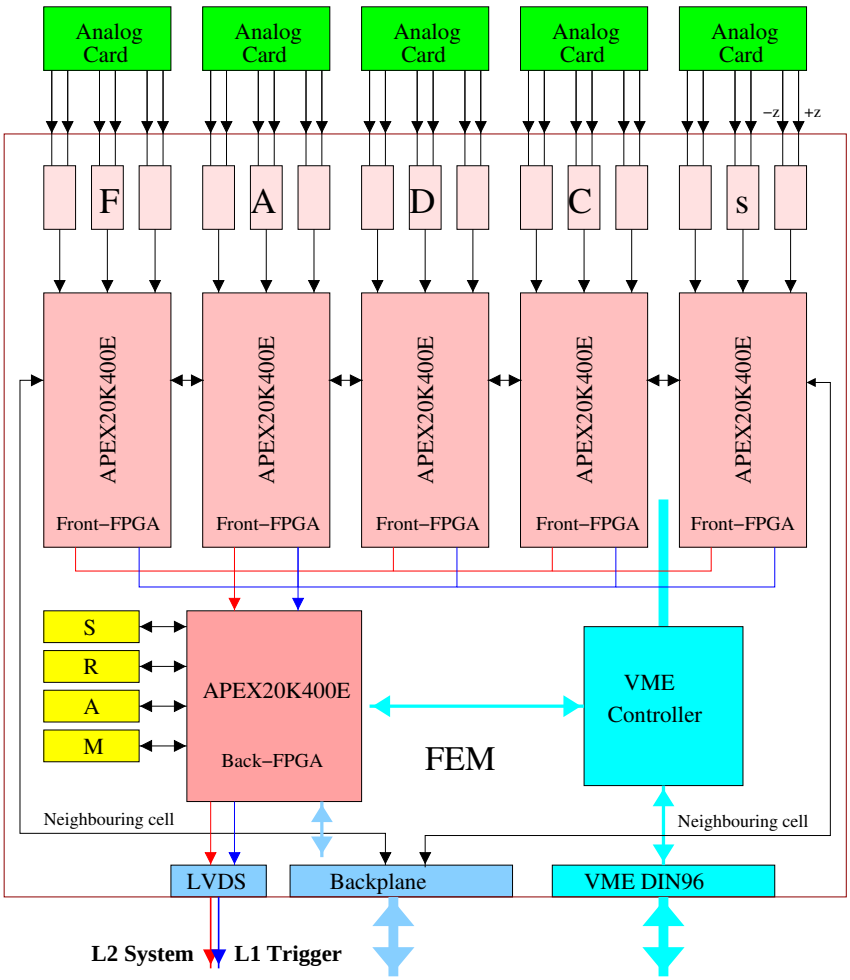

Figure 3.5: Schematic drawing of the Front End Module.

are used to perform the track fitting. In a first step, the curvature κ and the angle ϕ are used to fit a track in the $r-\phi$ plane [50]. In a second step, the polar angle θ is determined using a fit in the $r-z$ plane. A PQZP[§]-receiver is used to collect the data from different trigger sub-systems. Thus, the z-coordinate of the vertex as evaluated from the CIP/COP z-vertex trigger can be used to improve the FTT θ resolution. The current idea is to get the z coordinate of the vertex from the FTT z-vertex trigger [49]. For this trigger, a vertex resolution of $\sigma_z = 2$ cm is expected, which is slightly better than the vertex resolution of 2.5 cm from the z-vertex trigger which uses the CIP/COP proportional chambers. Thus the FTT-L2 θ resolution is 100 mrad (RMS). At the end of the fitter chain is the L2-decision card. This card collects the information of all successfully fitted tracks and generates the FTT-L2 trigger elements. Its decision is based on track related quantities [45].

If the central trigger sends an L2Keep signal, the track information as well as the PQZP data is transferred to the FTT-L3 system.

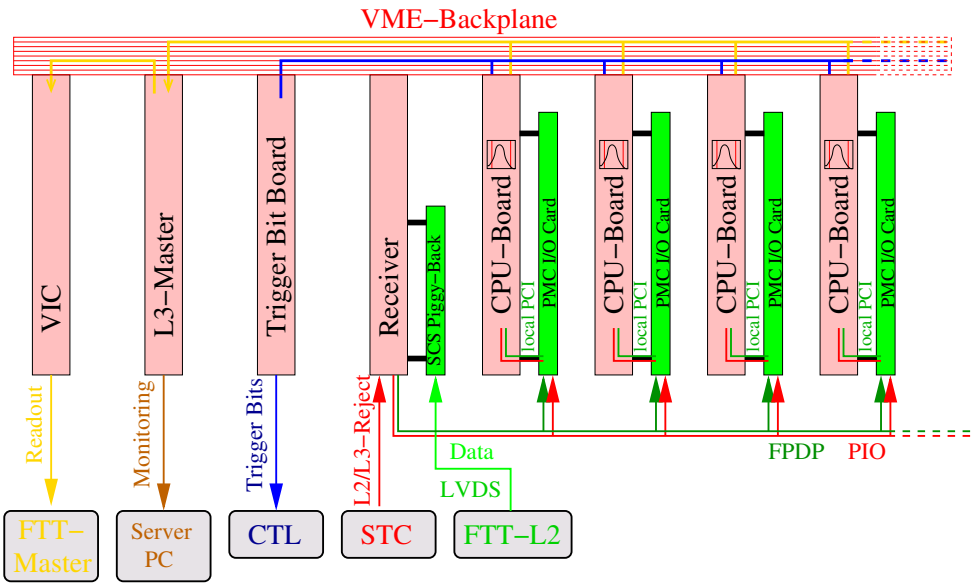

Figure 3.6: The L3 boards include 16 Motorola CPU cards on which several fast analysis algorithms can be run. Each of the 16 CPU cards is associated to a trigger element.

An overview of the third level of the FTT is shown in figure 3.6. It consists of a CPU farm. On each of the CPU boards, a specific trigger algorithm is run. Each CPU board is linked to an L3 trigger element. The FTT-L2 information is distributed to each CPU board in parallel. This information is used to perform on-line particle identification of decayed resonances as well as a search for selected topologies. The system is able to hold up to 16 processing CPU boards. The L3 Master collects all trigger elements and sends them on to the central trigger. A full description of the FTT-L3 can be found in [51].

[§]Parallel Quickbus Zero-Suppression Processor: A standard protocol used by H1 to send and receive trigger information

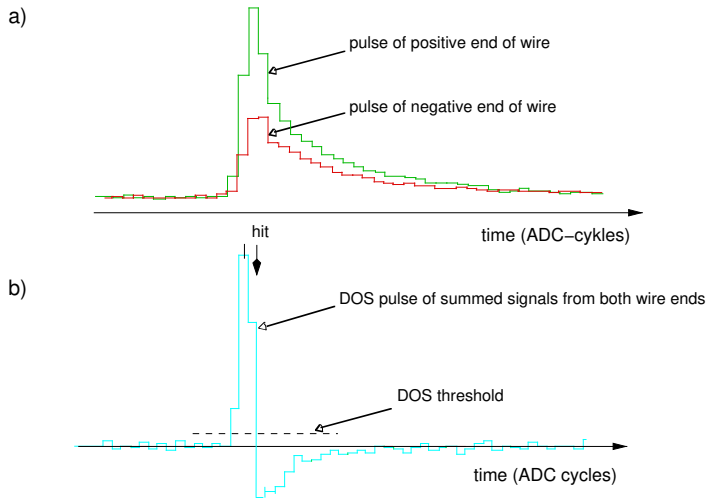

Figure 3.7: Figure (a) shows the digitised pulses from each end of a drift wire. Figure (b) shows the DOS signal after the summing of both digitised signals.

3.5 Principal Algorithms at L1

The algorithms that are run on the FTT hardware at L1 are the following:

- The charge and time (Q-t) Analysis;
- The Track Segment Finding Algorithm;
- The L1 Linker algorithm.

In this section, the Q-t Analysis as well as the L1 Linking algorithm are described in more detail. The Track Segment Finding algorithm is described in chapter 4.

3.5.1 Q-t Analysis

The Timing Analysis

The Q-t algorithm that is used by the FTT detects hits via a difference of samples (DOS) technique as described in [52]. The algorithm is based on the fact that a steep rise in the digital signal from both wire ends usually defines a hit. Figure 3.7 (a) shows the digital signals as they are recorded at both wire ends. After these digital signals have been summed up, the DOS technique involves the subtraction $bin_{n+1} - bin_n$ in order to find a rise (see figure 3.7 (b)). Once the difference is above the DOS threshold and the DOS signal has peaked, a hit is defined. In order to resolve separate hits, they have to be separated by 50 ns.

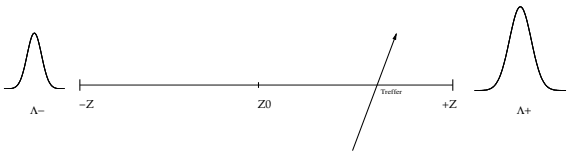

Figure 3.8: The determination of the z-coordinate through charge division. With the z-co-ordinate closer to the positive end of the wire, the amplitude of the charge arriving at the positive side of the wire is larger tan the one arriving at the side of the wire.

The Extraction of the z-Coordinate of the Hit

The z coordinate of the hit is determined by charge division. After a hit was found by the Q-t algorithm, the signal from each wire end is summed up over a fixed period of time. The running "summer" starts the integration with the bin before the bin defining the hit [52]. As shown in figure 3.8, the charge amplitudes recorded at each end of the wire depend on the position at which the charge that is due to the ionisation of the charged particle, is deposited on the wire. The z position of the charged particle can then be calculated from the following equation:

$$z = \frac{L}{2} \cdot \frac{Q^+ - Q^-}{Q^+ + Q^-}, \tag{3.1}$$

where L is the length of the wire and $Q^{+/-}$ is the charge amplitude measured at the $+z$ and $-z$ end of the wire respectively. Taking account of electronic gains and calibration effects, equation 3.1 can be re-written:

$$z = z_0 + \frac{L_{eff}}{2} \cdot \frac{\Lambda^+/g^+ - \Lambda^-/g^-}{\Lambda^+/g^+ + \Lambda^-/g^-}, \tag{3.2}$$

where $\Lambda^\pm$ and $g^\pm$ are the measured charge and the gain at the two ends of the wire respectively. The z-coordinate of each wire is extracted separately instead of obtaining only one z-coordinate per track segment. This allows a more flexible $r - z$ fit at L2 [53]. The z coordinates are stored in 6 bits per wire corresponding to a digitisation in bins of 3.4 cm. With the present gain, the bin size is smaller than the numerical precision of highly ionising particles in the CJC.

3.5.2 The Track Segment Linking at L1

During the time before an L1Keep signal is issued by the central trigger, data from each trigger group is transmitted to the L1 linker as shown on figure 3.9. There are 16 bits of information that are transmitted per cell and layer, resulting in 2400 bits transferred for each bunch crossing. Each bit that is set represents a track segment with a given curvature κ and azimuthal angle $\phi^\star$. Studies have shown that due to the inclination of the CJC cells with respect to the radial direction, the angle ϕ measured at the *distance of closest approach* (*dca*: see figure 3.10)) is unsuitable for the linking purpose, while the

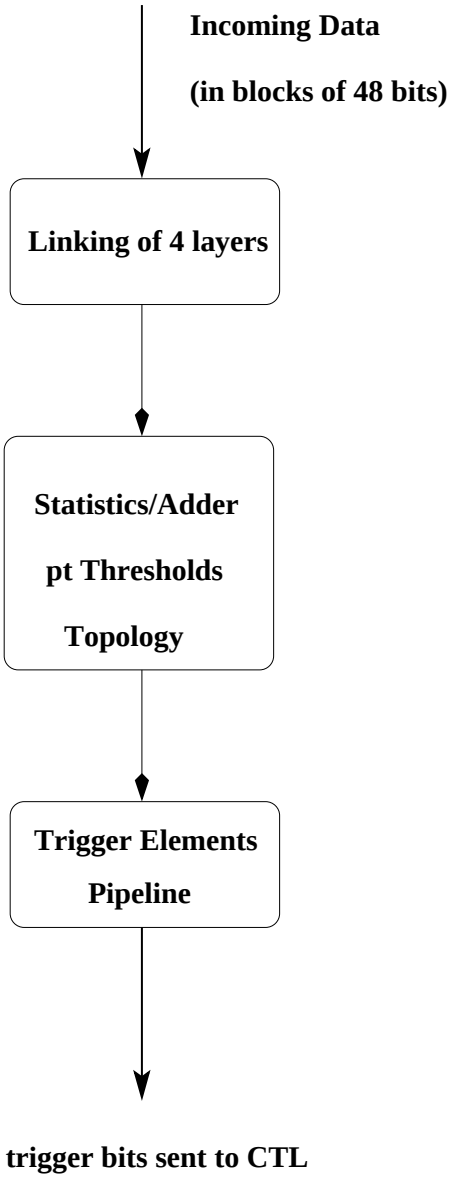

Figure 3.9: Flow diagram of the L1 linking algorithm.

angle $\phi^\star$ which is calculated at a radius of $r = 20$ cm, is reliable. The relation between $\phi^\star$ and ϕ measured at the nominal vertex ($dca = 0$) is given by the following equation:

$$\phi^\star = \phi_{dca=0} + 2 \cdot \arcsin\left(\frac{r}{2 \cdot R}\right), \tag{3.3}$$

where R is the radius of the track curvature. The track linking is performed in the $\frac{1}{p_T} - \phi$ plane. For each layer, a 16 by 60 $\frac{1}{p_T} - \phi$ histogram is filled. In order to link track segments to tracks, the 4 histograms from the different layers are overlaid. Once 2 out of the 4 histograms show a coincidence in the same window, a linked track is found.

As shown in the flow diagram, the bits collected from the FEMs are transmitted to the L1 Linker in 48 bit blocks. Due to the limited bandwidth, each incoming trigger bit sets two adjacent $\phi^\star$ bins in one of the four histograms. As there are only 30 cells in CJC1 and 60 cells in CJC2, the trigger bits of two adjacent CJC2 cells are combined through a logical "OR" before they are filled into the histogram.

Each of the 4 histograms is subdivided into 10 *sliding regions* of 6×16 bins. As each histogram represents a trigger layer in the $r - \phi$ plane, an overlap of 2×16 bins is needed as an overlap region to take into account the bin entries of adjacent sliding regions. The linking is performed in one sliding region per pipeline step. Thus, the pipelined algorithm needs ten 100 MHz cycles to perform the track linking once the histograms are filled. The t_0 validated tracks are extracted by comparing the histograms for different BCs. Approximately 200 ns after the first 48 bit block is received, the 16 FTT trigger elements are sent to the central trigger.

The algorithm that is currently implemented to determine the event t_0 is not based on the idea that t_0 validated tracks only have a lifetime of one beam crossing but rather on the idea that the number of track segments corresponding to a real track is highest in the bunch crossing of origin (event t_0). Thus, the number of track links defines the *track quality* of the track. The t_0 validation algorithm works in three steps:

- In the current bunch crossing, the track with the most links must have a track quality which is higher than a given threshold.
- The sum of track qualities has to be above a given threshold.
- The sum of track qualities in the current bunch crossing has to be larger than the sum of track qualities in the next bunch crossing.

If all three criteria are passed, a t_0 validated event is found and the FTT-L1 t_0 trigger element is set.

A more detailed description of the L1 linker algorithm can be found in [54].

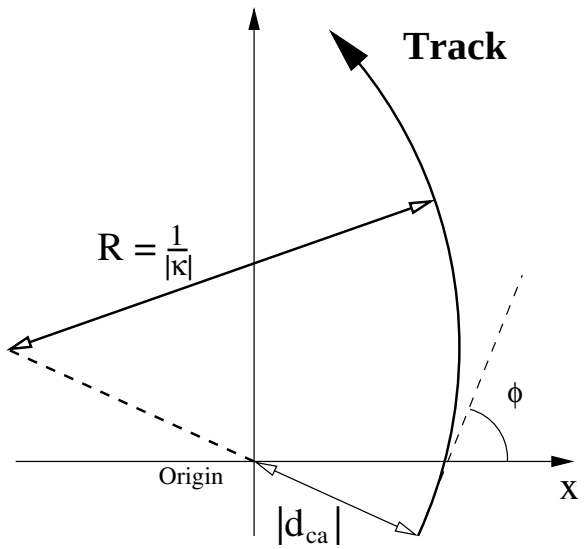

Figure 3.10: Definition of the FTT-L2 track parameters κ, ϕ and *dca*.

3.6 Definition of the FTT-L2 Tracks

The L2 reconstructed tracks that are used for the online particle identification are fully defined using track parameters which are summarised below:

- the curvature κ is defined to be the inverse radius of the track circle in the r-Φ plane. Assuming that the magnetic field B is uniform in the z direction, it is related to the signed transverse momentum of the track via the following relation:

$$p_T \text{ [GeV]} = -q \cdot 0.29979 \cdot B_z \text{ [T]} \cdot \left(\frac{1}{\kappa \text{ [m}^{-1}]} \right), \tag{3.4}$$

  where q is the charge of the particle in units of the electron charge, c is the speed of light and B_z is the z-component of the magnetic field B in the CJC (see figure 3.10).

- the track parameter *dca* is defined as the distance of closest approach of the track to the origin of the $H1$ co-ordinate system(see figure 3.10).

- the azimuthal angle ϕ is the angle measured between the tangent of the track at the *dca* point and the x-axis (see figure 3.10).

- the polar angle θ is the angle measured between the track and the z axis of the $H1$ co-ordinate system.

Chapter 4

The Track Segment Finding Algorithm

4.1 Introduction

In this chapter, a detailed description of the track segment finding algorithm is presented. The chapter starts with a short overview of the devices, techniques and algorithms that are used. The presentation of the different tasks of the track segment finder is followed by a discussion on the generation of track segment masks. Then, the resource usage of the algorithm is discussed. Finally, the state machine controlling the sequence of tasks that have to be performed, is described.

4.2 Devices and Technologies

4.2.1 Field Programmable Gate Arrays

Field Programmable Gate Arrays (*FPGA*s) are programmable chips that can make decisions based on multiple digital signal inputs. They can be used to the implement user defined algorithms. The Altera FPGAs used in the FTT design consist of two main components, as described below.

- The *Logic Array Block* (LAB) is made up of *Logic Elements* (LEs) which each have four inputs and one output. The sum and the carry of a single bit of a full adder can be implemented using only one LE.

- The *Embedded System Block* (ESB) is the building block which can be configured to behave as a RAM*, CAM† or FIFO‡ inside the FPGA. Each ESB has a private memory of 2 kB.

FPGAs are programmed using a hardware description language (HDL). After the compilation of the algorithm, the synthesis and fitting of the algorithm onto the chip is done using the chip vendor's proprietary software. The FPGA chips can be programmed a great number of times before they lose their functionality. A more detailed description of Altera FPGAs can be found in [48].

4.2.2 Content Addressable Memories

Content Addressable Memories (CAMs) function as "inverse" RAMs. The value that is transmitted to the CAM is searched for and if such a content is found, the address of the search value is returned. The return value can either be an unencoded address (see figure 4.1(a)) or a series of encoded addresses (see figure 4.1(b)). The Altera CAMs can be used in different modes [55]:

- The *single match mode* stops once a single match between the search value and the CAM content has been found. The return value can either be encoded or unencoded.
- The *fast multiple match mode* finds all matches between the search value and the CAM content. In this mode, the addresses are returned either encoded or unencoded. If multiple matches are found and the encoded address is returned, each address per single match is returned in series together with a validation flag. Hence one clock cycle is needed per match found.
- The *multiple match mode* differs from the fast multiple match mode in terms of the resources and clock cycles it needs to output the result. Whereas in the fast multiple match mode, the CAMs only include half as many entries per ESB and therefore can output the unencoded address within a single clock cycle, the simple multiple match mode needs 2 clock cycles to find all matches between the value searched for and the CAM content. Hence, the unencoded address is returned at every second clock cycle.

The use of the CAM technology enables a fast pattern recognition.

4.2.3 Shift Registers

In order to represent the drift times of the hits found by the Q-t algorithm, shift registers are used. At each clock cycle, the information on the shift registers is shifted by one

*Random Access Memory
†Content Addressable Memory: explained in subsection 4.2.2
‡First In First Out (a kind of memory buffer)

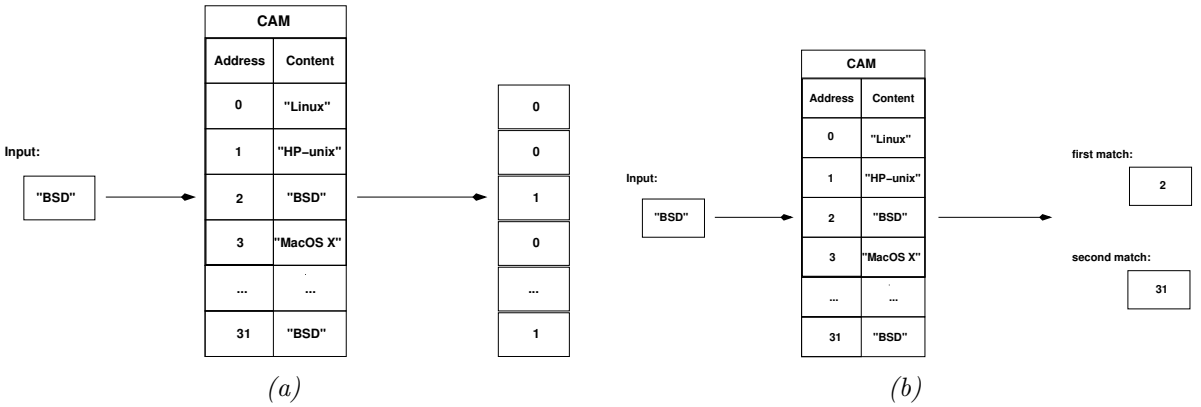

Figure 4.1: The above figure shows (a) the unencoded and (b) the encoded modes of the CAM search functions. In the unencoded mode, the CAM output is composed of a series of bits where each bit corresponds to a specific row. The bit is set if the input word was found in its corresponding row. In the encoded mode, the address of the matches that are found are sent out in series. The CAM search starts at position 0 and stops at position 31.

position. Hence, at a given clock cycle, the shift registers can be thought of as the representation in time of the hits in the chamber if an assumption on the bunch crossing of origin is made (t_0 hypothesis).

4.3 Description of Algorithm

The track segment finding algorithm is needed during two crucial stages of the FTT trigger sequence. At first, during the phase where the L1Keep signal is not set, the track segment finding algorithm has to search for patterns of hits on groups of three wires consistent with coarse track segments originating from the vertex region. The results are used as the input to the L1 linker as part of the FTT-L1 trigger algorithm. For this task, digitised hits are continuously read in from the Q-t Analysis and the track segment finding is performed once per bunch crossing. This phase is called the pre-L1Keep phase. During this phase the pipelines are active (PiEn = '1'). The post-L1Keep phase is entered once the pipelines are halted. During this phase, which repeats the track segment finding with higher precision at the start of the L2, the following tasks have to be performed by the track segment finder before the linking and fitting of the tracks is performed on the L2 boards:

- refinement of the coarse track segments found during the FTT L1 phase;
- validation of the refined track segments.

Figure 4.2 as well as figure 4.6 show an overview of the track segment finding algorithm. During the pre-L1Keep and post-L1Keep stages, coarse or refined track segments are sent to the L1 or L2 linker boards respectively.

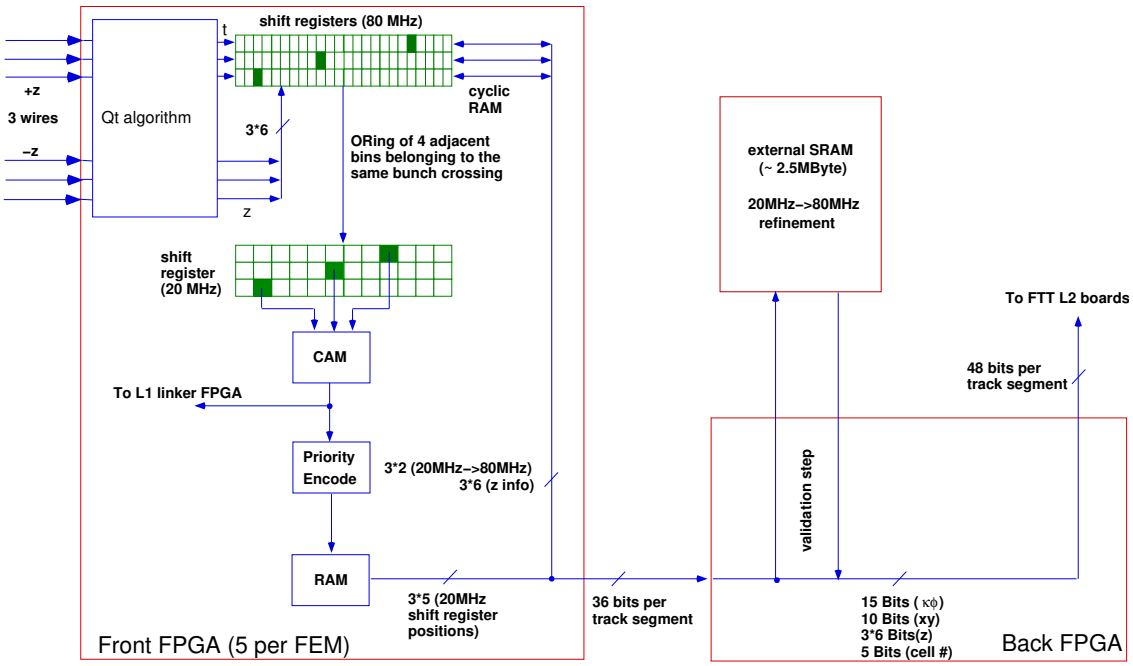

Figure 4.2: Overview of the track segment finding algorithm.

4.3.1 The Pre-L1Keep Phase

After the digitisation of the analogue signals by the FADCs as well as the Q-t Analysis the first task of the algorithm is to clock the hit information onto shift registers. As the hits found by the Q-t analysis are synchronised to the 80 MHz clock, but the shift registers are only clocked at 20 MHz, a logical "OR" between four consecutive 80 MHz bins is performed. There is no confusion because the Q-t algorithm is only able to provide one hit within 50 ns, so only one hit is possible per 20 MHz time slice. The shift registers are fully analysed once per bunch crossing, so that each of the possible t_0 hypotheses is investigated.

As the more precise timing information of the original hit with respect to the specific shift register bin is needed at a later stage of the algorithm, the 80 MHz timing information is stored in two bits of information in a parallel shift register. The z information is stored in a further six parallel shift registers, such that the information from one 20 MHz time slice is stored as 8 bits of information.

Space-Time Ambiguity

Translating the time information stored on a shift register into space co-ordinates reveals that the hit could originate from two different positions in the chamber on either side of the sense wire. This originates from the left-right ambiguity, a property common to drift chambers. Hence, the concept of *space-time ambiguity* emerges (see figure 4.3).

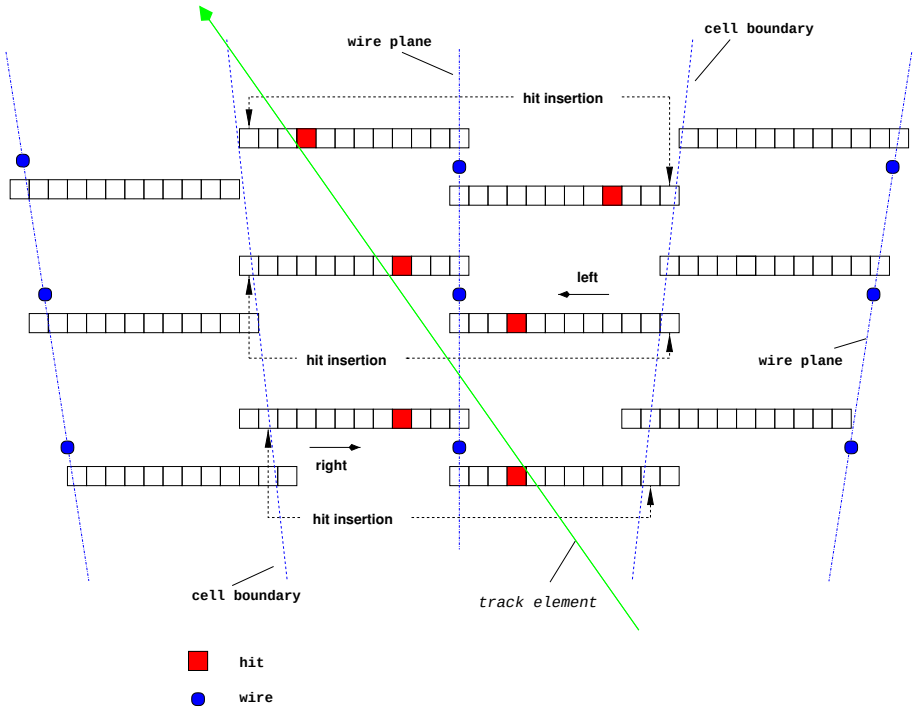

Figure 4.3: Hits emerging from two different space points which are equidistant from the trigger wire have exactly the same drift time.

As each hit combination is defined as groups of three hits, 8 different hit combinations are possible in the $r-\phi$ space coordinate plane.

Track Segment Pattern Extraction

For every bunch crossing, a search for valid track segments in the $r-\phi$ plane takes place using patterns supplied to CAMs. This search is realised by dividing the five shift registers of each trigger group into groups of patterns corresponding to acceptable solutions for valid track segments. Depending on whether the combination is 'in-cell', 'left-neighbouring' or 'right-neighbouring', short sequences of bins are grouped together from each of the corresponding three shift registers. Hence, a broad road through which tracks may have passed is created with these patterns. The patterns are presented to Content Addressable memories (CAMs), where valid track segment patterns are identified. The output of the CAMs is an unencoded address. As the CAMs need 2 clock cycles to compile the correct unencoded address, a validity bit is added to insure that the correct unencoded address is considered.

$\frac{1}{p_T}-\phi$ Mapping

During the final step of the track segment finder in this pre-L1Keep phase, a $\frac{1}{p_T}-\phi$ value is assigned to each of the track segments found. The assignment of a $\frac{1}{p_T}-\phi$ value to a

specific track segment is hardwired in the FPGA chip. This involves an "OR" between the selected address bits of the unencoded address from the CAMs. As the $\frac{1}{p_T}$ value of each valid track segment is known, a set of 16 trigger bits corresponding to the 16 curvature bins in the L1 histogram can be compiled. The 16 trigger bits together with the validity bit are then sent to the back FPGA.

Transfer to L1 Linker via Back FPGA

From each front FPGA on the FEM, the L1 trigger bits are sent to the back FPGA, where they are stored in a FIFO. Together with the data from the 4 other FPGAs on the FEM, the trigger bits are rearranged into 2 blocks of 48 bits of information. These are then transferred to the L1 Merger. Here, the data from several FEMs is merged. This time, the 48 bit blocks of data represent a specific region of the $\frac{1}{p_T} - \phi$ histogram. These are finally sent to the L1 Linker board, where the full track information is obtained (see section 3.5.2 page 46).

4.3.2 The Post-L1Keep Phase

Once a positive L1Keep signal has been received from the central trigger, the track segment finding algorithm is performed again. This time however, the track segment information is passed on to the FTT Level 2 system. The *L1Keep* signal is received ~ 2.3 μs after the t_0 of the event. By this time, the track segments found during the beam crossing of the event upon which the L1Keep signal was issued have moved by 18 bins on the shift registers clocked at 20 MHz corresponding to a time of 900 ns. As a consequence, the data processed in this second round is shifted backwards by 18 bins on the shift registers clocked at 20 MHz, with respect to the pre-L1KEEP steps. Once an L1Keep signal is issued, the pipelines are halted.

Extraction of Valid Track Patterns

The extraction of valid track segment patterns from the CAMs happens exactly as described in the pre-L1Keep step.

Priority Encoding

The further tasks are not processed in parallel mode because of the limited resources on the chip, and instead a 'Priority Encoding' circuit is used to encode the address bits of the valid track segments. The output of the priority encoder is a 12 bit word corresponding to one of 4096 possible address words. The output is ordered by address. The address that is compiled by the priority encoding circuit corresponds to a unique "mask number" of a particular valid track segment.

During the post-L1Keep phase, the L1 validity bit is used to start the priority encoder. Once the priority encoder has found a valid address, it generates its own validity bit which is used by the track segment finder in all further tasks. Addresses of track segments corresponding to the highest p_T tracks are encoded first.

In order to send the refined track segments to the L2 linker, the t and z information of the valid coarse track segments has to be regained. The priority encoding of the CAM address is a first step towards regaining this information.

Look-up of Valid Hit Combinations

Next, the shift register positions of the valid track segment combinations have to be retrieved. This is done by making use of a Read Only Memory (ROM). As the output of the priority encoder has a one-to-one relationship to the original hit combination on the 20 MHz shift registers, it is possible to retrieve the shift register positions for all possible valid "mask numbers" that are found. Up to 4096 different shift register positions can be stored in the ROM. Each of the three shift register positions for a track segment is encoded in a 5 bit address. As there are 3 shift register positions, which are associated to a valid track segment combination, each valid "mask number" is associated to one 15 bit address.

Retrieving the t and z Information

In this step, the finer granularity 80 MHz timing and z information is re-associated to the 20 MHz track segment. The shift register positions of the valid hits extracted in the previous step are now used to retrieve the 80 MHz information from the cyclic RAMs, which hold copies of the shift register information. Each cyclic RAM is associated to a specific shift register.

Depending on the encoded mask number, the shift register positions are used to retrieve the 80 MHz timing and z-information from the shift register copies representing either the 'left neighbour', 'in cell' or 'right neighbour' shift registers.

Collection of Track Segments and Refinement Information

The 12 bit output of the priority encoder as well as the validity bit are delayed for the time that is needed to collect the 80 MHz timing and z information. After all data is collected, the information is sent to the back FPGA where the refined track segments are validated (see section 4.3.2). Per valid track segment, the information sent to the back FPGA consists of a 36 bit word. It is composed of the 12 bit RAM address, the bit of information containing information about the half of the CAM the valid mask pattern originated from, the 2 bits of information containing the timing information and the 6 bits of information containing the z-information.

The Validation Step

The collected data from all 5 front FPGAs is collected by the back FPGA. The validity bit from the front FPGA tells the back FPGA which data should be processed. As the hit combinations are now known more precisely, simulation studies have shown that only approximately 50% of the 80 MHz masks can be extrapolated to the primary vertex position. The validation step thus rejects a large amount of background from random hit combinations. In order to validate an 80 MHz refined track segment, the 80 MHz mask number is composed at first. It is an 18 bit word, corresponding to the 12 bit 20 MHz track segment mask number together with the 2 bit timing information of each of the 3 hit positions. This word is fed to an external SRAM, where a 'validity' bit is added. The latter indicates whether the track segment was validated or rejected. If the segment is valid, a second look-up SRAM is used to obtain the remaining track parameters needed by the FTT L2 system (section 3.6 page 49). The word that is sent to the L2 boards contains 40 bits of information, corresponding to the $\kappa - \phi$ value of the valid track segment as well as the drift times and the z position of the 3 hits. Each FEM sends out 40 bits of data to the L2 boards per track segment that is kept.

4.4 Generation of Valid Track Segment Masks

The fast pattern recognition process uses a set of pre-defined valid track segment masks which it compares to the hit information available on the shift registers[§]. In order to find out which combination of hits can be combined into a track segment that originates from a track, a simulation program was written to study the matching of the drift times of all possible combinations from a group of three hits with the drift times of known track hits. Each combination of hits represents 3 hits in the r-ϕ plane. Assuming that the fourth space coordinate is the nominal vertex, a track combination of hits is a valid track segment if a circular fit through the space coordinates of the four points is possible. For each successful fit, the variance σ^2 of the fit is calculated:

$$\sigma^2 = \sum_{i}^{3} (x_i^{obs} - x_i^{fit}), \tag{4.1}$$

where x_i is the space coordinate of hit i. The fitting program that was written makes use of routines that are used for the offline reconstruction [56]. Thus, corrections between the drift time and drift distance are taken into account in the precise fit of the space coordinates.

Figure 4.4 shows part of the three shift registers of one trigger group as well as a track that validated the track segment. The figure shows the coarse binning (at a rate of 20 MHz) as well as the refined binning (at a rate of 80 MHz)[¶]. The corresponding bin widths are ~ 2500 ns and ~ 600 ns respectively. To keep the number of valid masks at a reasonable

[§]An explanation of shift register is given in 4.2.3 on page 51.

[¶]The coarse binning as well as the refined binning actually correspond to 20.8 MHz and 83.2 MHz respectively.

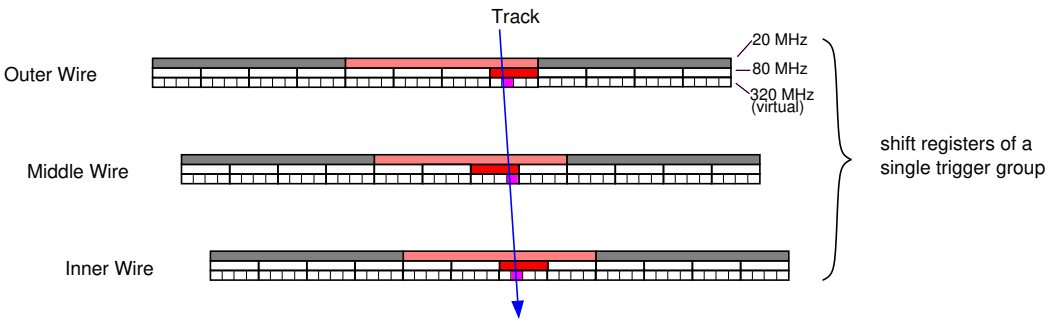

Figure 4.4: The generation of valid track segments is performed by checking all possible track segment masks for their validity. The sampling of the drift times is done at 20, 80 as well as 320 MHz.

level, each refined hit combination was checked for its importance. This was done by associating each valid track segment with a weight. For this, a virtual 320 MHz layer was introduced. Thus, for each 80 MHz bin, four hits are possible. The importance of each valid 80 MHz mask is measured by counting the number of valid 320 MHz hit combinations within a valid 80 MHz mask . Hence, the maximum weight per 80 MHz mask is $4^3 = 64$. This happens if all 320 MHz combinations for the corresponding 80 MHz mask are valid. In the same way, the importance of each valid 20 MHz mask is measured by counting the number of valid 80 MHz mask combinations.

As there are around 10^7 possible 320 MHz combinations per trigger group, it is impossible process all 320 MHz masks. Hence, before checking the importance of the valid 20 MHz hit combinations, the number of valid 20 MHz masks are stored. Table 4.1 shows the approximate number of valid track segments. The number of valid track segments depends on the variance cut that is applied on the fit. If a further cut on masks with low weights is applied, the number of valid track segments can be reduced further. In this way, a reduction of track segment masks from the 3^{rd} layer from 3300 to approximately 3100 masks means that 99% of the phase space is still covered. The number of masks also depends on the current calibration.

	1^{st} layer	2^{nd} layer	3^{rd} layer	4^{th} layer
20 MHz	≈ 1200	≈ 2000	≈ 3300	≈ 2800
80 MHz	≈ 20000	≈ 38000	≈ 60000	≈ 55000

Table 4.1: The number of valid masks that are found in the various trigger layers. The exact number mainly depends on the drift velocity in the different cells. The masks during positron running also differ from the masks during electron running as the nominal vertex for both settings are different.

4.5 Required Resources

The FPGAs which are used for the implementation of the Q-t Analysis as well as the track segment finding algorithm are Altera Apex20K400E chips. Each of these chips incorporate 16640 LEs corresponding to approximately 400000 gates. A set of 104 ESBs are available for the implementation of memory cells such as RAMs, FIFOs or CAMs [48]. The biggest requirements on FPGA resources arise on the front FPGA where the track segment finding takes place.

4.5.1 Resources on Front FPGA

The use of CAMs to store the 20 MHz track segment masks as well as a Look-up RAM in order to retrieve the shift register positions of the valid track segment hits requires a lot of resources.

Each CAM stores up to 32 entries per ESB. Hence, it would be necessary to use 96 ESBs to store 3072 masks in CAMs on one FPGA. As there are only 104 ESBs available inside each FPGA and because the Look-up RAM needs another 32 ESBs, the idea of using 96 CAMs per FPGA is not feasible. Thus, to save resources and maximise resource usage, the solution was to check the stored words twice by presenting two different hit combinations to the same CAM within one 20 MHz cycle. This halves the number of the resources to be used. As shown in figure 4.5, the input pattern that is fed to a single CAM depends on which half of the CAM is to be investigated. The trick is to write two valid track segments into each column of the CAM. In order to be able to check each column with two different input patterns, the valid track segment patterns are stored inside the CAMs using "don't care" bits. This means that each '0' belonging to a valid track segment patterns is replaced by an 'X'. This "don't care" bit accepts both a '1' and a '0' as a valid input. Hence, if one half of the input pattern is filled with a set of '1's and the other half of the input pattern is filled with entries from the shift registers, then the corresponding unencoded output bit is only validated if the '1's of the stored track segment pattern correspond to the '1's on the input pattern. In an alternating process, all valid track segments can thus be identified, by looping over the 1536 patterns stored in one half of the CAMs and then looping over the final 1536 patterns stored on the other half. This reduces the resources needed to identify all possible valid track segments from 96 down to 48 CAMs. A single bit is synchronised with the CAM output to provide information about which half of the CAMs the identified track segments originate from. This bit is also the lowest bit in the CAM address output of the priority encoder. Table 4.2 summarises the resource usage on the front FPGA.

[‖]The number depends on the time at which the z information, which is not needed during the pre-L1Keep phase, is added into the shift registers. During synthesis, unneeded shift register blocks are not implemented into logic.

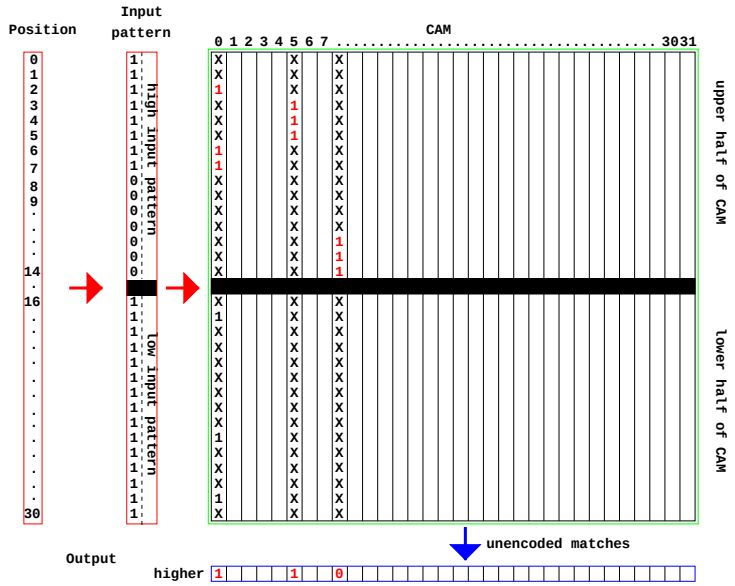

(a)

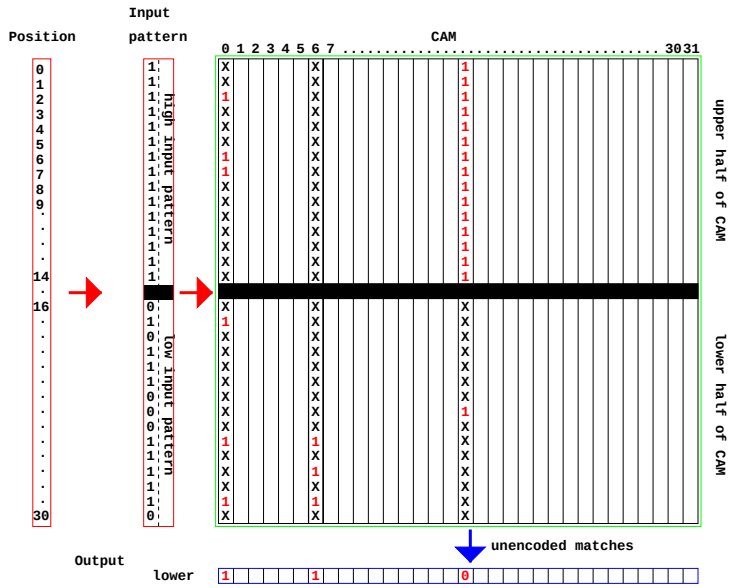

(b)

Figure 4.5: In figure (a), valid track segment combinations stored in the upper half of the CAM should be identified. The high input pattern is composed of selected sections from the three relevant shift registers and the low input pattern is composed of a series of '1's. As more than a single valid track segment may be identified, "don't care" bits, pictured as 'X', are used instead of '0's in the stored track segment patterns inside the CAMs. As the "don't care" bits accept '1's or '0's as a valid input, the low input pattern would automatically validate all unencoded output bits. Hence, the high input pattern decides which one of the 32 output bits is validated. In figure (b), the process is similar to the process shown in figure (a) except that valid track segment combinations stored in the lower half of the CAM should be identified in this case. Here, the low input pattern decides which one of the 32 output bits is validated. For more information see section 4.5.1.

Task	Number LEs	Number ESBs	Reference
Hit finding	886	12	simulated [57]
Charge division	804	/	simulated [57]
Shift registers	630	/	simulated‖
Cyclic RAM	338	5	simulated
CAM controller	5967	48	simulated
L1 Oring	666	/	simulated
Priority Encoding	5070	/	simulated
Lookup	41	32	simulated
Retrieve refined t and z	131	/	simulated
Collect segments	79	/	simulated
Control and IF	383	/	simulated
Total	$\sim$ 14864	97	

Table 4.2: This table shows the resource usage of all tasks performed by the track segment finding algorithm on the front FPGA in terms of logic elements (LEs) and embedded system blocks (ESBs).

4.5.2 Resources on Back FPGA

The back FPGA functions as an Input/Output Controller of the FEM, which results in nearly all the chip pins being used for data transfer. The implementation of dual ported FIFOs inside the back FPGA ensures that the data received from the different front FPGAs is re-synchronised to the 100 MHz clock which is used on the back FPGA. Further FIFOs are needed to store the respective data before they are sent on via the LVDS chain. A state machine controls the transfer of the data during the pre-L1Keep phase as well as the transfer of the data via the validation SRAM and the look-up SRAM during the post-L1Keep phase. As all FIFOs are implemented into ESBs, the transfer of the data should not use up a lot of logic elements.

4.6 The Main Control Unit of the Track Segment Finder

A flow diagram of the track segment finding algorithm is shown in figure 4.6. The algorithm can be broken into several units. Each unit performs a dedicated task.

One of the units is the *'control unit'* which controls the sequence of the different tasks which are performed by the algorithm. The 'control unit' checks two important input signals originating from the main H1 trigger system. These are the following:

- PiEn: if set, the pipelines are active;
- FClr_N: the fast clear signal is issued after the detector readout is completed or the event is rejected by either the L2 or L3 trigger. This signal tells the trigger

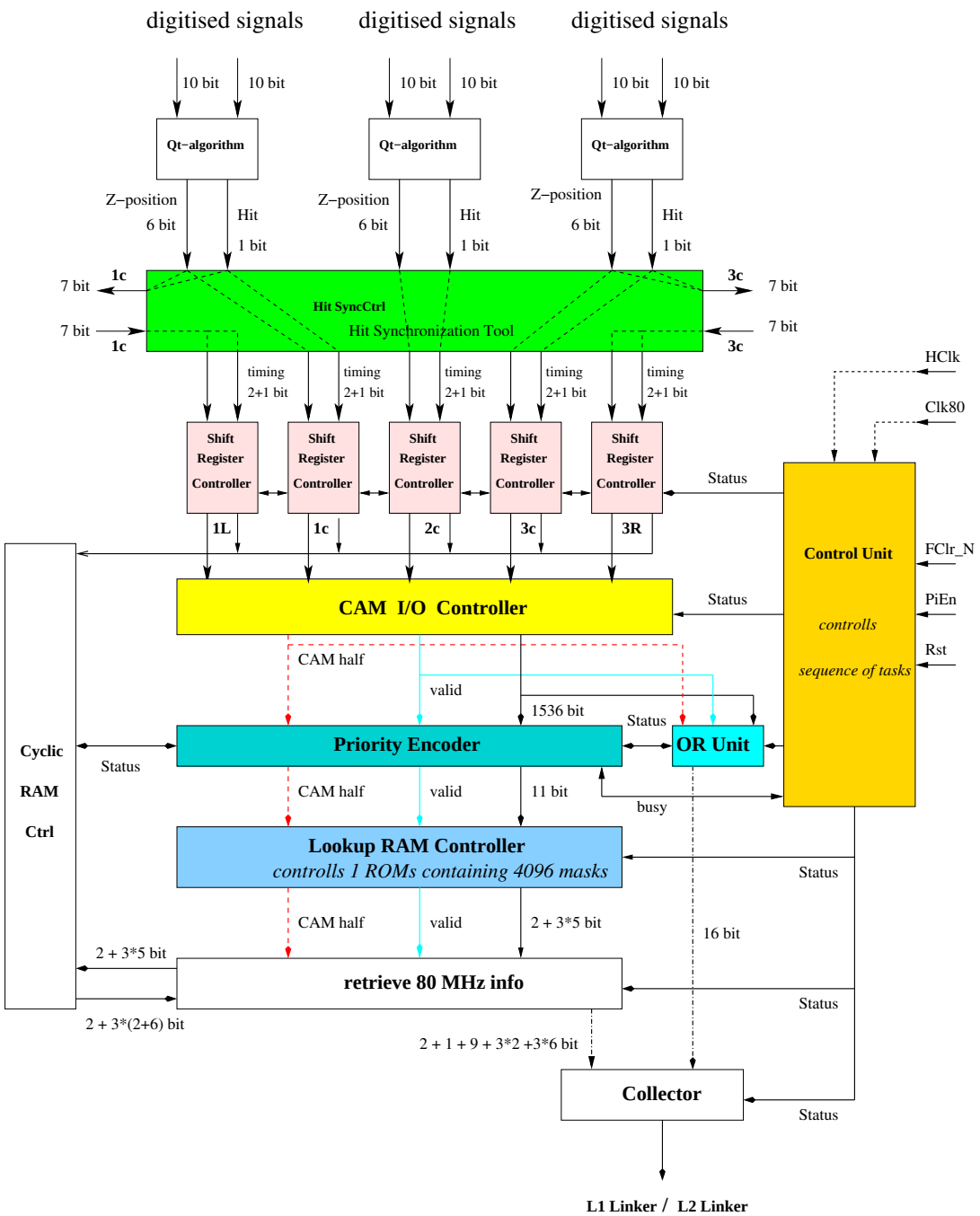

Figure 4.6: This figure shows a flow diagram of the track-segment finding algorithm. Each of the different boxes illustrates a particular control unit.

sub-systems that the pipelines will be activated again and data taking commences soon.

From these two signals alone, the different trigger stages, the pre-L1Keep and the post-L1Keep phases can be deduced. The HERA Clock, which is also received by the track segment finding algorithm determines the bunch crossing. For the internal organisation of the track segment finder, the following signals are also required:

- Rst: the asynchronous reset port;
- busy: this signal tells the main state machine whether the priority encoder is encoding addresses or not.

The 'Rst' signal is generated by the track segment finder once the chips are powered up. This enables the external phase lock loops (PLLs) to generate a clock signal which is 8 times the frequency of the bunch crossing (Clk80). Furthermore, this signal is used to clear the cyclic RAMs (which hold copies of the shift registers) after the post-L1Keep phase is finished. In order to perform fast switching, the 80 MHz clock is used. To enable timing checks, all other clocks are synchronised to this clock. 'Clk10' is the synchronised HERA clock. The 'Status' signal port is the only outgoing port of the control unit. The different states is as follows:

- "111": reset state or 'idle'
- "000": 'pre_L1active1' state
- "001": 'pre_L1active2' state
- "011": 'L1active' state
- "010": 'L23active1' state
- "100": 'L23active2' state
- "110": 'L23active3' state

Immediately after the 'Rst' signal is unset, the state of the control unit changes to the next state in the sequence. The change always happens synchronous to the 80 MHz clock (Clk80) and needs one cycle to propagate over the chip. In the 'pre_L1active1' state, the shift registers are cleared by filling them with zeros. This takes 23 HERA clock cycles and thus corresponds to the latency of the L1 trigger. Once all shift registers are cleared, the 'pre_L1active2' state waits for the pipelines to be re-enabled (PiEn='1'). Once the 'PiEn' signal is set, the control unit changes to the 'L1active' state. The post-L1Keep phase starts once the pipelines are halted (PiEn='0'). Three different states are necessary to control the patterns that are sent to the CAMs. During the first state ('L23active1') one half of the CAMs are checked. The state changes to the 'L23active2' state once the control signal 'busy', which is generated by the priority encoder, is set. Once the priority

encoder has finished the encoding of the addresses of the 20 MHz track segments, the state of the control unit changes to 'L23active3'. Now, the other half of the CAMs is searched for valid track segment matches. This last state only changes once the 'FClr_N' input signal changes (FCLr_N='0'). This signal tells the algorithm that a new event sequence is started. The state of the control unit sets to 'Idle'. The behaviour of the control unit is shown in figure 4.7. The corresponding VHDL code can be found in appendix A.

4.7 The Timing of the L1 Trigger Chain

The L1 linker needs to have transfered the FTT-L1 trigger elements to the central trigger within a latency of 2.1 μs. The central trigger needs a further 0.2 μs to take a trigger decision. The maximum drift time in the CJC is approximately 1.1 μs, so the timing of the algorithms during the pre-L1Keep phase is critical. In addition, the delays due to analogue cable delays, the digitisation and the transfer of the data from the FEMs to the L1 Linker board are unavoidable. The quoted delays in table 4.3 were obtained by simulation of the individual tasks. The testing in the actual hardware has not yet been performed. Limited by the specification of the CAMs, it is not possible to further optimise the track segment finding algorithm for tasks that are performed on the front FPGA during the pre-L1Keep phase.

Task	Latency (ns)	Cumulative time (ns)	Reference
Ionisation + drift to sense wires	1100	1100	measured
Analogue Cable delays	180	1280	estimated
FADCs	60	1340	specification
T Analysis + synchronisation	36	1376	simulated [57]
Write shift registers + synchronisation	60	1436	estimated**
CAM pattern generation	24	1460	simulated
1^{st} CAM match	24	1484	simulated
2^{nd} CAM match	24	1508	simulated
κ-ϕ mapping of 2^{nd} match	12	1520	simulated
collect L1 κ-ϕ bits	12	1532	simulated
collection of κ-ϕ on back FPGA	12	1544	estimated [58]
ORing of κ-ϕ bits	20	1564	estimated [58]
collection of 48 bit blocks in FIFO	10	1574	simulated [58]
transfer to L1 Linker via merger chain	231	1805	estimated [59]
Linking + topology	150	1955	estimated [54]
t_0 validation	100	2055	estimated [54]
transfer of TEs to central trigger	75	2130	estimated [54]

Table 4.3: This table shows the time resource usage of all tasks performed by the track segment finding algorithm on the front FPGA. The timing to get the z-information from charge division is not included.

Estimates of the pre-L1Keep timing are given in table 4.3. Currently, the timing is

**It was assumed that the hit information from the adjacent cells needs 12 ns to be transferred from the adjacent FPGA.

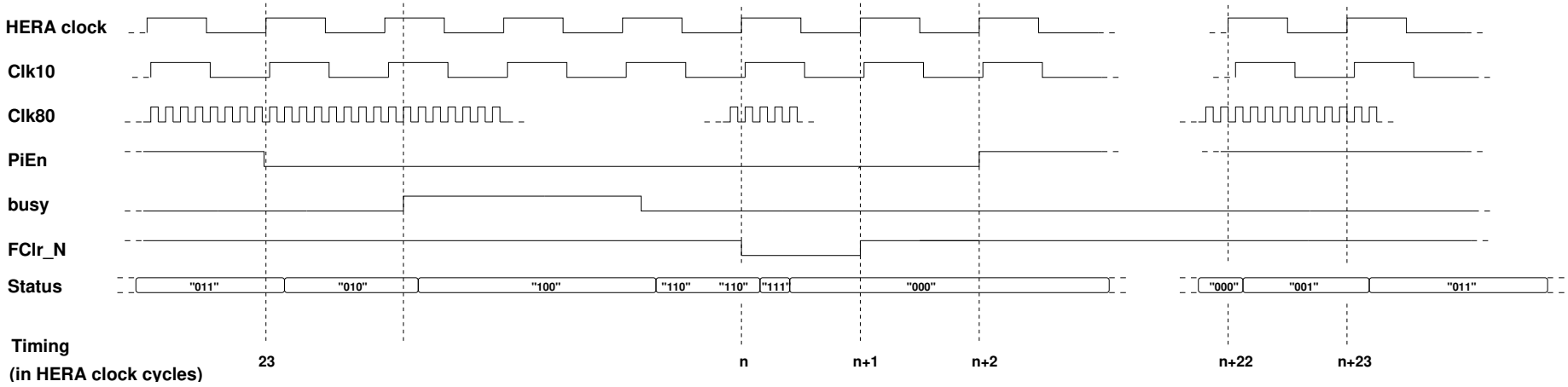

Figure 4.7: The control unit of the track segment finder uses the incoming control signals 'PiEn', 'FClr_N' and 'busy' to determine the sequence of states. The 10.4 MHz HERA clock as well as the HERA clock (Clk10), which is synchronised to the 83.2 MHz clock (Clk80), is shown. The outgoing 'Status' bits are used by the track segment finding algorithm to switch tasks if necessary.

very tight corresponding to the available 2.1 μs. As the cable length was conservatively estimated to 15 m it may still be possible to reduce the cable length by a further 3 m. Further improvement may be possible by optimising the t_0 validation algorithm. If these improvements are not adequate, a fall-back solution has been investigated whereby hits from the longest drift times (> 1.0 μs) are ignored in the processing of L1 trigger elements. Such long drift times only occur in the outermost trigger layer of CJC1, so that the hits represent only 1% of all hits [60] and their retention is not critical.

4.8 Timing of the Track Segment Finder during the Post-L1Keep Phase

During the post-L1Keep phase, the timing is not as critical as during the pre-L1Keep phase. Assuming that the track segment finder takes 0.3 μs to transfer the first refined track segments, the FTT-L2 algorithms take 17.7 μs to compile the L2 trigger elements [45]. This leaves enough time to transfer the results to the central trigger which takes a decision within the L2 latency of 20 μs.

The timing estimates of the track segment finding algorithm during the post-L1Keep phase are shown in table 4.4. The table only shows the timing for the track segment finder to collect the first refined track segment before sending it to the L2 boards if it is valid. For each further refined track segment that is found, the algorithm needs an additional 12 ns. To find all refined track segments, the algorithm is run twice during the post-L1Keep phase. The delay between the first and the second runs is 24 ns. A maximum of 128 refined track segments are accepted by the L2 boards. Hence, the 128^{th} track segment leaves the back FPGA 1858 ns after L1Keep was set.

Task	Latency (ns)	Cumulative time (ns)	Reference
read shift register	12	12	simulated
CAM pattern generation	24	32	simulated
CAM match	24	60	simulated
1^{st} word from priority encoder	60	120	simulated
lookup	12	132	simulated
retrieving refined t and z	48	180	simulated
collect segments	12	192	simulated
transfer to back FPGA	12	204	estimated
Validation step	60	264	estimated [58]
Lookup of refined (κ-ϕ) values	60	324	estimated [58]
Write into output FIFO	10	334	estimated [58]

Table 4.4: This table shows the time resource usage of all tasks performed by the track segment finding algorithm on the front FPGA.

4.9 Summary

In this chapter, a detailed description of the track segment finding algorithm has been presented. During the pre-L1Keep phase, the track segment finder processes the L1 data in a highly parallel way. Approximately 1500 ns after the hit information of the Q-t analysis has entered the track segment finding algorithm, coarse track segments are found and the corresponding $\frac{1}{p_T} - \phi$ trigger bits have been collected. These are then sent to the L1 linker boards where the linking takes place. The linking of the coarse track segments as well as the compilation of trigger elements finishes 1955 ns after the event t_0. If the decision were not to issue an FTT t_0 trigger element, this would mean that the data will arrive at the central trigger at a time of 2030 ns after the event t_0 and over 0.2 μs would be left for the central trigger to take a trigger decision. Although the CIP/COP z-vertex trigger also issues an event t_0 trigger element, it is advisable that the FTT issues such a trigger element too. The compilation of an FTT t_0 trigger element means that the timing is more critical as the data then arrives 30 ns late. However, by further optimising the t_0 validation algorithm, the timing should be fine. In the case where such an optimisation is not possible, a fall-back solution was studied, whereby hits with long drift distances above 1 μs are ignored. In this case, only 1% of the hits are lost. During the post-L1Keep phase, the pipelines are halted and refined track segments originating from the L1 triggered event are searched for. As the timing during this phase is not critical, a priority encoding circuit is used to serialise the data output. The encoded address from the priority encoder is the mask number of the valid 20 MHz track segment. This enables the serial lookup of the shift register positions of the valid coarse track segments and is a first step to retrieve the ignored 80 MHz information that was filled into the shift registers during the pre-L1Keep phase. After retrieving the 80 MHz timing and z information, the data is collected and sent to the back FPGA. Together with the data of the 4 other front FPGAs, the refined track segments are validated. Then, after the lookup of the corresponding L2 ($\kappa - \phi$) histogram entries, the information is sent on to the L2 boards.

It has been shown that the limited resources on the front FPGA are sufficient, provided that the CAMs are used in an optimal way. By looping over the CAM content twice, with different input patterns each time, it is possible to check alternative CAM halves for valid track segments. Through the optimal usage of the CAM resources a reduction from initially 96 down to 48 CAMs was reached.

Chapter 5

Simulated FTT Performance Studies

5.1 Introduction

This chapter starts with the introduction of the Monte-Carlo simulations used to study the various processes investigated from the point of view of the FTT in this thesis. It is followed by a brief description of the detector response, as well as a short introduction to the program FTTEmu 4.04 which simulates the FTT. Then, results on the FTT L1 and L2 track resolutions as well as the track efficiencies are presented. The section on track based performances presents the track finding efficiencies and the track purities for different processes. The FTT is being commissioned at the time of writing. Hence only simulated events and real data from the HERA I setup were used for these studies. Finally, the efficiency and timing resolution of the FTT T0 trigger element is investigated for different processes.

5.2 Monte-Carlo Simulation

In a physics analysis at H1, Monte-Carlo (MC) simulations are generally used to correct the data for the detector acceptance and efficiency. Furthermore, contributions to the signal region from background processes can be studied. In the implementation, MC events are generated assuming a specific physics production mechanism.

5.2.1 Monte-Carlo Event Generators

Different MC event generators can be used to generate the hard sub-process underlying the ep interaction. This sub-process is generated according to the perturbative QCD (pQCD) cross-section at leading order. In this thesis, three different MC event generators were used.

- The charged current event generator **DJANGO** is used to generate the hard subprocess according to the MRSH [61] parameterisations for the parton density functions.
- The **PYTHIA** [62] event generator uses the GRV parton density functions to generate a leading order cross section for photoproduction processes. In this thesis, direct, resolved as well as prompt photons are considered.
- The **DIFFVM** [63] program is used to generate diffractive $\gamma p \rightarrow J/\psi\ p$ events. A detailed description of the parameters used can be found in [64]. This MC program is also used to generate $\gamma^{\star} p \rightarrow \rho^0\ Y$ events [65].

The fragmentation of the partons into hadrons is simulated using the *JETSET* [66] program. Two or more partons linked with colour strings are hadronised as described by the "Lund-String Model". The parameters used in this model have been adjusted to describe the H1 data. The resulting hadrons (and electrons) are then presented to the detector simulation.

5.2.2 Detector Simulation

The detector response to the particles generated in a Monte Carlo event is simulated in detail in the detector simulation program *H1Sim* [67] which makes use of the *Geant3* [68] program. In order to properly simulate the interactions between particle showers and the detector elements with acceptable speed, the program *H1FAST* [69] [70] is used. To save computer time, it uses fast parameterisations to describe the energy development of the electromagnetic and hadronic showers in the calorimeters. As the detector has a wide though limited geometrical acceptance, not all generated particles will be detected. The simulated MC events are also subject to the trigger simulation program *H1Trig*. Hence, the trigger response one obtains from the MC simulation can be compared to the information from the data. One of the programs which will eventually be part of *H1Trig* is the program FTTEmu. It simulates the trigger response of the FTT over the three first stages of the H1 Trigger system. A more detailed description of this program can be found in [45].

5.3 FTT Track Resolutions

In order to determine the resolutions of the track parameters θ, ϕ and $\frac{1}{p_T}$, the results of the FTT are compared with the offline calculations using the CJC reconstruction. This is done for both level 1 and level 2.

5.3.1 Level 1 Track Resolutions

With the objective of achieving optimal resolution for tracks over the full p_T range, the non-linear histogram binning scheme shown in table 5.1 was chosen.

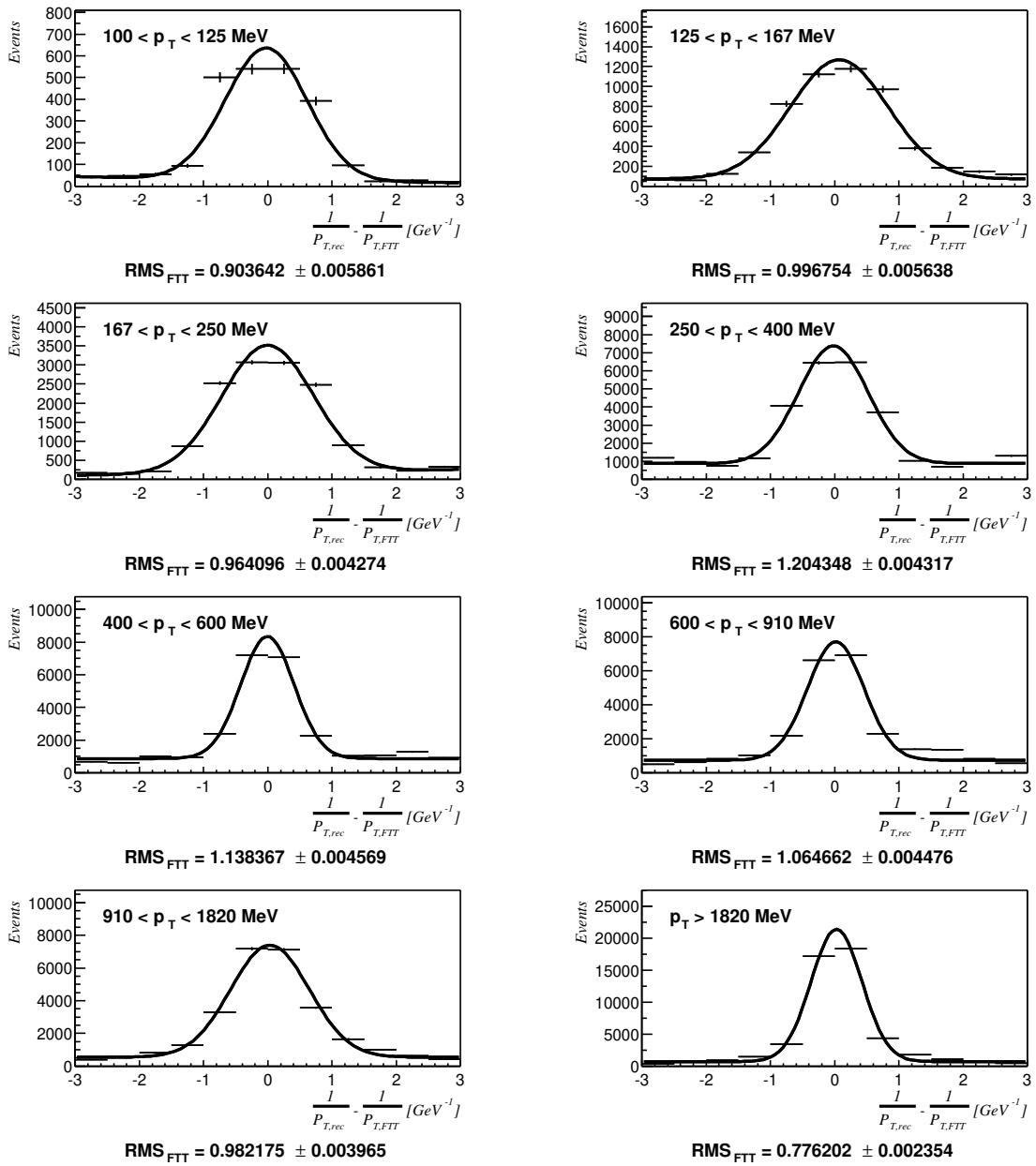

Figure 5.1: The $\frac{1}{p_T}$ resolution of tracks from NC events are shown in different bins of p_T. Only offline tracks within the FTT acceptance are used. The histograms show the difference between $\frac{1}{p_T}$ as reconstructed off-line and as obtained from FTTEmu. The RMS of each distribution is indicated.

bin	lower p_T edge [MeV]	higher p_T edge [MeV]
1	100	125
2	125	167
3	167	250
4	250	400
5	400	600
6	600	910
7	910	1820
8	1820	∞

Table 5.1: The above table lists the p_T values of the lower and upper bin edges used to define the L1 linking histogram.

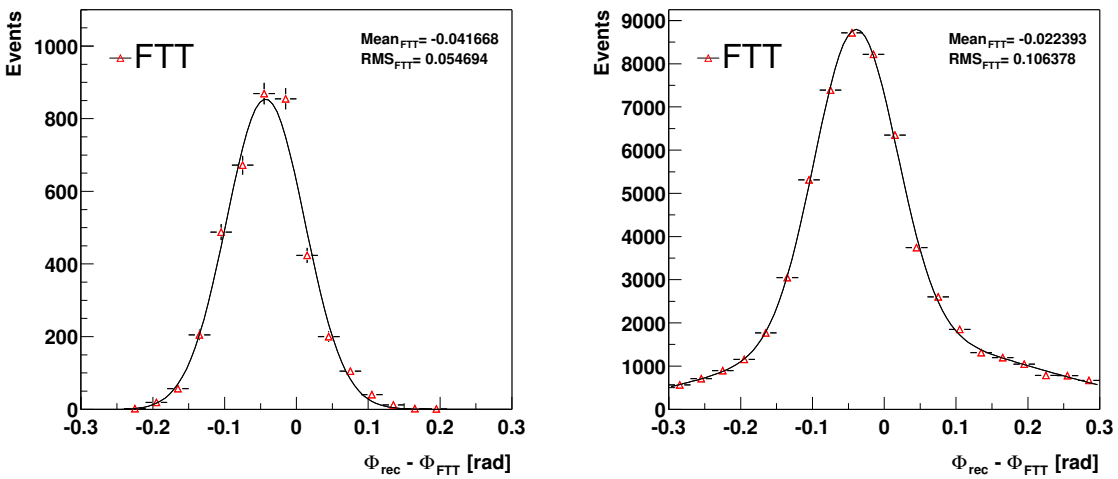

(a) *(b)*

Figure 5.2: The L1 resolutions in the ϕ coordinate are shown for (a) $\gamma p \rightarrow J/\psi\ p$ data sample as well as (b) for NC events.

Figure 5.1 shows the resolution of the $\frac{1}{p_T}$ track parameter based on a simulation of neutral current data events. All offline tracks and FTT-L1 reconstructed tracks were chosen to lie within the FTT acceptance of [25°,155°]. The study was performed comparing the inverse p_T of the offline reconstructed track with the mean p_T value of the corresponding bin which holds the associated FTT-L1 reconstructed track. It can be seen that the resolution is approximately constant at $\frac{\sigma(p_T)}{p_T^2} \approx 1$ GeV^{-1} for the lower p_T bins and that the resolution is slightly better for the highest p_T bin with $\frac{\sigma(p_T)}{p_T^2} \approx 0.77$ GeV^{-1}. The better resolution of high p_T tracks can be explained from two arguments. Firstly, multiple scattering mainly takes place at low values of p_T. Thus, the track segments have poorer resolution for low p_T tracks. Secondly, low p_T tracks of around 100 MeV are generally linked from only two track segments by the FTT reconstruction, whereas tracks of $p_T \sim 2$ GeV are linked from 3 or 4 track segments. As the track resolution increases with the number of track links [71], high p_T tracks have a better resolution.

In figure 5.2, the resolution of the FTT track parameter ϕ is shown for (a) a selected

$\gamma p \rightarrow J/\psi\, p$ data sample and (b) a NC data sample. With effectively 30 bins in ϕ, the expected optimal resolution is approximately 0.06 rad. Considering J/ψ events, where all tracks have a $p_T > 0.8$ GeV, the resolution of the L1 track parameter is only slightly below the expected best value. This is due to the fact that the J/ψ photo-production sample only includes well isolated tracks separated by approximately 180° in the ϕ coordinate and thus is a very clean sample. For the Neutral Current data sample, however, the resolution is approximately a factor 1.5 worse than the expected resolution. One explanation is that low p_T tracks from the NC hadronic final state worsen the resolution due to multiple scattering. Furthermore, high multiplicity events including jets create a high number of track segments. Although most of the space-time ambiguities are resolved during the linking process, some of the track segments can be linked to ghost tracks.

5.3.2 Level 2 Track Resolutions

At the second level, the 80 MHz refined track segment information used for the linking process as well as the additional track fitting procedure considerably improve the track resolutions. Hence, the expected optimal resolutions in $\frac{1}{p_T}$, ϕ and θ are $\frac{\sigma(p_T)}{p_T^2} \approx 0.04$ GeV^{-1}, $\sigma(\phi) \approx 5$ mrad and $\sigma(\theta) \approx 100$ mrad, respectively. Figure 5.3 shows the resolutions of the three different track parameters $\frac{1}{p_T}$, ϕ and θ in the case of the J/ψ photo-production process. Again, only tracks above 0.8 GeV were selected. It can be seen that for the clean photo-production process, the resolutions of all three track parameters are very good, although they do not fully match expectations. The resolutions of the L2 track parameters mentioned above are also shown using the CC data sample (see figure 5.4). For this high multiplicity process, the resolutions of the FTT track parameters are worse than for the J/ψ photoproduction process but are still consistent with the design specifications.

5.3.3 Performance of L1 Linker

To find out more about the performance of the linking method used at the first level of the FTT, the fraction of tracks that are reconstructed with the same sign than the FTT reconstructed track are compared to its offline associated counterpart is studied as a function of the transverse momentum of the offline reconstructed track.

In order to make sure that all tracks are well isolated, the following criteria were used to select the events:

- $|\phi_{track,i} - \phi_{track,j}| > 40°$,
- $n_{max} = 6$,
- $|\phi_{track,offline} - \phi_{track,FTT}| \leq 3 \cdot \sigma_{\phi(L1)}$,
- $25° < \theta_{track,offline} < 155°$,

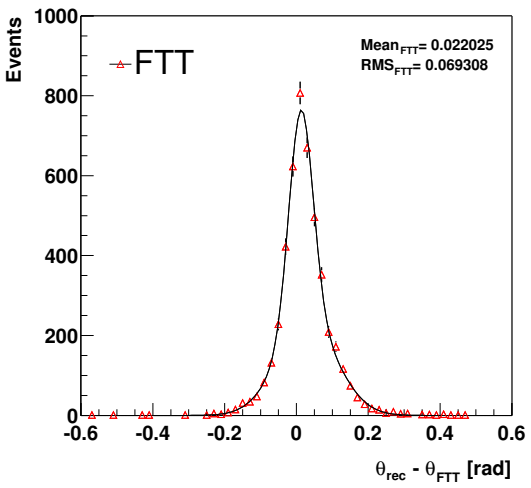

(a)

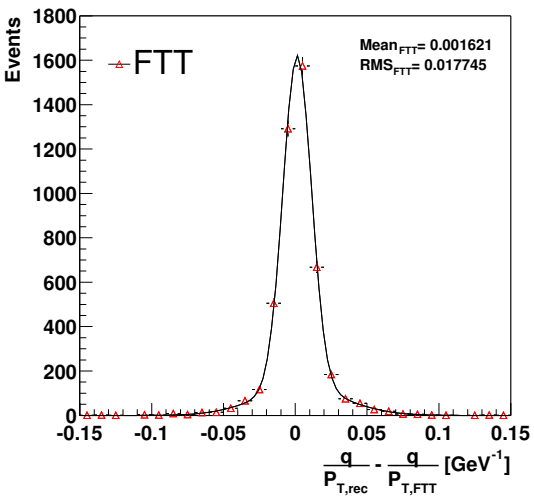

(b)

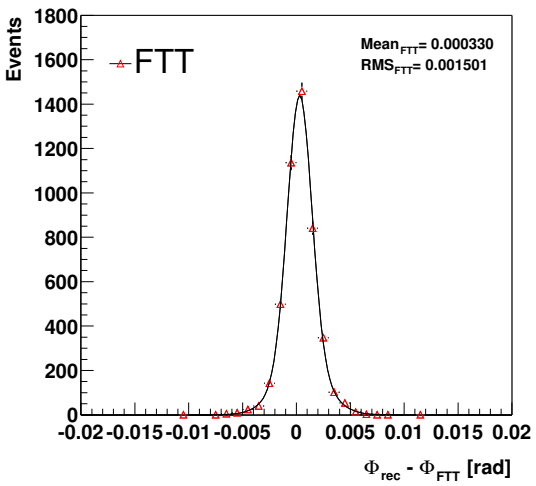

(c)

Figure 5.3: L2 resolutions of the parameters (a) θ, (b) $\frac{1}{p_T}$ and (c) ϕ of the FTT reconstructed tracks relative to the offline reconstructed tracks are shown for the elastic $J/\psi \rightarrow \mu^+\mu^-$ photo-production sample.

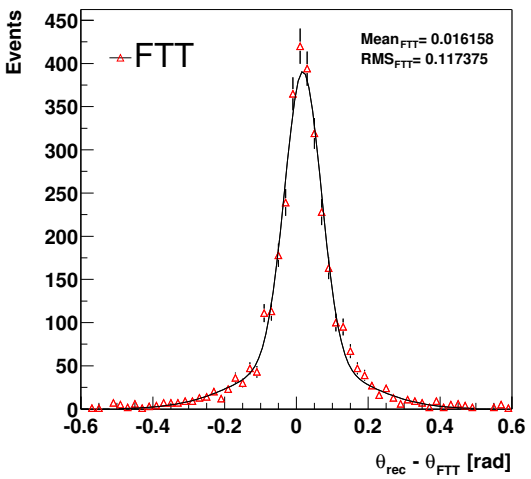

(a)

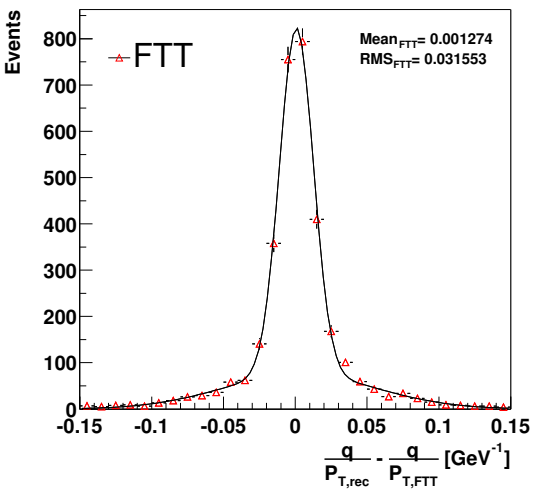

(b)

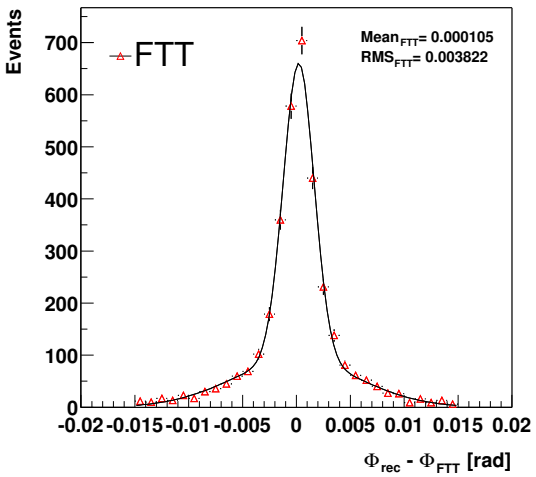

(c)

Figure 5.4: L2 resolutions of the parameters (a) θ, (b) $\frac{1}{p_T}$ and (c) ϕ of the FTT reconstructed tracks relative to the offline reconstructed tracks are shown for the CC data sample.

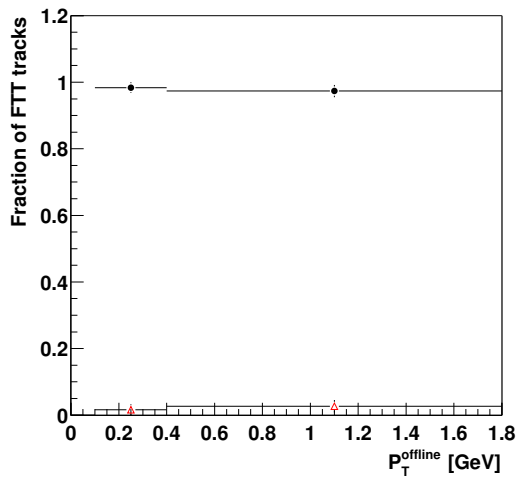

(a)

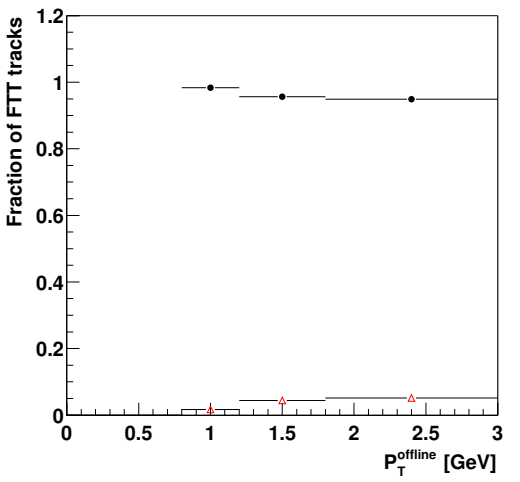

(b)

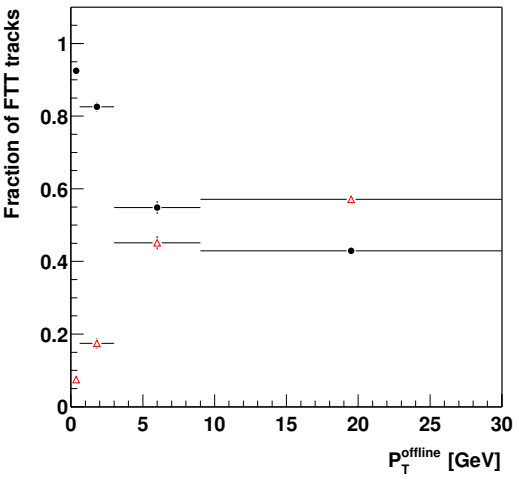

(c)

Figure 5.5: The fraction of offline reconstructed tracks associated to FTT reconstructed L1 tracks with the same curvature sign (dots) as well as the fraction of offline reconstructed tracks associated to L1 tracks with the opposite curvature sign (triangles) are shown as a function of the p_T of the associated offline track. The three figures show these fractions in the cases of (a) the $\rho^0 \rightarrow \pi^+\pi^-$ electro-production process, (b) the elastic $J/\psi \rightarrow \mu^+\mu^-$ photoproduction process and (c) the NC process. The selection only includes tracks originating from the nominal bunch crossing.

where n_{max} is the maximum number of tracks in the acceptance region of the FTT and $\sigma_{\phi(L1)}$ is equal to 18°. Hence, no effects due to wrong track assignment can influence the investigation.

Figure 5.5 shows this fraction for the electro-produced ρ^0 data sample, the $\gamma p \rightarrow J/\psi\, p$ data sample and the NC data sample. In all three figures it can be seen that the fraction of FTT reconstructed tracks that have the opposite curvature sign compared to its offline counterpart rises as a function of the p_T of the offline associated track. The results are similar for all three processes. At a transverse momentum of approximately 5 GeV, the fraction of FTT reconstructed tracks with the wrong curvature is equal to the fraction of FTT reconstructed tracks with the correct curvature. This means that the L1 trigger cannot determine the charge of the reconstructed track any longer.

5.4 FTT Track Efficiencies and Purities

The probability of finding a track in the CJC depends on the single hit efficiency ϵ_{SH} of the trigger wires of each single trigger group. Only if a hit is detected by the three wires of a trigger group can a track segment be defined. Thus, the probability P_{seg} for a track segment to be found by a particular trigger group once a particle passed nearby, can be described by the following equation:

$$P_{seg} = \epsilon_{SH}^3. \tag{5.1}$$

Then, taking into account that a two out of four coincidence is required between trigger layers, the probability P_{tr} to link the track segments to form a track can be determined from the following equation:

$$P_{tr} = \sum_{i=2}^{4} \binom{4}{i} P_{seg}^i (1 - P_{seg})^{4-i}. \tag{5.2}$$

Given that the single hit efficiency is approximately 95%, the efficiency of reconstructing a track due to a particle that passed both central jet chambers CJC1 and CJC2 is $\simeq 99$ %.

The track efficiency is defined as follows:

$$\varepsilon = \frac{FTT \wedge \text{offline}}{\text{offline}}, \tag{5.3}$$

where *offline* denotes the number of offline reconstructed vertex-fitted tracks and FTT denotes the number of FTT reconstructed tracks. As all FTT reconstructed tracks are required to originate from the nominal vertex, the track efficiencies were determined from vertex fitted offline tracks only.

5.4.1 L1 Track Efficiency

Figure 5.6 shows the L1 track efficiency as a function of the track parameter p_T as measured offline. For this figure, a proton-dissociative ρ^0 MC sample was used with the cuts. Furthermore, only events that pass the L1 track criteria mentioned in section 5.3.3 on page 72 were chosen. It can be seen that the track efficiency rises from 95% for tracks with a p_T below 0.4 GeV to 97% for tracks with a p_T above that value.

5.4.2 L2 Track Efficiency and Purity

The track purity is defined as a ratio of the number of offline reconstructed tracks found by the FTT to the total number of FTT reconstructed tracks. This can be written down mathematically as follows:

$$\varepsilon = \frac{FTT \wedge \text{offline}}{FTT}. \tag{5.4}$$

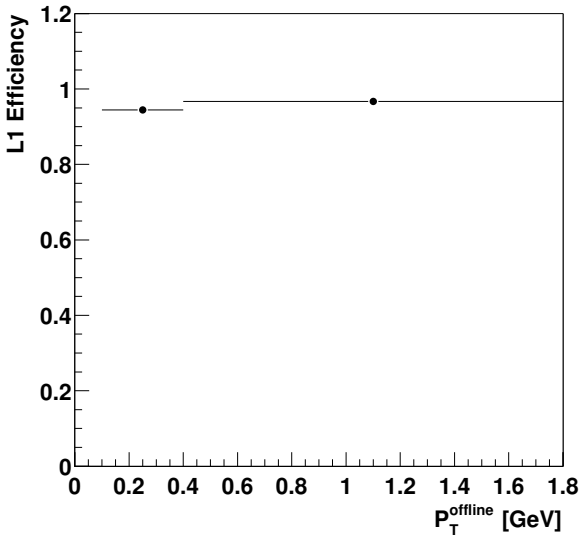

Figure 5.6: The L1 track efficiency is shown as a function of the offline transverse momentum.

Although the FTT was built to reconstruct vertex fitted tracks only, it is possible that tracks originating from secondary particles are found. As these tracks should not be considered as ghost tracks, the purity was determined using non-vertex fitted tracks. The L2 track efficiencies as well as the track purities have been determined using events with isolated tracks as was the case for the L1 track efficiency. The improved resolution permits a slight change in the isolation criteria:

- $|\phi_{track,i} - \phi_{track,j}| > 5°$,
- $n_{max} = 6$,
- $|\phi_{track,offline} - \phi_{track,FTT}| \leq 3 \cdot \sigma_{\phi(L2)}$,

where $\sigma_{\phi(L2)} = 5$ mrad is the expected L2 resolution of the FTT reconstructed ϕ track parameter.

Figure 5.7 shows the track finding efficiency as a function of the track parameters θ, p_T and ϕ in the case of the $ep \rightarrow \rho^0 Y$ Monte Carlo sample. Figures 5.7(b) and 5.7(c) are shown with the additional offline acceptance cut applied. It can be seen that the L2 track efficiency at low p_T shown in figure 5.7(b) is lower than the L1 track efficiency in figure 5.6. Indeed the refined L2 track segments are a sub-sample of the coarser L1 track segments as not all track combinations of 80 MHz hits from the three trigger wires within the 20 MHz mask are valid. Hence, only part of the L1 phase space is covered by L2. The track efficiency for pion tracks with a p_T below 0.5 GeV drops from 95% at L1 down to approximately 75% at L2.

For the $ep \rightarrow \rho^0 Y$ process, the purities of the track parameters θ, p_T and ϕ are shown in figure 5.8. Again, the Monte-Carlo sample was used. The above mentioned acceptance

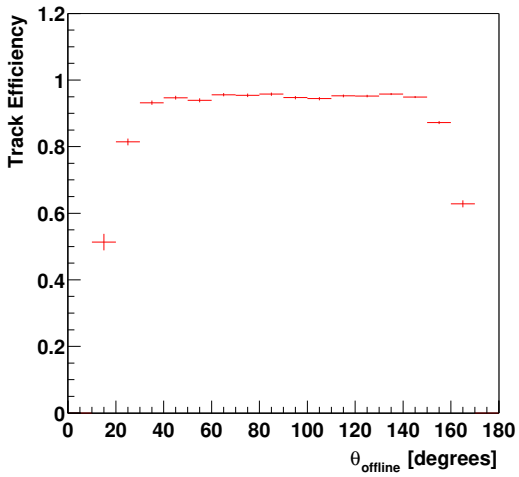

(a)

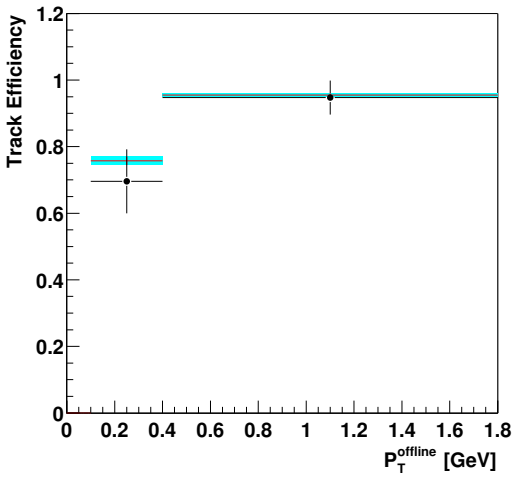

(b)

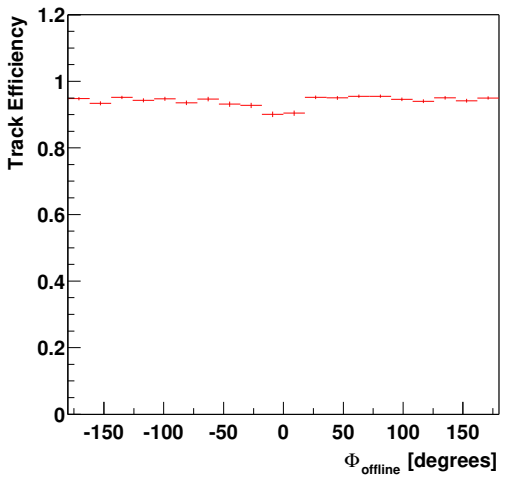

(c)

Figure 5.7: The L2 track finding efficiencies are shown as a function of the track parameters (a) θ, (b) p_T and (c) ϕ. In figure (b) the efficiency is shown for data (dots) as well as Monte-Carlo. The error on the Monte-Carlo is shown by the shaded band. For both data and MC, only events triggered by the independent monitor trigger ST0 were selected.

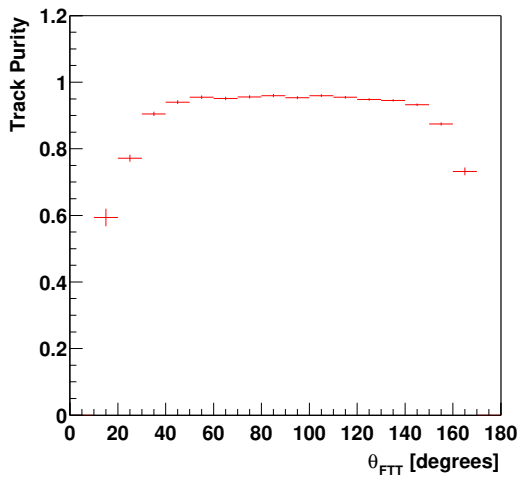

(a)

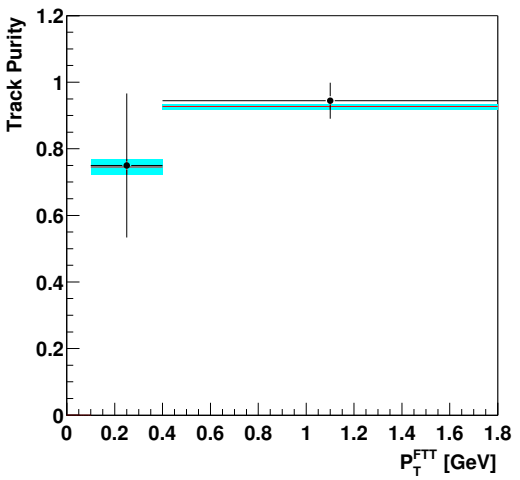

(b)

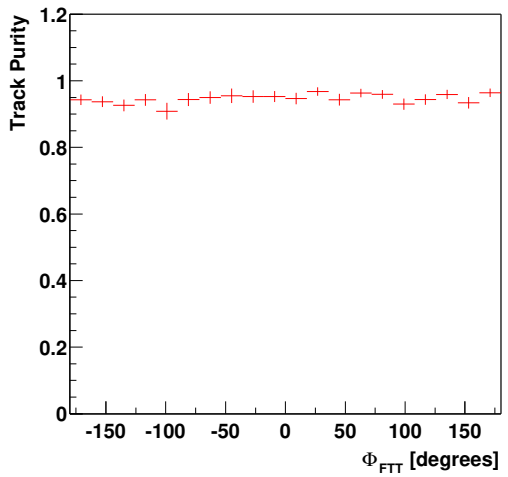

(c)

Figure 5.8: The L2 track purities are shown as a function of the track parameters (a) θ, (b) p_T and (c) ϕ. In figure (b) the efficiency is shown for data (dots) as well as Monte-Carlo. The error on the Monte-Carlo is shown by the shaded band. For both data and MC, only events triggered by the independent monitor trigger ST0 were selected.

cut $25° < \theta < 155°$ was applied in figures (b) and (c). The overall purity in the acceptance region is 95%. For low p_T tracks, the purity is slightly lower.

The efficiencies as a function of the three L2 track parameters θ, p_T and ϕ have also been investigated in the case of the NC process and the results are shown in figure 5.9. Noticeable is the high track efficiency in the backward region of the CJC ($100° < \theta < 160°$) as shown in figure 5.9(a). The high track efficiency is due to the scattered electron that is reconstructed. The jet consists of lower p_T tracks and is mainly directed in the forward region of the CJC.

The track purities from an NC data sample are shown in figure 5.10 in the usual format. Figure 5.10(a) shows that the purity of tracks at large values of theta is approximately 99 % whereas at values of theta below 40° the purity decreases to approximately 55 %. This is again due to the fact that the scattered electron is found at high values of θ. From

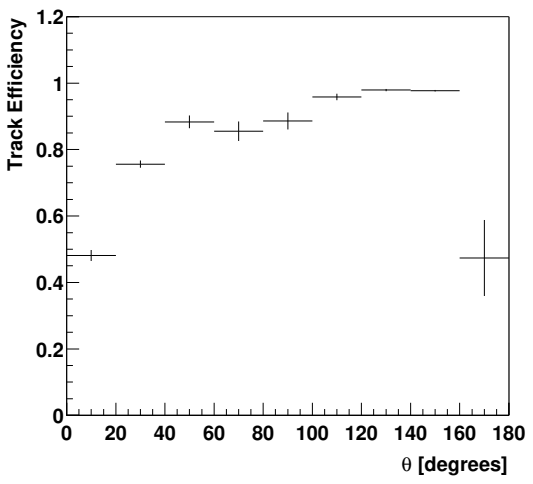

(a)

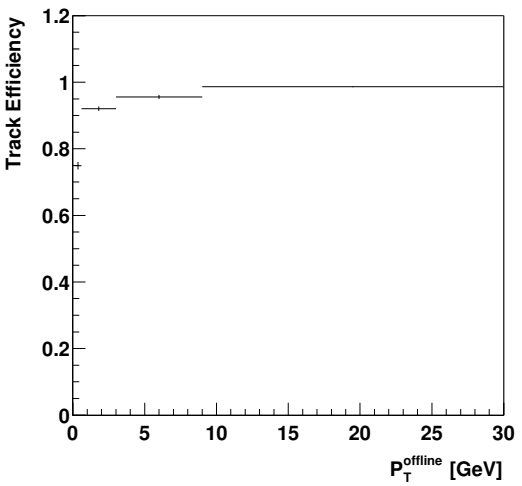

(b)

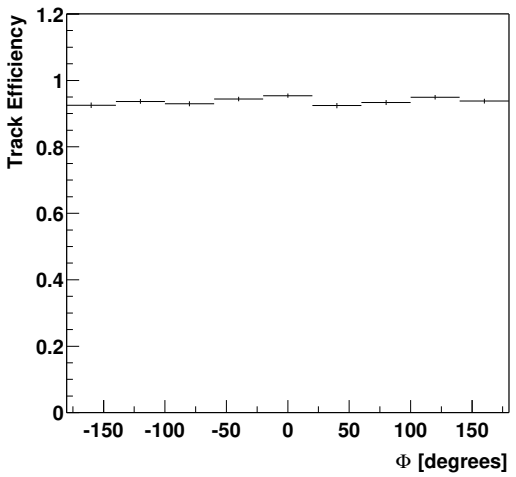

(c)

Figure 5.9: The L2 track finding efficiencies are shown as a function of the track parameters (a) θ, (b) p_T and (c) ϕ. A NC data sample was used. For both data and MC, only events triggered by the independent monitor trigger ST67 were selected.

figure 5.10(b), it is seen that tracks with p_T below 0.5 GeV have a purity of less than 30 %.

Figure 5.11(a) shows the track finding efficiency as a function of track multiplicity. It can be noticed that the track finding efficiency is at approximately 99 % if only one offline track is present within the acceptance region of the FTT. Once a higher number of offline tracks are present, the track finding efficiency drops to approximately 90 %. Figure 5.11(b) shows the electron finding efficiency as a function of the offline track multiplicity in the acceptance region of the FTT. It can be seen that the efficiency remains at approximately 99 % for all track multiplicities. Hence it can be concluded that whenever only one track is seen within the acceptance region of the FTT or when the track is well isolated as is the case for the scattered electron, the efficiency is very high.

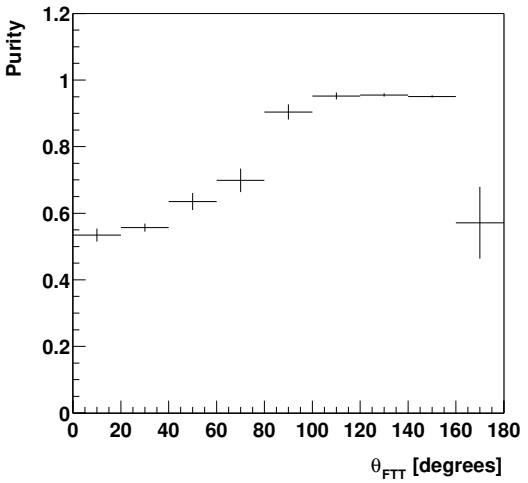

(a)

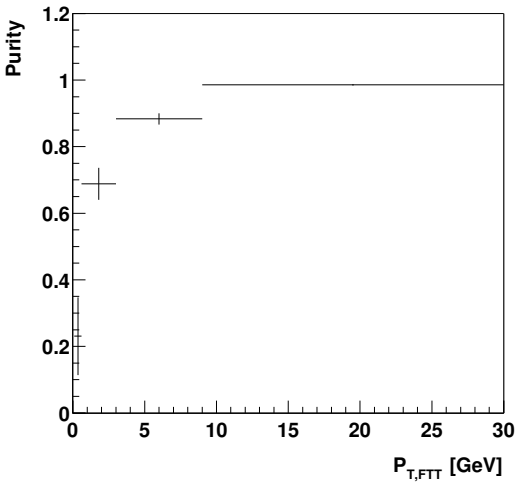

(b)

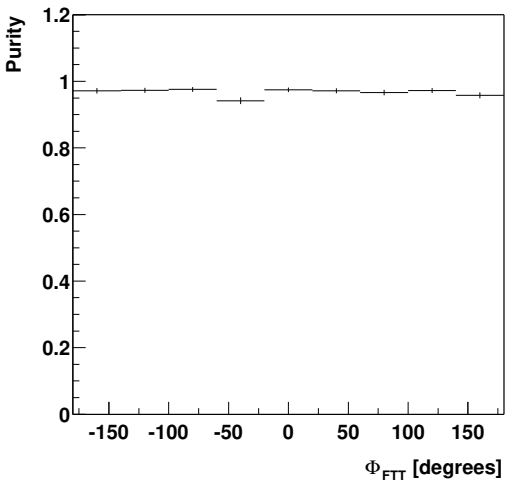

(c)

Figure 5.10: The L2 track purities are shown as a function of the track parameters (a) θ, (b) p_T and (c) ϕ. A data sample of selected NC events that were triggered by an independent LAr Calorimeter based monitor trigger was used.

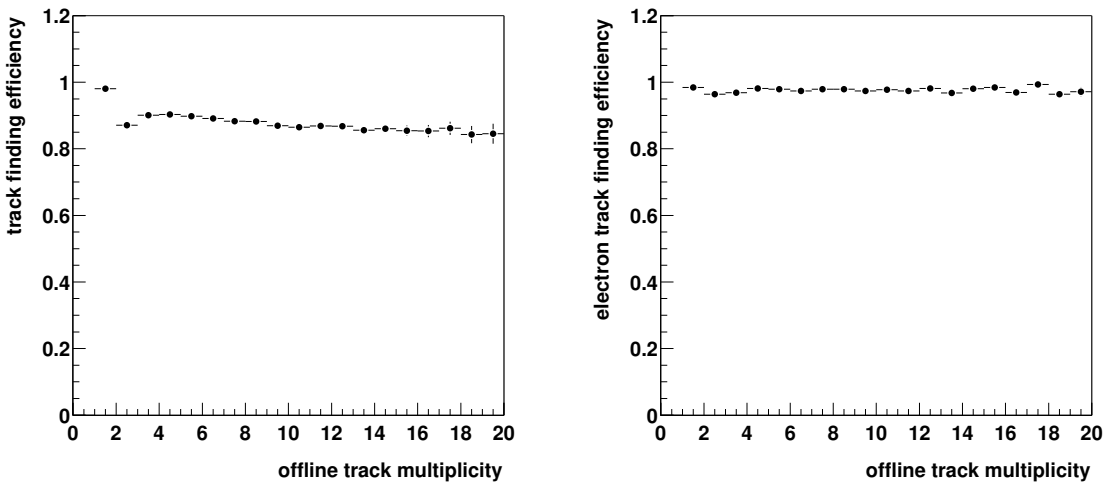

(a) *(b)*

Figure 5.11: (a) The track finding efficiency and (b) the efficiency to find the electron track are shown as a function of the offline track multiplicity in the event. A data sample of selected NC events, that were triggered by the independent LAr Calorimeter based monitor trigger, was used.

Figure 5.12(a) shows the correlation between the number of tracks reconstructed by the FTT and the number of offline reconstructed tracks. Figure 5.12(b) shows the correlation between the number of tracks found by the FTT and the offline reconstruction in the FTT acceptance region. In both figures, a clear correlation is present. In high multiplicity events, such as NC events, it is possible that the FTT finds more tracks than the offline reconstruction. This is due to ghost tracks.

In figure 5.13, the ratio of the track efficiencies for tracks with a negative curvature and tracks with a positive curvature is shown as a function of the transverse momentum of the track. It can be seen that the negatively charged tracks have a higher efficiency than the positively charged ones if the p_T of the track is below 0.4 GeV. For tracks with a p_T of higher than 0.4 GeV, the track efficiencies for both negatively and positively curved tracks are very similar. This can be explained due to the radial slope for the CJC cells (see section 2.5.1 on page 28).

5.5 The FTT T0 Trigger Element

The main task of the L1 trigger is to select *ep* events that have a well determined time origin. As already notified in section 3.5.2 on page 46, the FTT t_0 trigger element is set if a t_0 validated event was found. In the t_0 algorithm used in this thesis, the t_0 event is defined on the basis that in such events, the number of found track segments corresponding to a single track is highest.

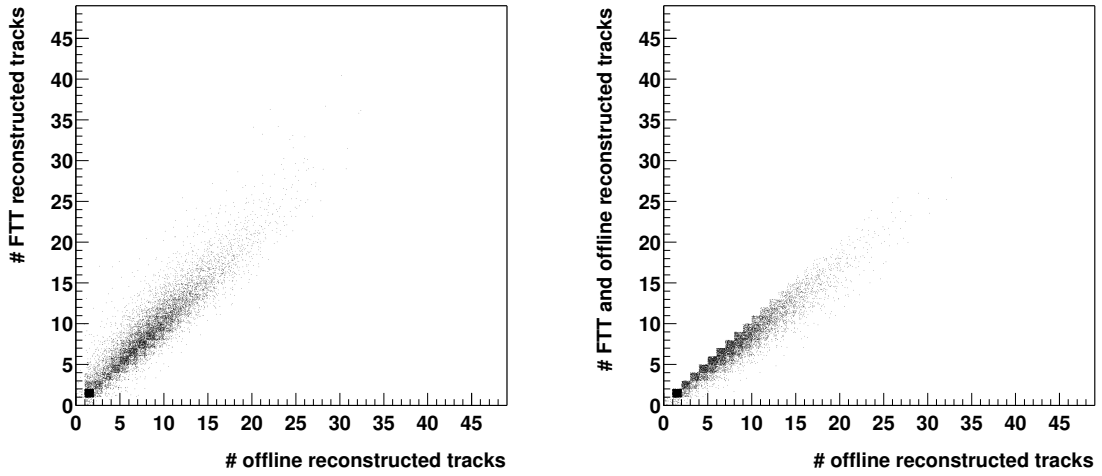

(a) *(b)*

Figure 5.12: (a) The number of FTT reconstructed tracks and (b) the number of offline tracks also found by the FTT, shown against the number of offline reconstructed tracks in the acceptance region of the FTT.

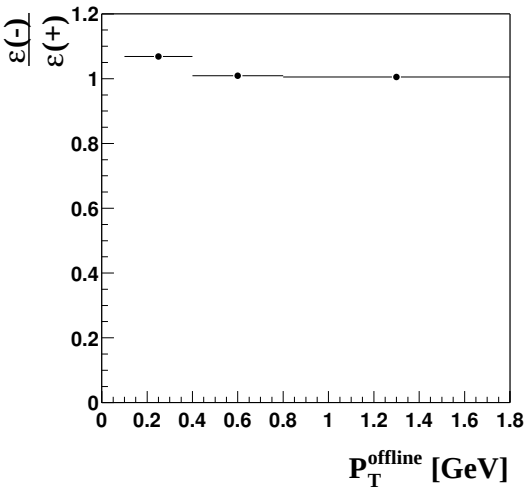

Figure 5.13: Ratio of tracks with negative and positive track curvature shown as a function of the offline reconstructed p_T.

Firstly, the timing of FTT t_0 validated events has been investigated. Figure 5.14 shows the timing for various processes. In all three cases, t_0 validated events are spread over several bunch crossings. In the case of the proton-dissociative ρ^0 MC sample shown in figure 5.14(a), approximately 87% of the events have been selected in the correct bunch crossing. For the selected NC data sample (see figure 5.14(b)), the number of events with a t_0 validated track in the correct bunch crossing rises to approximately 94%. For the selected CC data sample shown in figure 5.14(c), the number of t_0 validated events in the correct bunch crossing is 87% and is thus comparable to the result for the proton-dissociative ρ^0 MC sample. From the fact that the quality of the sum of all tracks found by the FTT has to be above a given threshold, high multiplicity events should have a higher t_0 probability than low multiplicity events. Thus, both NC and CC events should have approximately the same high overall t_0 efficiency. As both event classes generally include a jet, one explanation may be that the high p_T track of the scattered electron, which is always present in NC events, is responsible for the good t_0 performance in the case of NC events. Thus, if only a jet is present, the probability, that the quality of the summed tracks in the correct bunch crossing is better than the quality of the summed tracks in the bunch crossing after the correct one, is slightly smaller. This is probably due to the high track multiplicity which causes track segments to sometimes be linked to the wrong track. In order to find out the exact cause of this effect, the performance of the algorithm needs to be studied further. During the further optimisation of the algorithm, however, care has to be taken that the FTT t_0 trigger element selects the correct events with a high efficiency.

Secondly, the t_0 efficiency is investigated. For this study, the proton-dissociative ρ^0 MC sample was used. Care was taken that only events passing the L1 track criteria were used. Figure 5.15 shows the t_0 efficiency as a function of the p_T of the track. The t_0 efficiency behaves as expected. Knowing the L1 track efficiency as well as the t_0 timing efficiency, the trigger efficiency is expected to be approximately 82% for tracks below 0.4 GeV and 86% for tracks above that value. The ρ^0 Monte-Carlo (dots) confirms this statement.

5.6 Summary

In this chapter, the simulated performance of the FTT for various processes has been presented. The L1 track resolutions for the different $\frac{1}{p_T}$ bins were presented for a NC data sample. The resolutions were approximately equal to 1 GeV^{-1} except for the highest p_T bin where the resolution was reduced to 0.77 GeV^{-1}. The L1 ϕ resolutions were found to be comparable to the expectation of $RMS_\phi = 0.06$ rad. With $RMS_\phi = 0.05$ rad in the case of a J/ψ data sample, the resolution was slightly better than design. In the case of a NC data sample the resolution was found to be $RMS_\phi = 0.1$ rad and was slightly worse that expected. This was mainly due to the high multiplicity in the NC event.

The L2 resolutions were presented for the three track parameters θ, ϕ and $\frac{1}{P_T}$ in the case of a J/ψ data sample as well as the NC data sample. The J/ψ sample only includes tracks with a $p_T > 0.8$ GeV so that the resolutions are sightly better than for the NC events. It was shown that the FTT is very robust in reconstructing tracks. For high

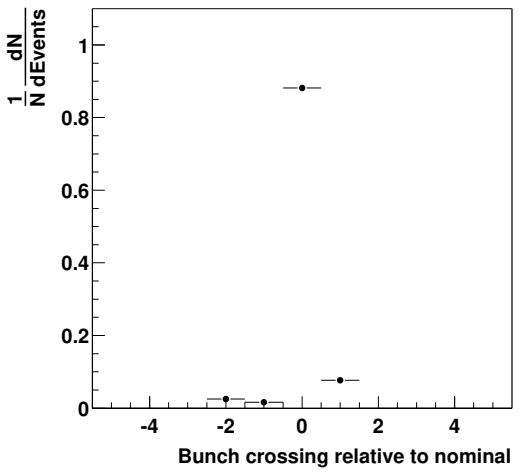

(a)

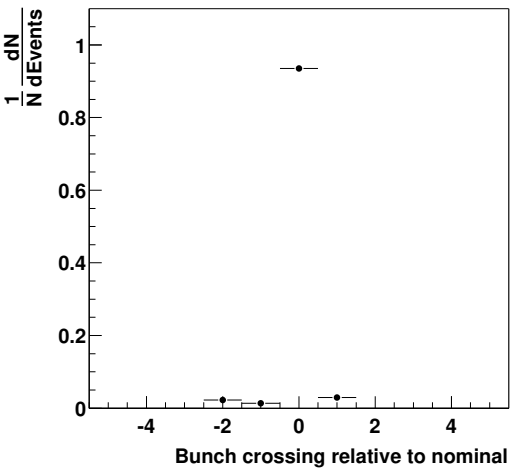

(b)

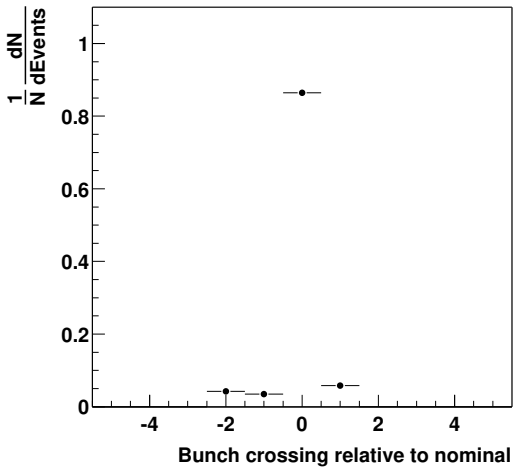

(c)

Figure 5.14: The number of events with a t_0 validated track is shown as a function of the Bunch Crossing relative to the nominal one in the cases of (a) the ρ^0 MC sample, (b) the selected NC data sample and (c) the selected CC data sample. If an event incorporates several tracks each of which is t_0 validated for a different bunch crossing, the event enters the bunch crossing bin where the first t_0 validated track was found.

multiplicity NC events, the L1 linker could determine the charge of tracks with a p_T of up to 5 GeV. In 95% of the cases, the FTT reconstructed tracks below 1 GeV have the correct track curvature. The overall L2 track efficiencies were found to be 95% in the case of the $\gamma^\star p \rightarrow \rho^0\ Y$ MC sample as well as for the NC data sample. In the NC sample, the track of the scattered electron is found with an efficiency of 99%. Due to the high multiplicity, low p_T tracks are reconstructed with lower efficiency than in the low multiplicity ρ^0 MC sample.

Finally, the performance of the currently implemented FTT t_0 algorithm was presented. Approximately 86% of the ρ^0 and CC events were assigned to the correct bunch crossing of origin. In the case of the NC data sample, this fraction increased to above 90%. The reason for the increase was related to the fact that the high p_T track of the scattered electron increased the overall quality of the event and likelihood to find a t_0 validated event. The efficiency of the t_0 trigger element was investigated using the proton-dissociative ρ^0 MC.

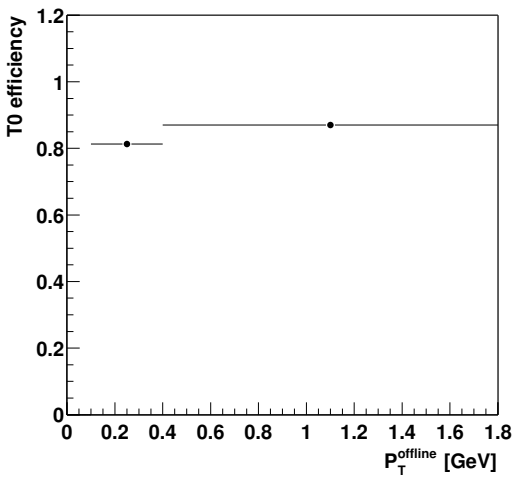

Figure 5.15: The efficiency to obtain a t_0 validation of an event in the nominal bunch crossing is shown against the track parameter p_T for the low multiplicity process $\gamma^\star p \rightarrow \rho^0\ Y$. The proton-dissociative ρ^0 MC was used.

It was found that the trigger efficiency rises from approximately 82% to approximately 87% for tracks with a p_T above 0.4 GeV. Further work is needed to optimise the t_0 trigger element in order to minimise the bias in the trigger decision.

Chapter 6

A Study to Trigger Low Multiplicity Processes with the FTT

6.1 Introduction

In the previous chapter, it was shown that the FTT is able to reconstruct three dimensional tracks reliably reliably at L2 using the three track parameters κ, Φ and θ. With this track information available, it is possible to reconstruct the invariant masses of resonances at the third level of the FTT. This feature provides the possibility to reconstruct invariant masses of vector mesons at the trigger level.

In this chapter, two trigger studies are presented. In the first study, the possibility to trigger on elastic photo-production events was investigated using a photo-produced J/ψ with the J/ψ decaying to $\mu^+\mu^-$ MC sample. In the second study, the possibility to trigger on the electro-produced ρ^0 with the ρ^0 decaying to $\pi^+\pi^-$ was investigated. The aim of this study was to investigate the feasibility to trigger on ρ vector mesons at high $|t|$.

6.2 Considerations for Developing a New Trigger

When developing a new trigger, three important issues have to be addressed:

- Due to the variety of interesting physics processes and the limited trigger rate that is available, only part of the overall trigger rate is available for a given physics process.
- To collect as much statistics as possible for each triggered process, it is important to have highly efficient triggers with low backgrounds.
- A good set of triggers should ideally select one physics process. This would simplify the analysis of a given channel significantly.

The aim of the following trigger studies is to validate an existing sub-trigger, which was designed to trigger on the considered process, with an FTT L2 or L3 condition. The goal is to reduce the current rate by a factor 5, but maintain the efficiency of the current sub-trigger.

6.3 Determination of the Trigger Efficiency and Evaluation of its Rate

Before the evaluation of the efficiency of a given trigger, the resolutions of the variables used to separate the background from the signal processes, need to be estimated. This is generally done using a Monte-Carlo model of the signal process. In this chapter, the FTT (offline) *RMS* value is presented as the FTT (offline) resolution σ.

After the selection of the variables to cut upon, the different cuts can be implemented and the trigger efficiencies can be evaluated. In the case where a Monte Carlo event sample is used, the trigger efficiency is usually evaluated according to the following equation:

$$\epsilon = \frac{N\ (offline, FTT\ cut\ passed)}{N\ (offline)}, \tag{6.1}$$

where N denotes the number of events fulfilling the conditions listed within the parentheses. In the instance where a selected data set is used however, the trigger efficiency is determined from the following equation:

$$\epsilon = \frac{N\ (MT, offline, FTT\ cut\ passed)}{N\ (MT, offline)}, \tag{6.2}$$

where N is the same as in equation 6.1 and MT is a monitor trigger which is independent of the FTT. This monitor trigger has to be used to avoid a bias of the trigger efficiency.

In order to predict the L3 rate of the newly developed trigger, a set of L2-L4 transparent runs from the years 1997 and 1999 were analysed. These contain all events that were selected at the first level with no further rejection taking place at the second or fourth level stages.

The trigger rates of the different levels are defined as follows:

- The L1 rate of a specific sub-trigger $R_{ST,L1}$ corresponds to the events per second that have been accepted through the logical combination of the trigger elements belonging to the sub-trigger ST.
- The L2 rate $R_{ST,L2}$ corresponds to the number of events per second that have been selected by the second level of a trigger sub-system. The validation step involves the combination of the L1 decision with the different L2 trigger elements through a logical "*AND*".
- The L3 rate $R_{ST,L3}$ corresponds to the rate at which a sub-trigger accepts events after the validation at the second and third trigger level.

The rate $R_{FTT,L3}$ is calculated as follows:

$$R_{FTT,L3} = R_{MT,L1} \cdot \frac{Number\ of\ events\ triggered\ by\ FTT\ after\ L3\ and\ MT\ at\ L1}{Number\ of\ events\ triggered\ by\ MT\ at\ L1}, \tag{6.3}$$

where the monitor trigger (MT) is a sub-trigger which should select all events that could be potentially triggered by the FTT.

6.4 Kinematic Reconstruction Methods

In order to get the best offline resolutions for the various kinematic variables, a variety of kinematic reconstruction methods are available. In the cases where the outgoing scattered electron is not detected or the outgoing lepton is a neutrino, the kinematic variables x, y and Q^2 can be derived from the hadronic final state [72]: the **Jacquet-Blondel** or **hadron method**. The inelasticity y and the virtuality Q^2 can then be re-written as:

$$y_h = \frac{\Sigma_h}{2 \cdot E_e}, \qquad Q^2_h = \frac{P^2_{T,h}}{1 - y_h}, \tag{6.4}$$

where the variables $P_{T,h}$ and Σ_h which are used to reconstruct the kinematic variables from the hadronic final state are defined below:

$$\begin{aligned} P_{T,h} &= \sqrt{\left(\sum_{all\ \ hadrons,i} (\vec{p_i})_x\right)^2 + \left(\sum_{all\ \ hadrons,i} (\vec{p_i})_y\right)^2}, \\ \Sigma_h &= \sum_{all\ \ hadrons,i} (E_i - (\vec{p_i})_z). \end{aligned} \tag{6.5}$$

The kinematic variable x follows from equation 1.7 such that

$$x_h = \frac{Q^2_h}{y_h \cdot s}. \tag{6.6}$$

This method is applied for reconstructing *charged current* events, where the scattered neutrino cannot be directly measured within the detector. In these cases, the transverse momentum $P_{T,h}$ has the same amplitude as the missing transverse momentum P_T^{miss}. This method is also used in this chapter in order to reconstruct the variable Q^2 in the case of the ρ^0 trigger study [65]. Another useful variable is the inclusive hadronic angle γ_h. It is defined by:

$$\tan\frac{\gamma_h}{2} = \frac{\Sigma_h}{P_{T,h}} \tag{6.7}$$

and is used in chapter 7 to limit the angular range of the hadronic final state that is considered in charged and neutral current processes. For the NC process, for example, where redundant information is available, the use of two alternative reconstruction methods is possible. In the **electron-method**, the kinematic variables are reconstructed from the polar angle θ_e and the energy E' of the scattered electron.

$$Q^2_e \equiv 4E_eE'_e\cos^2\left(\frac{\theta_e}{2}\right), \qquad y_e \equiv 1 - \frac{E'_e}{E_e}(1 - \cos\theta_e), \qquad x_e = \frac{Q^2_e}{y_e \cdot s}. \tag{6.8}$$

The other method for reconstructing the kinematic variables is the **double-angle method** [73]. Here, only the angles of the scattered electron and the hadronic final state are used:

$$y_{DA} = \frac{\sin\theta_e \cdot (1 - \cos\gamma_h)}{\sin\gamma_h + \sin(\theta_e + \gamma_h)}, \qquad Q^2_{DA} = \frac{4 \cdot \sin\gamma_h \cdot (1 + \cos\theta_e)}{\sin\gamma_h + \sin[\theta_e - \sin(\theta_e + \gamma_h)]}. \tag{6.9}$$

This method is used in the reconstruction of the centre of mass energy of the photon-proton system $W_{\gamma p}$ in the ρ^0 trigger study. It is given by:

$$W^2_{\gamma p} = Q^2_{DA}\left(1 - \frac{1}{x_{DA}}\right). \tag{6.10}$$

6.5 Reconstruction of the Invariant Mass and Mandelstam $|t|$

At L3, the invariant mass $M_{l,l}$ of the vector meson can be reconstructed as follows:

$$M_{l,l} \simeq \sqrt{2 \cdot E_{l^+} \cdot E_{l^-} - 2 \cdot \vec{p}_{l^+} \cdot \vec{p}_{l^-} + m^2_{l^+} + m^2_{l^-}}, \tag{6.11}$$

where E_{l^+} (E_{l^-}) is the energy, p_{l^+} (p_{l^-}) is the momentum and m_{l^+} (m_{l^-}) is the mass of the positive (negative) decay lepton respectively.

In photo-production, the electron is scattered at a very small angle and remains undetected in the beampipe. Hence, the Mandelstam variable t for the vector meson process is to a good approximation given by:

$$t \simeq -(\vec{p}_{T,l^+} + \vec{p}_{T,l^-})^2. \tag{6.12}$$

In electro-production, however, the electron transfers momentum to the produced vector meson and thus cannot be ignored in the calculation of the Mandelstam variable t:

$$t \simeq -(\vec{p}_{T,l^+} + \vec{p}_{T,l^-} + \vec{p}_{T,e})^2. \tag{6.13}$$

The Mandelstam variable t is always negative and describes the four-momentum transfer squared at the proton vertex.

6.6 Triggering J/ψ Events with the FTT

The aim of this study was to investigate the feasibility of triggering on diffractive J/ψ events in the photoproduction. In order to do this, the idea was to develop a trigger based on a FTT-L3 trigger element and sub-trigger ST15. The H1 collaboration would allow such a trigger to have a post-upgrade rate of 1 Hz [74] corresponding to a pre-upgrade rate of 0.2 Hz. The logical combination of ST15 is listed in table 6.1.

Sub-trigger	logical trigger element combination	$R_{ST,L1}$ [Hz]
ST15	(Mu_Bar $\vee$ Mu_ECQ) $\wedge$ DCRPh_THig $\wedge$ zvtx_sig> 0	2

Table 6.1: Monitor trigger used for calculating the L3 rate of the FTT. Here, $R_{ST,L1}$ is the unprescaled L1 rate of sub-trigger ST15 during the HERA I running period.

The different trigger elements used by sub-trigger ST15 are described in the following:

- **Mu_Bar**
  This trigger element requires that at least two of the four trigger layers in the central region of the central muon system find a charged particle.
- **Mu_ECQ**
  The trigger element is set once a particle is found by three out of the five trigger layers of the forward or backward end caps of the central muon system.
- **DCRPh_THig**
  This trigger element is set if the DCr$-\phi$ trigger finds at least one track with a p_T above 0.8 GeV.
- **zvtx_sig**
  The z-vertex trigger searches for track candidates originating from the interaction point ("rays"). If the ratio between the number of rays in a single bin of the z-vertex histogram (see section 2.5.2 page 29) to the total number of rays is above a given threshold, the zvtx_sig trigger element is set. A set of four thresholds, reaching from 0 to 3, is available. In this study, the lowest threshold (zvtx_sig> 0) is required.

The data sample used in this study consists of selected γp events which have decayed into a pair of muons with a mass of 158 ± 0.10 MeV [6] each. The event selection was constrained to events with only two tracks within a θ range $[20°, 160°]$. The transverse momentum of both tracks was required to be at least 0.8 GeV. Furthermore, the tracks were required to originate from the interaction region ($|z - vertex| < 40$ cm). At L1, the number of tracks reconstructed is shown in figure 6.1. The figure shows that more than one track is found and reconstructed at the first trigger level within the acceptance region of the FTT in approximately 93% of all cases. As the L1 rate can still be reduced after L2 and L3, a simple trigger element requiring one or more FTT reconstructed tracks at L1 with a transverse momentum above 0.1 GeV could be used in conjuction with the first level trigger conditions of ST15 to select J/ψ vector mesons.

At L2, the refined track information enables a more accurate determination of the track multiplicity in the acceptance region of the FTT. From figure 6.2 it can be seen that the number of events where only one track is reconstructed within the acceptance region of the FTT remains approximately the same, whereas the fraction of events with the correct track multiplicity increases to approximately 94%.

Figure 6.3 shows the reconstructed J/ψ invariant mass distribution with a clear peak for the offline reconstructed invariant mass as well as the reconstruction of the invariant

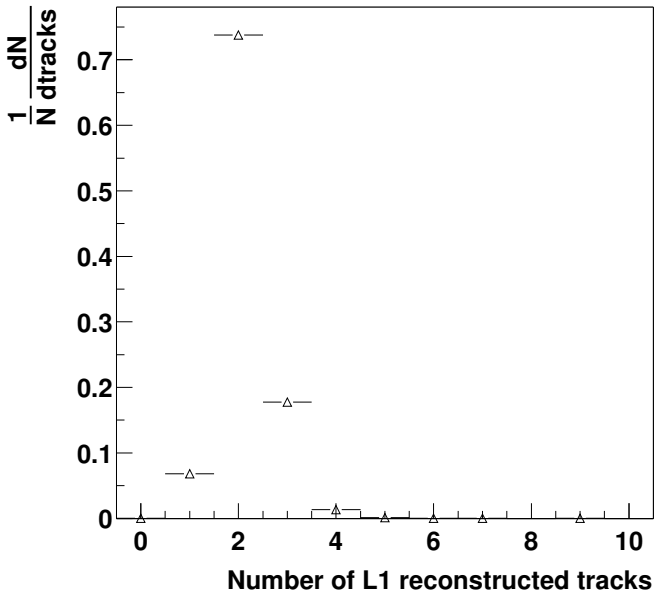

Figure 6.1: Number of tracks reconstructed by the FTT at L1 in $\gamma p \rightarrow J/\psi\, p$ events.

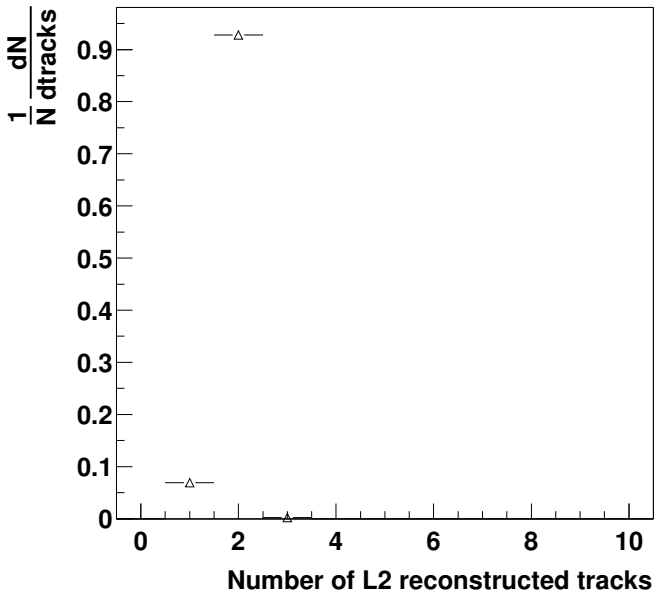

Figure 6.2: Number of tracks reconstructed by the FTT at L2 in $\gamma p \rightarrow J/\psi\, p$ events.

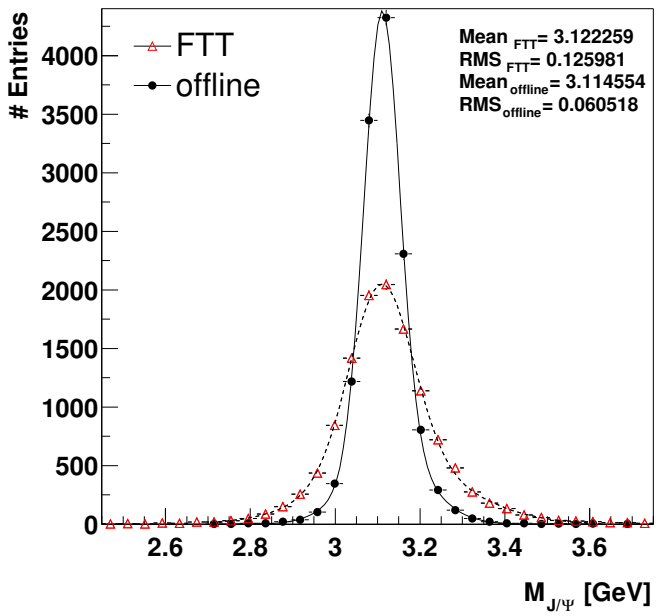

Figure 6.3: The invariant J/ψ mass reconstructed from the two muons at the FTT-L3 trigger level as well as offline.

mass at L3 of the FTT. In both cases, the mean value of the invariant mass is close to the nominal J/ψ mass of 3.097 GeV.

This is confirmed in figure 6.4, where the difference between the nominal J/ψ mass and the reconstructed invariant mass is shown for both the FTT reconstruction at L3 and the offline reconstruction.

The reconstruction of the variable t is shown in figure 6.5. In photo-production, the resolution of the FTT reconstructed Mandelstam $|t|$ ($\sigma_{FTT} = 0.049$) is only slightly worse than the offline resolution of $|t|$ ($\sigma_{\text{offline}} = 0.035$).

6.6.1 The Final Trigger Algorithm

The trigger algorithm that was preferred is the following [75]:

- the two track candidates must have opposite curvature κ,
- the transverse momentum of all tracks should be above a given $P_{T,cut}$ threshold,
- the reconstructed invariant mass of the two track candidates $M_{track\ comb}$ must be within an interval $\Delta M = |M_{J/\psi} - M_{track\ comb}|$, where $M_{J/\Psi}$ is the nominal J/ψ mass,
- the Mandelstam variable $|t|$ is larger than the value $|t|_{cut}$.

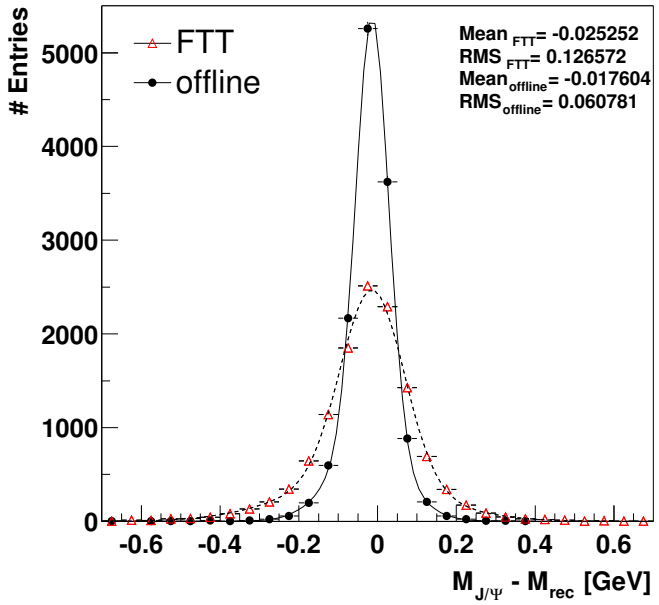

Figure 6.4: The difference between the generated and reconstructed J/ψ mass is shown. The dots represent the offline reconstructed mass difference and the triangles represent the FTT reconstructed mass difference.

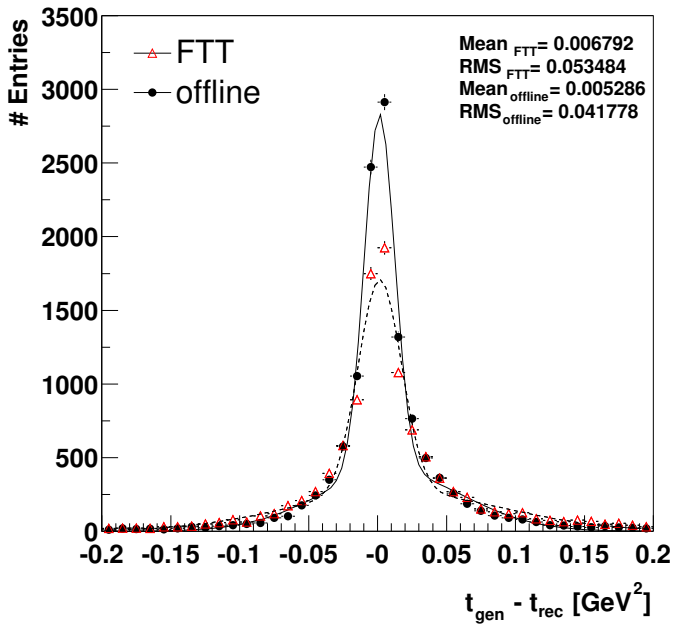

Figure 6.5: The reconstructed Mandelstam variable t is compared to the generated one in both the FTT reconstruction (triangles) and the offline reconstruction (dots). The FTT resolution σ_{FTT} was to be 0.03 GeV in the case of elastic $J/\psi \rightarrow \mu^-\mu^+$ using the photo-production MC.

Other resonance production processes take place which also yield a pair of muons take place in approximately the same mass range. These are:

$$\Psi(2S) \rightarrow \mu^+\mu^-; \tag{6.14}$$
$$\Psi(2S) \rightarrow J/\psi\ \pi^+\pi^- \rightarrow (\mu^-\mu^+)\ (\pi^+\pi^-). \tag{6.15}$$

In order to allow for these background processes to be accurately fitted in the analysis, the analysis cut $\Delta M < 1.1$ GeV is applied in [64]. To take into account that the FTT mass resolution is slightly worse than the resolution offline, an FTT cut of $\Delta M < 1.2$ GeV is necessary.

6.6.2 Trigger Efficiency

The trigger efficiency of the algorithm was determined from the J/ψ diffractive MC described in section 5.2.1 on page 68. The FTT and offline cuts that were used are listed in the table below:

Parameter	Analysis cut	FTT-selection cut
$p_{T,cut}$	0.8 GeV	0.7 GeV
ΔM	1.1 GeV	1.2 GeV
$n_{tracks,max}$	2	2

Table 6.2: Cuts performed in order to predict the efficiency of the J/ψ trigger algorithm.

Using the above described algorithm, the efficiency to trigger elastic J/ψ photo-production events can be seen in figure 6.6. If no cut on the FTT measured Mandelstam $|t|$ is applied, J/ψ vector mesons are triggered with an efficiency of 94%.

As shown in figure 6.7, a cut accepting events with $|t|$ above 0.1 GeV^2 as reconstructed by the FTT would only affect the trigger efficiency at low values of $|t|$. At a value of $-t_{offline} = 0.2$ GeV^2, the trigger efficiency reaches the value of 94% determined previously.

6.6.3 Trigger Rates

The trigger rate has been determined from equation 6.3. The monitor trigger used to determine the rate is sub-trigger ST15. Its characteristics are listed in table 6.1 page 91. Figure 6.8 shows the trigger rate as a function of the transverse momentum of the tracks as measured by the FTT. Despite the requirement $p_T > 0.8$ GeV in the ST15 monitor trigger, a small dependence of the rate on p_T is observed for $p_T < 0.8$ GeV. Hence, J/ψ candidates are selected by ST15 that include at least one track with a transverse momentum below $p_T \simeq 0.7$ GeV according to the FTT reconstruction.

As shown in figure 6.9, the trigger rate evolves roughly linearly with the cut on the width of the mass difference ΔM as measured by the FTT. With a value of $\Delta M = 0.4$ GeV,

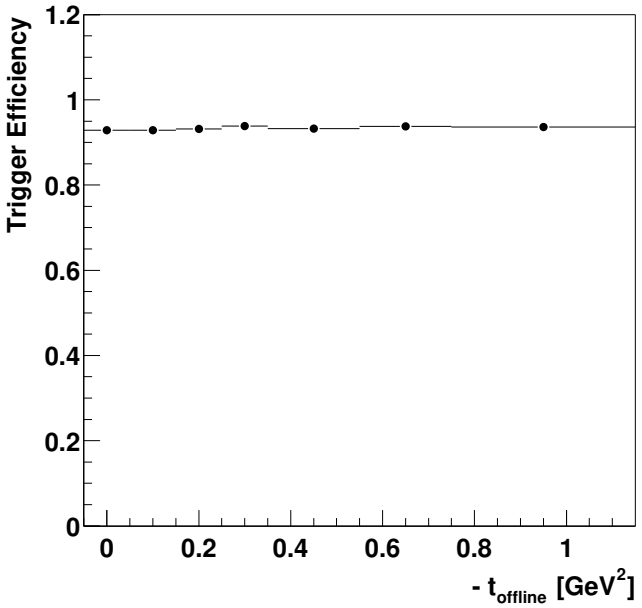

Figure 6.6: The trigger efficiency of the algorithm searching for elastic J/ψ events in photo-production as a function of the Mandelstam variable $-t_{offline}$.

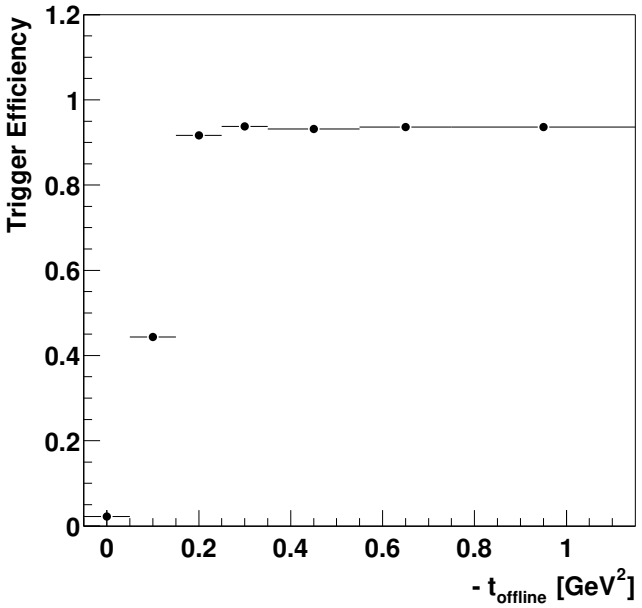

Figure 6.7: The trigger efficiency of the algorithm searching for elastic J/ψ events in photo-production as a function of Mandelstam $|t|$ as measured offline if the cut $-t_{FTT} > 0.1$ is applied on trigger level.

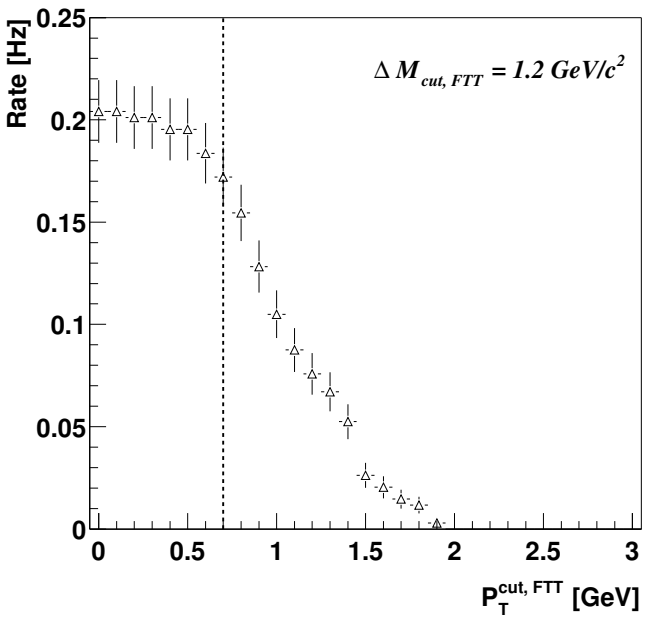

Figure 6.8: L3 Rate of FTT validated sub-trigger ST15 as a function of $p_{T,\ FTT}^{cut}$.

only the J/ψ signal region will be selected. In that case the rate is approximately equal to 0.07 Hz. However, the disadvantage of such a selection is that it would be impossible to estimate the background accurately due to the lack of a control sample in the sidebands away from the resonance. Hence, it seems to be reasonable to cut on a value of $\Delta M <$ 1.2 GeV as measured by the FTT. This is also compatible with the current offline J/ψ analyses, where the cut $\Delta M = 1.1$ GeV is applied.

In figure 6.10, the $\gamma p \to J/\psi\, p$ rate is plotted as a function of the variable $-t_{cut,FTT}$. It can be seen that the rate drops drastically as the value of $-t_{cut,FTT}$ increases from 0.1 to 0.2 GeV^2. Hence, one possibility to reduce the rate further would be to apply a cut on $|t|$. This may be acceptable since the low $|t|$ region is already well measured. As the trigger efficiency of sub-trigger ST15 was 21.4% during the HERA I running period, loosening the requirements is desirable. It may be possible to remove the muon conditions of ST15 and thus raise its trigger efficiency to 70.8%. This would be a significant improvement of the elastic J/ψ triggers.

6.6.4 Conclusion

In this section it was shown that it is possible to trigger on $\gamma p \to J/\psi\, p$ events with a HERA II trigger rate of less than 1 Hz by validating sub-trigger ST15 with the algorithm described above running at the FTT-L3. During the HERA I running period, the efficiency of ST15 to trigger on elastic J/ψ events was 21.4%. In order to increase its efficiency to 70.8%, the muon trigger elements would have to be removed. This would mean that other background channels producing $\pi^+\pi^-$ pairs would need to be considered. Assuming that

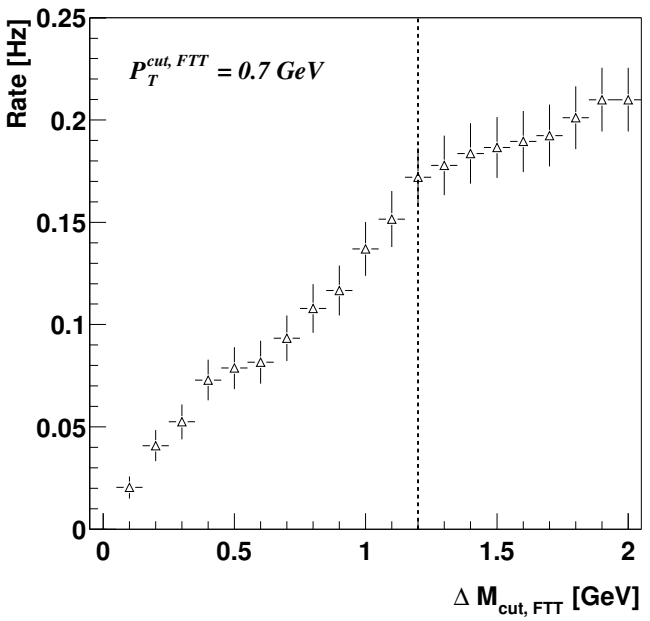

Figure 6.9: L3 Rate of FTT validated sub-trigger ST15 as a function of $\Delta M_{cut,\ FTT}$.

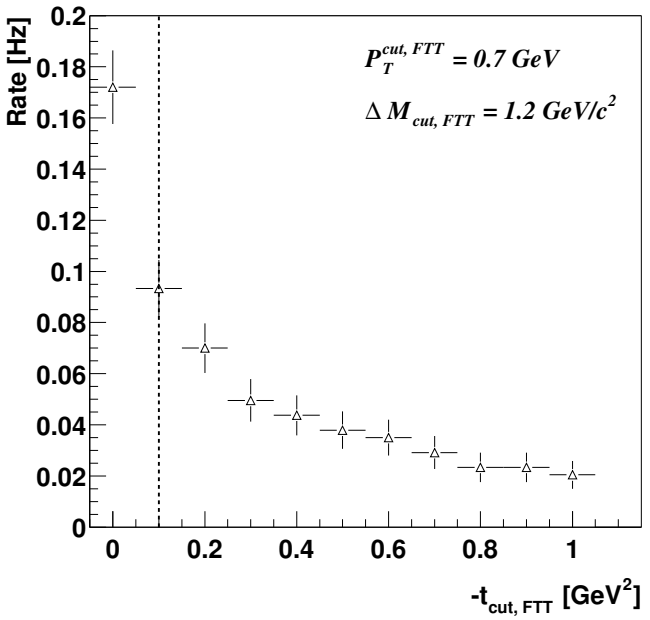

Figure 6.10: L3 Rate of FTT validated sub-trigger ST15 as a function of $t_{cut,\ FTT}$.

these additional background processes only raise the rate by a factor 2, the removal of the muon trigger elements may be compensated with a cut on $|t_{FTT}| > 0.1$ GeV^2 which would entail a loss in trigger efficiency of 100% for J/ψ events where the four-momentum transfer at the proton vertex $|t_{offline}|$ is equal to zero.

6.7 Triggering ρ^0 Mesons in Electro-production

The aim of this study was to investigate the the possibility of triggering on ρ^0 mesons in electro-production. Exploiting the possibility to calculate invariant masses at L3, the idea was to develop an algorithm to trigger on ρ^0 mesons with the FTT especially at large $|t|$. This trigger should be based on the FTT and the SpaCal sub-trigger ST0. The H1 collaboration would allow such a trigger to have a post-upgrade rate of 1 Hz [74], corresponding to a pre-upgrade rate of 0.2 Hz. The sub-trigger ST0 is composed of the trigger element listed in table 6.3. This trigger element is used to trigger if the interacting electron scatters into the SpaCal:

- **SPCLe_IET**
  This trigger element requires that the energy E_C of at least one cluster in the electromagnetic section of the SpaCal is above threshold. The SPCLe_IET has a set of three thresholds: $E_C > 0.5$ GeV (low), $E_C > 2$ GeV (medium) and $E_C > 6$ GeV (high). The central clusters of the SpaCal are ignored by this trigger element.

For this study, a Monte-Carlo sample of proton dissociative ρ^0 events was used. Only two tracks within the θ interval $[20°, 160°]$ were allowed for this analysis. The selection was further constrained to the kinematic region defined by 5 GeV$^2 \leq Q^2 \leq 60$ GeV^2 and 40 GeV$^2 < W < 180$ GeV^2.

Sub-trigger	logical trigger element combination	$R_{ST,L1}$ [Hz]
ST0	SPCLe_IET> 2	5

Table 6.3: Monitor trigger used for calculating the L3 rate of the FTT. Here, $R_{ST,L1}$ is the unprescaled L1 rate of sub-trigger ST0 during the HERA I running period.

The number of tracks reconstructed at the first level of the FTT for the pre-selected ρ^0 meson electro-production sample is shown in figure 6.11. Only 70 % of the events are reconstructed with the correct track multiplicity. To make sure that no events are lost, an FTT trigger element that requires at least one track in the CJC with a transverse momentum of 0.1 GeV can be used in conjunction with the L1 conditions of sub-trigger ST0.

Figure 6.12 shows the track multiplicity from the process $\gamma^\star p \to \rho^0 Y$ as reconstructed at the second level of the FTT. It can be seen that the number of events with the correct track multiplicity increases slightly to approximately 87 %.

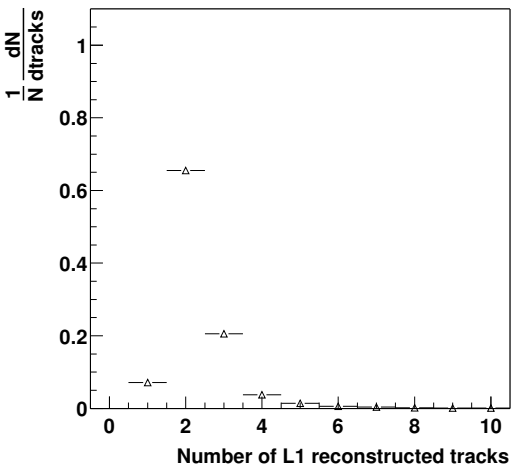

Figure 6.11: Proton-dissociative $\rho^0 \rightarrow \pi^+\pi^-$ tracks reconstructed by the FTT at L1.

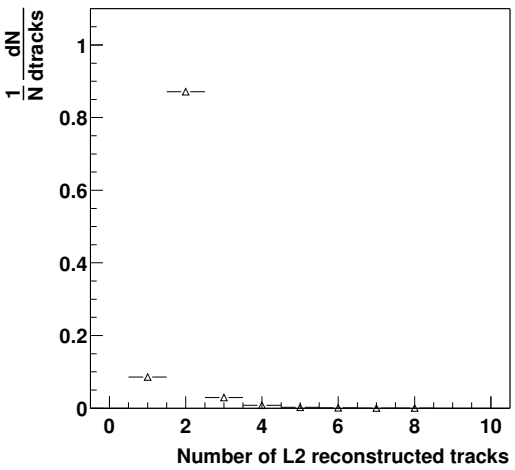

Figure 6.12: The number of $\rho \rightarrow \pi^+\pi^-$ tracks reconstructed by the FTT at L2. The ρ^0 Monte-Carlo selection was used for this study.

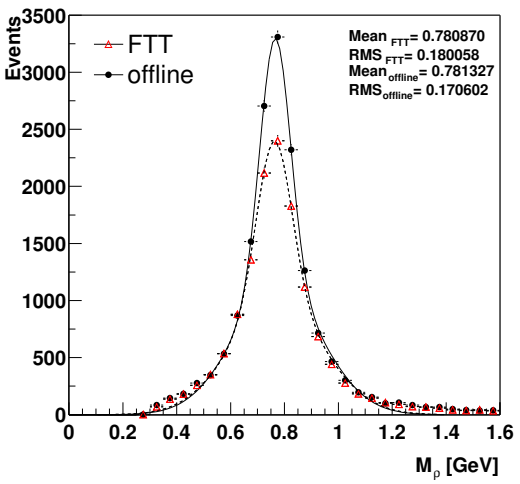

Figure 6.13: The FTT reconstructed invariant mass of the ρ^0 meson in electro-production. The elastic electro-production MC was used.

6.7.1 Reconstruction of the Invariant Mass

First, the reconstruction of the invariant mass was investigated using the sample described above. Figure 6.13 shows the reconstructed ρ^0 mass peak for both offline and trigger level reconstruction. In both cases, the mean of the invariant mass distributions is slightly higher than 768.5 MeV which is the mass of the nominal ρ^0 meson [6].

6.7.2 Reconstruction of Mandelstam $|t|$

In order to evaluate the Mandelstam variable t in electro-production at the trigger level, the transverse momentum of the electron has to be reconstructed. The only electron information available at L3 is the information from the electromagnetic clusters in the Spacal. Since the vertex position and the cluster energy are not known, the resolution on $|t|$ is significantly worse than that achieved offline. Assuming that the electron was scattered at the nominal vertex, the polar angle $\theta_{e'}$ of the scattered electron can be calculated using the following equation:

$$\begin{aligned} \theta_{e'} &= \pi - arctan(\frac{r_{e'}}{z_{e'}}), \\ r_{e'}^2 &= x_{e'}^2 + y_{e'}^2, \end{aligned}$$

where $x_{e'}$, $y_{e'}$ and $z_{e'}$ are the coordinates of the Spacal cluster hit by the scattered electron and $r_{e'}$ is the radius at which the hit occurred (see figure 6.14).

One way to reconstruct the transverse momentum of the scattered electron uses the fact that the difference between the energy E and the z-component of the momentum P for all particles in the initial state i has to be equal to the same difference of all particles

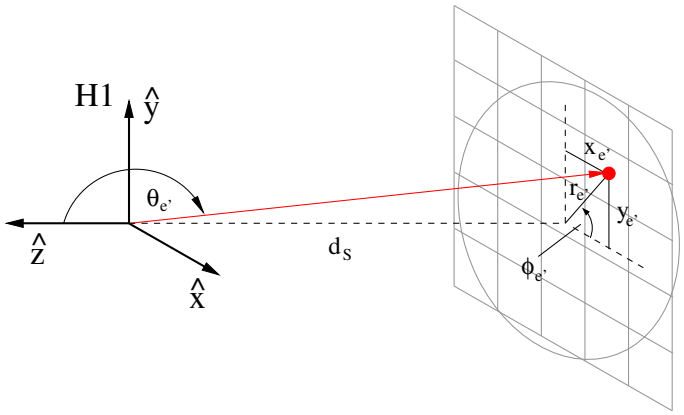

Figure 6.14: The electron track is reconstructed using the position of the hit cluster in the Spacal. The track is assumed to originate from the nominal vertex position in the H1 coordinate system.

present in the final state f [76]:

$$2E_e = \sum_i (E_i - P_{z,i}) = \sum_f (E_f - P_{z,f}),$$

where E_e is the energy of the electron. Then the energy of the scattered electron is given by:

$$E_{e'} \simeq \frac{(2E_e - (E_{\pi^+} - P_{z,\pi^+}) - (E_{\pi^-} - P_{z,\pi^-}))}{1 - cos(\theta_{e'})}, \tag{6.16}$$

where the particles observed in the tracker are assumed to be charged π mesons. Knowing the coordinates of the hits in the electromagnetic section of the SpaCal as well as the energy of the incoming electron, equation 6.16 can be used to calculate the energy $E_{e'}$ of the scattered electron at the third level of the FTT. The transverse momentum $p_{T,e'}$ of the scattered electron then follows from:

$$p_{T,e'} \simeq E_{e'} \cdot \sin(\theta_{e'}). \tag{6.17}$$

This method was used in [75] to reconstruct $p_{T,e'}$. For the selected Monte-Carlo sample of electro-produced ρ^0 mesons, the resulting resolution of the Mandelstam variable t from this method via equation 6.13 is shown in figure 6.15(a). Here the resolution from the FTT is much worse than the offline resolution. The FTT reconstructed Mandelstam variable t is under-estimated on average as the mean is positive.

Another way of estimating the transverse momentum of the scattered electron is to make use of the fact that the event should have overall zero transverse momentum. Hence, in the case of elastic ρ^0 production, the following equation is valid:

$$|p_{T,\rho^0}| = |p_{T,e'}|. \tag{6.18}$$

When, as in our sample, the ρ^0 particle decays into two pions, the absolute value of the

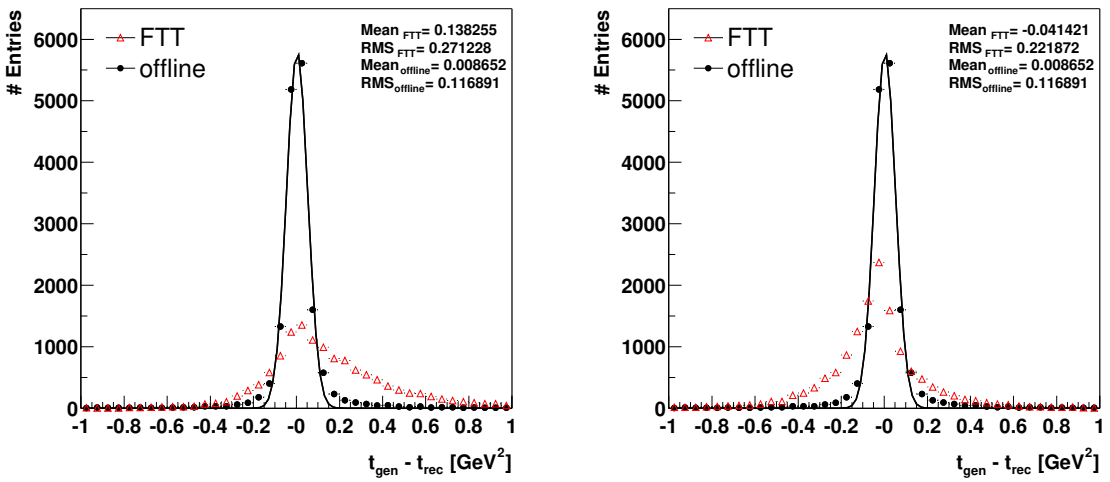

(a) *(b)*

Figure 6.15: The resolution on the reconstructed Mandelstam variable t was investigated using the elastic ρ^0 Monte-Carlo in electro-production. The variable t is compared to the generated one in both the FTT reconstruction (triangles) and the offline reconstruction (dots). In figure (a) t was reconstructed using equation 6.17 to reconstruct the electron's transverse momentum. In figure (b), t was reconstructed using the fact that the event has to be balanced in p_T. The second method results in a better resolution.

transverse momentum of the ρ^0 particle can be reconstructed as

$$|P_{T,e'}| = \sqrt{(\sum_i P_{x,i})^2 + (\sum_i P_{y,i})^2}, \tag{6.19}$$

where i stands for the π^+ and π^- particles. Using the ϕ information from the scattered electron (see figure 6.14), the x and y components of its momentum can then be extracted:

$$\begin{aligned} P_{x,e'} &= |P_{T,e'}| \cdot cos(\phi_{e'}), \\ P_{y,e'} &= |P_{T,e'}| \cdot sin(\phi_{e'}). \end{aligned}$$

Again, the elastic ρ^0 electro-production Monte-Carlo data sample was used. Figure 6.15(b) shows the difference between the reconstructed Mandelstam variable t and the generated one for both the FTT reconstruction and the offline reconstruction. This time, the method relying on the p_T balance is used for the reconstruction of the electron momentum at the trigger level. By using the second method, a much better resolution can be achieved at the trigger level than by using the first one. The second method allows harsher cuts at the trigger level without cutting into the signal. As a consequence, less background is accepted by the trigger.

Looking at proton-dissociative ρ^0 production, both reconstruction methods show a similarly bad reconstruction of the variable t at the trigger level (see figure 6.16). The resolution is worse for the proton-dissociative ρ^0 meson sample because particles from the proton-dissociative system are not taken into account in both methods. Furthermore, $|t|$

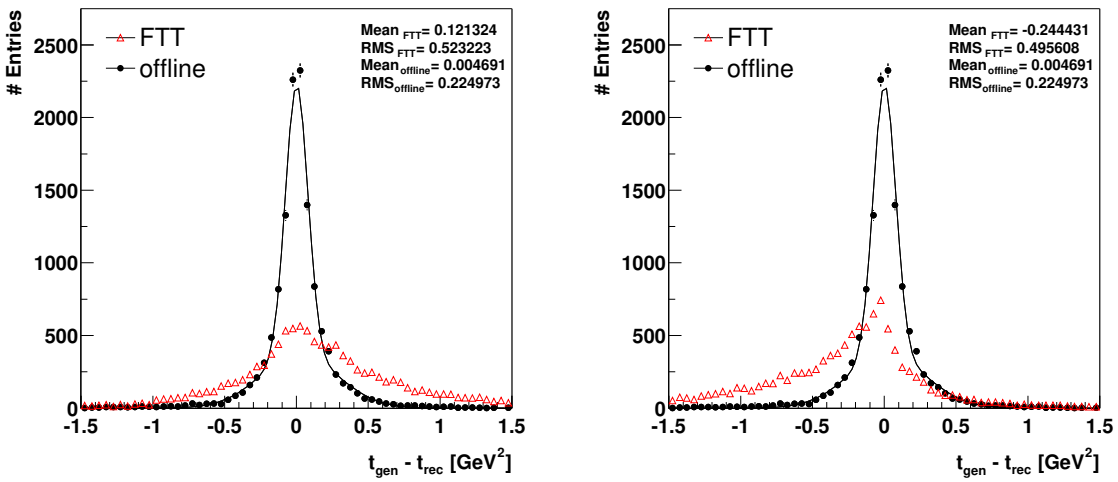

(a) *(b)*

Figure 6.16: The resolution on the reconstructed Mandelstam variable t was investigated using the proton-dissociative ρ^0 Monte-Carlo in electro-production. The variable t is compared to the generated one in both the FTT reconstruction (triangles) and the offline reconstruction (dots). In figure (a) t was reconstructed using equation 6.17 to reconstruct the electron's transverse momentum. In figure (b), t was reconstructed using the fact that the event has to be balanced in p_T.

is on average bigger in proton-dissociative samples. Hence, the approximation in equation 6.18 gets worse. Thus, it has to be concluded that t is not a good variable to cut upon at the trigger level. The next task was to set up a trigger algorithm that can be used to perform this task.

6.7.3 Trigger Efficiency

The trigger efficiency for various approaches are presented in this section. In all cases, a minimum of two track candidates reconstructed by the FTT at the second level is required. The kinematical cuts, listed in table 6.4, were applied when determining the ρ^0 trigger efficiency.

In figure 6.17, the trigger efficiency is shown as a function of $-t_{offline}$. Here, the search algorithm required that two tracks only are found and reconstructed by the FTT at the second level and a cut $\Delta M_{cut,FTT} = 0.8$ GeV was applied. The figure shows that the trigger efficiency remains high at approximately 85% at values of $|t_{offline}|$ up to 4 GeV^2. For $|t_{offline}| > 4$ GeV^2, the trigger efficiency drops down to 72%.

Figure 6.18 shows the trigger efficiency when either two or three tracks are found and reconstructed by the FTT at the second level. It can be seen that the trigger efficiency improves over the whole range in $|t|$. This improvement is most significant for proton-dissociative ρ^0 events where the variable $|t|$ as measured offline is in the range

Parameter	Analysis cut	FTT-selection cut
$p_{T,cut}$	0.1 GeV	0.1 GeV
ΔM_{cut}	none	0.8 GeV
W_{cut}	$40 < W < 180$	none
Q^2_{cut}	$5 < Q^2 < 60$	none
$n_{tracks,max}$	2	2
$n_{cluster}$	1	1

Table 6.4: Cuts performed in order to predict the efficiency and rate of the ρ^0 trigger algorithm.

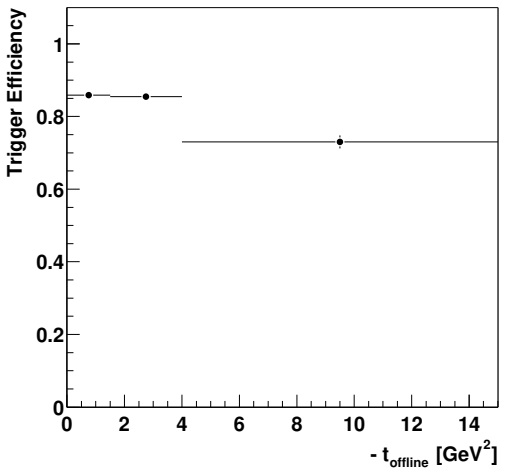

Figure 6.17: Trigger efficiency of the algorithm searching for proton dissociative ρ^0 vector mesons as a function of $-t_{offline}$. The algorithm required exactly two tracks to perform the search.

[4 GeV^2, 15 GeV^2].

An investigation of the trigger rate showed that the rate could only be reduced by 65% relative to the pre-upgrade conditions, which was not enough. If a minimum of two and a maximum of three tracks are required, the required rate reduction factor of 5 can only be reached if the cut $-t_{FTT} > 0.2$ GeV^2 is applied. This is undesirable for the proton-dissociative sample due to the poor $|t|$ resolution (c.f. figure 6.16). The resulting trigger efficiency is shown as a function of $-t_{offline}$ in figure 6.19. The trigger efficiency slowly rises from 40% at $|t_{offline}| = 0$ GeV^2 to 80% at $|t_{offline}| = 4$ GeV^2. For values of $|t_{offline}|$ in the range [4 GeV^2, 15 GeV^2], the trigger efficiency is 65%. Since the efficiency for exactly two tracks is better than this, it is not worth extending the FTT algorithm to allow three tracks.

Knowing that the trigger efficiency of ST0 is 75%, the trigger efficiency of the sub-trigger with the additional FTT requirements and exactly two FTT tracks is approximately 52% for ρ^0 events with $4 < |t_{offline}| < 15$ GeV^2. As sub-trigger ST0 used to be prescaled

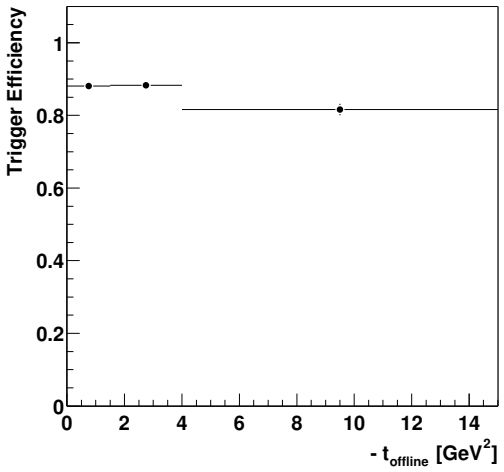

Figure 6.18: Trigger efficiency of the algorithm searching for proton dissociative ρ^0 vector mesons as a function of $-t_{offline}$. The algorithm required a minimum of two and a maximum of three tracks to perform the search.

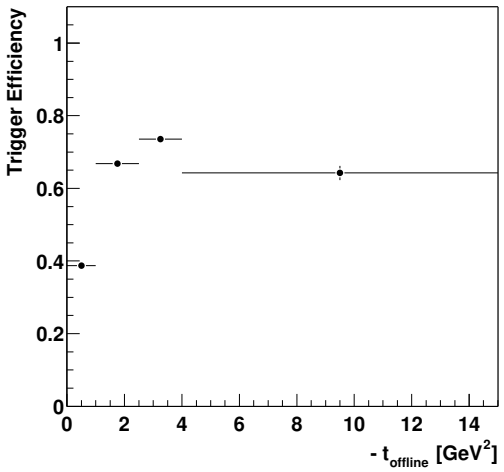

Figure 6.19: Trigger efficiency of the FTT validated ST0 as a function of $|t_{offline}|$. The algorithm required a minimum of two and a maximum of three tracks to perform the search. A further cut $|t| > 0.2$ GeV^2 was applied in the FTT reconstruction.

by a factor 3 approximately, its effective ρ^0 trigger efficiency during the HERA I running period was approximately 25%. This means that with the new FTT algorithm, the trigger efficiency is expected to improve by a factor 2. The rate for this new trigger algorithm is acceptable as is shown in the following section (section 6.7.4).

6.7.4 The Trigger Rates

The L3 rate at which an FTT validated sub-trigger ST0 would have triggered before the HERA luminosity upgrade has been determined from equation 6.3. Using an L2-L4 transparent run from 1997, all rates were investigated by applying only the FTT selection cuts listed in table 6.4. The results are shown in figure 6.20. The vertical dotted line in figure 6.20 marks the rate achieved if the following cuts are applied: $-t_{cut,\ FTT} = 0$, $\Delta M_{cut,\ FTT} = 0.8$ GeV and $p_{T,\ FTT}^{cut} = 0.1$.

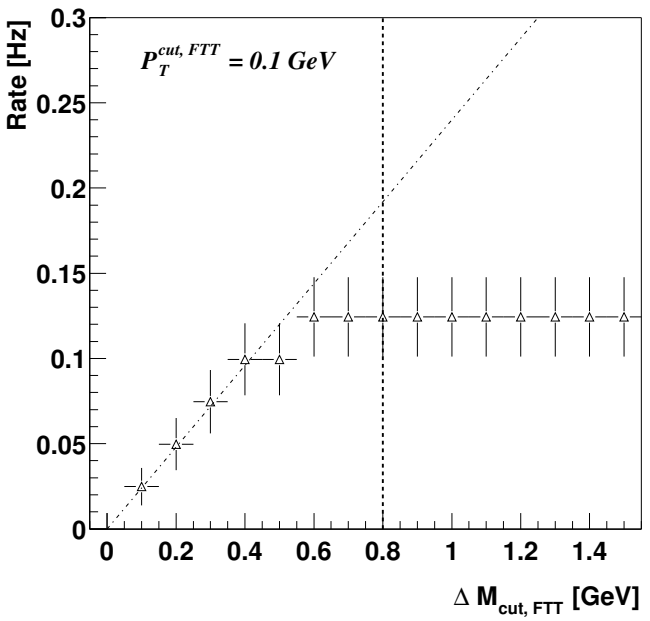

Figure 6.20: L3 Rate of FTT validated Sub-trigger ST0 as a function of $\Delta M_{cut,\ FTT}$. Exactly two FTT reconstructed tracks were required by the trigger algorithm.

Figure 6.20 shows the trigger rate as a function of the cut on the FTT reconstructed invariant mass ΔM_{FTT}. It can be seen that unlike the J/ψ trigger rate, the rate only evolves linearly at low values of $\Delta M_{cut,\ FTT}$. As the ρ^0 peak is wider than the J/ψ peak, the invariant mass is expected to increase linearly. It was found, that this is because there were no events of the L2-L4 transparent run with $\Delta M_{FTT} > 0.6$ GeV. With a cut $\Delta M_{FTT} = 0.6$ GeV most of the ρ^0 signal region is covered. Assuming that the trigger rate rises linearly, the rate was extrapolated to various $\Delta M_{cut,\ FTT}$ values. The maximum allowed rate for this trigger was reached at a cut value $\Delta M_{cut,\ FTT} = 0.8$ GeV. With this cut, the background can be estimated accurately due to the extension of the sidebands.

6.7.5 Conclusion

It has been shown that $\gamma^{\star}p \rightarrow \rho^0\, Y$ events can be triggered during the HERA II running period. The proposed trigger is based on the existing L1 sub-trigger ST0. The validation of the sub-trigger is performed at L3, where an algorithm requiring two FTT selected tracks with opposite curvature as well as a single electromagnetic cluster in the SpaCal, is run. The resulting trigger efficiency is 85% at values $|t_{offline}| < 4$ GeV^2 and 70% for events with Mandelstam $|t|$ in the range [4 GeV^2, 15 GeV^2]. The post-upgrade rate is less than 1 Hz.

6.8 Summary

In this chapter, the trigger efficiency as well as the rate of an FTT validated elastic J/ψ and proton-dissociative ρ^0 trigger were presented. In the photo-production regime, the $J/\psi \rightarrow \mu^+\mu^-$ channel was investigated. From the diffractive MC of elastic J/ψ vector meson production, the trigger efficiency of the FTT trigger element at L3 was determined to be approximately 94%. The rate at which events are accepted by the FTT validated sub-trigger ST15 previous to the HERA luminosity upgrade is always below 0.2 Hz. The FTT is likely to be able to maintain the existing J/ψ diffractive γp trigger rate. If the additional cut $|t|_{FTT} > 0.1$ GeV is applied at L3, the trigger efficiency of the FTT TE sharply rises from 0% to 94% as $|t|_{offline}$ rises from 0 to 0.2 GeV^2. If this cut is applied, the pre-upgrade trigger rate is approximately 0.1 Hz. With the low trigger efficiency of the present sub-trigger ST15 of approximately 21%, it may be possible to improve the trigger efficiency of the present sub-trigger to 70% by removing the muon trigger conditions. In order to ensure that the rate does not increase above 0.2 Hz, further studies considering background processes which produce $\pi^+\pi^-$ final states are needed. In electro-production, a diffractive high $|t|$ ρ^0 Monte-Carlo sample was used to investigate the trigger efficiency. The trigger efficiency of the FTT proton-dissociative ρ^0 trigger element was determined to be approximately 85% for events with an offline measured Mandelstam $|t|$ below 4 GeV^2. Above this value, the trigger efficiency drops down to 72%. The rate at which the FTT validated sub-trigger ST0 would have accepted events previous to the HERA luminosity upgrade was also found to be below 0.2 Hz. As the present sub-trigger ST0 has a trigger efficiency of 75%, the trigger efficiency of the FTT validated sub-trigger is 52% in the range [4 GeV^2,15 GeV^2]. If the rate of both triggers is proportional to the increase of the luminosity after the upgrade, the rate is predicted to stay below 1 Hz for each of the FTT validated sub-triggers, ST15 as well as ST0.

Chapter 7

The Design of a New Charged Current Trigger for the H1 Experiment

7.1 Introduction

Unlike neutral current (NC) events where the transverse momenta of the hadronic final state particles are balanced by the transverse momentum of the scattered electron, the hadrons in charged current (CC) events are balanced by an undetected neutrino. This means that a large missing transverse momentum is seen for charged current events.

In this chapter, the main CC triggers that were used before the upgrade are presented. After the accelerator upgrade, the design luminosity is expected to increase by a factor 5. The present CC triggers which were not prescaled during the HERA I running period, would therefore need to be prescaled. However, the modifications of the detector mean that one of the main CC triggers used before the upgrade is no longer available. The aim of this trigger was to improve the efficiency to trigger CC events with a low transverse momentum hadronic final state. In order to maintain the improvement in trigger efficiency in this low p_T region, the trigger had to be redesigned. This chapter investigates the possibility of using the FTT in this redesign.

7.2 The Charged Current Sub-Triggers

During HERA I, charged current events were mainly triggered by three sub-triggers, all of which relied in some way on the detected imbalance in p_T in the detector.

The logical combinations of trigger elements of these sub-triggers are shown in table 7.1. The different trigger elements are described in the following subsections.

ST66	$LAr_Etmiss > 2 \wedge LAr_IF > 1 \wedge (Ray_T0 \vee LAr_T0)$
ST77	$LAr_Etmiss > 1 \wedge Ray_T0$
ST71	$zvtx_sig > 1 \wedge DCr\phi_Tc \wedge LAr_BigRay$ $DCr\phi_T0 \wedge Ray_T0 \wedge L2(Big_T_miss)$

Table 7.1: The main CC sub-triggers at HERA I.

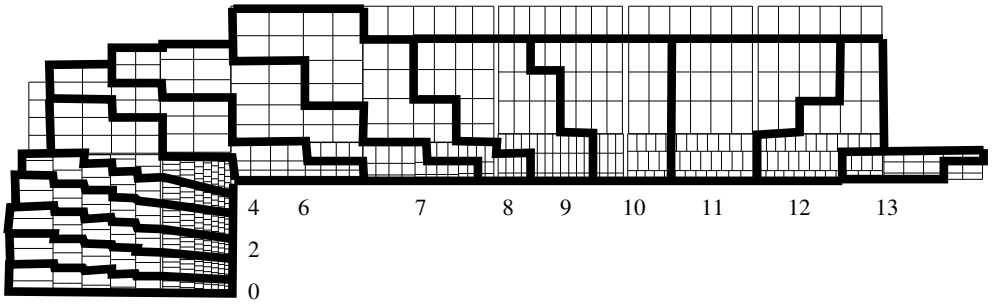

Figure 7.1: Side view of the LAr calorimeter in the $y - z$ plane. Only the upper part of the LAr calorimeter is shown as it is symmetric about the z-axis. The thick lines show the borders of the different big towers

7.2.1 Trigger Elements used to Trigger CC Events at HERA I

Liquid Argon Trigger Elements

The deposited energy inside each cell in the LAr calorimeter generates an analogue signal that can be read out. The signals of 16 (4) neighbouring cells of the electromagnetic (hadronic) calorimeter are combined into trigger cells (TC). These TCs are summed to form trigger towers (TT). The TCs are combined such that the resulting trigger towers point towards the nominal vertex as shown in figure 7.1. Hence, the fact that *ep* interactions occur at the interaction point is loosely taken into account. To avoid triggering on electronic noise, the analogue signals from the TTs are compared to a set of thresholds. Thus, if the signal from a specific TT is below threshold, that TT is ignored by any further summing algorithm. Finally, the signals of up to 4 TTs are combined into big towers (BT). After this summing process has finished, the signals are digitised. These digitised BT signals are then used to form all LAr calorimeter trigger elements. The hadronic part and the electromagnetic part include 256 BTs each. The following LAr calorimeter TEs were used to trigger CC events:

- *LAr_Etmiss*:
  The vector sum of the transverse components of the BT energies is calculated as follows:
  $$V = \sqrt{E_x^2 + E_y^2}, \tag{7.1}$$

where E_x and E_y are given by:.

$$E_x = \sum_{BT\ i} E_i^{BT} sin(\theta_i) cos(\phi_i), \tag{7.2}$$

$$E_y = \sum_{BT\ i} E_i^{BT} sin(\theta_i) sin(\phi_i). \tag{7.3}$$

E_i^{BT} is the energy measured in the ith BT. The LAr_Etmiss TE has a set of three thresholds of $V > 3.8$ GeV (low), $V > 4.4$ GeV (medium) and $V > 5.2$ GeV (high).

- LAr_IF:
  The energy sum E_{IF} of all the BTs in the forward region of the LAr Calorimeter (IF) defines the LAr_IF trigger element. A set of three thresholds is available: $E_{IF} > 2$ GeV (low), $E_{IF} > 7.5$ GeV (medium) and $E_{IF} > 20$ GeV (high).

- LAr_T0:
  The timing signal from the LAr Calorimeter is determined from the trigger tower signals. The signals of the trigger towers are copied with a delay of 500 ns. The crossing point between the delayed signal and the original signal determines the trigger tower that triggered during the t_0 bunch-crossing. These are then summed to big towers called BT_T0. If at least one BT_T0 is set, the LAR_T0 TE is set.

- LAr_BigRay:
  The LAr_BigRay TE is set if the energy of one BT is above threshold and can be combined with a track candidate of the z-vertex trigger.

- Big_T_miss:
  This L2 trigger element was specifically designed to trigger on a single jet topology. The TE is set whenever an energy of at least 2.5 GeV is found in one BT or in two adjacent ones [77].

With the introduction of the new jet-trigger [78], more complex TEs can be implemented. Here, the trigger elements will be based on the TT information.

Trigger Elements of the Tracking Chambers

- $zvtx_T0$ and $zvtx_sig > 1$:
  Before the luminosity upgrade, the z-vertex trigger used the information of the CIP and the COP as well as the first forward proportional chamber situated in the Forward tracking detector. The $zvtx_T0$ was set, once a track candidate originating from the interaction point ("ray") was found. The zvtx_sig TE is explained in section 6.6 on page 90.

- FwdRay_T0:
  Before the upgrade, this TE relied on the information of the three forward proportional chambers. It was set if a track candidate in the forward region was found. In the following text, the "OR" between the zvtx_T0 and FwdRay_T0 TEs is denoted as Ray_T0.

- DCr-ϕ_T0 and DCr-ϕ_Tc:
  The DCr-ϕ_T0 TE was set whenever a track that originated from the vertex region was found to cross the corresponding wire plane such that accurate timing information was obtained. The DCr-ϕ_Tc is set if three tracks that originated from the vertex region are found. The polar acceptance of the DCr-ϕ trigger is [35°,145°]. The transverse momentum threshold per track is around 420 MeV.

With the removal of the forward proportional chambers, the FwdRay_T0 TE is no longer available after the upgrade. It can, however, be replaced by a trigger element looking for a coincidence between the FTi2 and the CIP. Furthermore, the modified CIP does not provide information about the polar angle of a track candidate. Hence, the LAr_BigRay TE is no longer available after the upgrade.

7.3 Triggering Charged Current Events at HERA II

With the luminosity upgrade, the rate of charged current triggers is expected to rise by a factor 5. The aim of this study is to regain acceptable rates by using FTT trigger elements to reduce the rate and at the same time maintain the trigger efficiency, which was achieved at HERA I. The trigger studies in this and the following sections have been performed using a sample of charged current events, generated using data events and the Django MC. The trigger efficiencies of various trigger elements are calculated according to equations 6.1 and 6.2 displayed on page 88, depending on whether a MC selection or a data selection is used. The rates have been calculated using equation 6.3 displayed on page 89. In the first subsection (see subsection 7.3.1 on page 112), a set of appropriate cut variables are presented together with their respective trigger efficiencies. In the second subsection (see subsection 7.3.2 on page 115), the rate reductions that can be achieved when applying appropriate FTT trigger elements to the sub-triggers ST66 and ST77 are presented before a final conclusion is drawn. With the loss of ST71, a new low P_t^{miss} trigger has to be designed. The approach that was taken to achieve this goal as well as the trigger efficiencies and rates of the redesigned trigger are discussed in section 7.4.

7.3.1 Trigger Efficiencies for Appropriate Cut Variables

Because the triggering of charged current events mainly uses the energy imbalance measured in the LAr calorimeter, the missing transverse momentum measured by the FTT may help to reduce the CC rate. Figure 7.2 shows the correlation between the generated transverse momentum of the hadronic final state V_{gen} and the FTT reconstructed transverse momentum of the hadronic final state V_{FTT}. In order to make sure that the comparison is useful, the generated quark which balances the undetected neutrino was required to be within a θ range [40°,140°]. It can be seen that the correlation between the variables is rather diffuse with the FTT generally under-measuring the missing p_T and therefore V_{FTT} is not a suitable variable to use for selecting CC events.

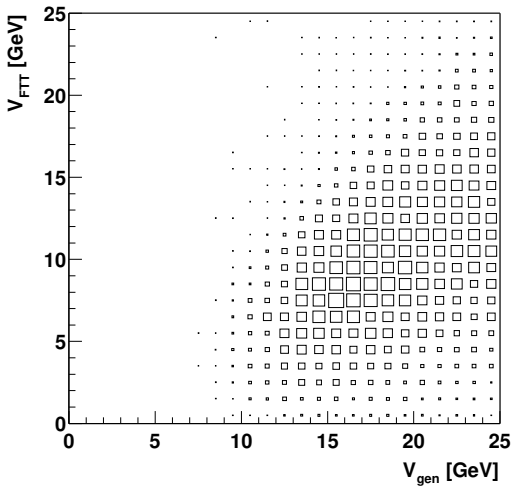

Figure 7.2: The correlation between the generated missing transverse momentum (V_{gen}) and the missing transverse momentum measured by the FTT (V_{FTT}) is shown for CC events where the hadronic final state is scattered in the central region.

Another important variable used in the selection of CC events is the quantity V_{ap}/V_p, which describes the ratio of the transverse momentum going into the opposite hemisphere as the net momentum of the hadronic final state to the transverse momentum going into the same hemisphere. In mathematical terms, this can be stated as follows:

$$V_{ap} = -\sum_i \frac{\vec{p}_{T,h} \cdot \vec{p}_{T,i}}{p_{T,h}}, \qquad \text{for all} \qquad \vec{p}_{T,h} \cdot \vec{p}_{T,i} < 0; \tag{7.4}$$

$$V_p = \sum_i \frac{\vec{p}_{T,h} \cdot \vec{p}_{T,i}}{p_{T,h}}, \qquad \text{for all} \qquad \vec{p}_{T,h} \cdot \vec{p}_{T,i} > 0. \tag{7.5}$$

In CC events, the ratio V_{ap}/V_p is expected to be close to zero, as the neutrino which balances the hadronic final state is not detected. The main backgrounds to charged current processes originate from photo-production, beam-gas interactions, and cosmics. V_{ap}/V_p is expected to be closer to one for all these processes. As the angular acceptance of the FTT is limited to the central region, some neutral current events can fake the charged current process when either the scattered electron or the neutral current jet remains undetected. Hence, a first investigation was performed to determine which region of phase space CC events could be distinguished from the NC events as well as the photo-production events by using these variables. This was done by investigating the $V_{ap} - V_p$ variable as reconstructed by the FTT. As figure 7.3(a) shows, the CC events are mainly situated in the bin $V_{ap} < 1$ GeV. The photo-production events shown in figure 7.3(c), which were generated using the Pythia MC, are mainly present below $V_p = 5$ GeV. Due to the fact that the NC cross-section is approximately 1000 times larger than the CC cross-section, 100000 events of selected NC data events were used compared to only 1000 CC MC events. For NC events, a weak correlation of V_{ap} with V_p can be seen. Only

a small fraction of NC events are present below $V_p = 1$ GeV (see figure 7.3(b)). Thus, although the acceptance of the FTT is limited by its polar acceptance, the CC events can be localised in a small region of the $V_{ap} - V_p$ phase space. Therefore, the variables V_{ap} and V_p are proposed for making selections of CC events.

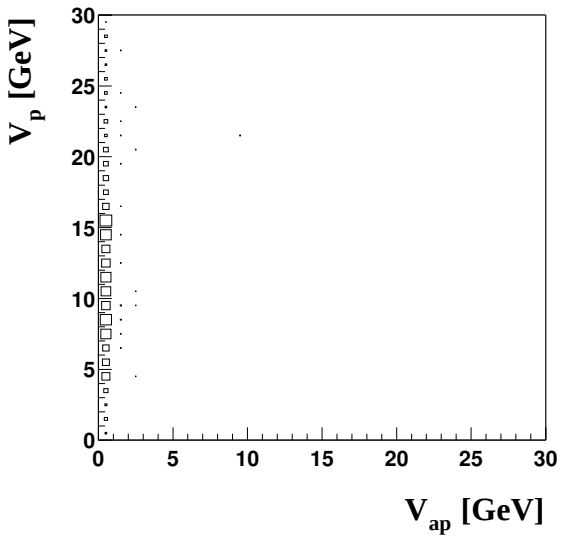

(a)

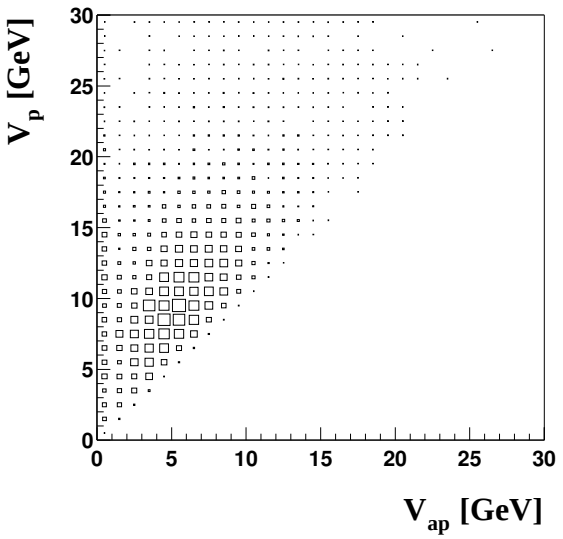

(b)

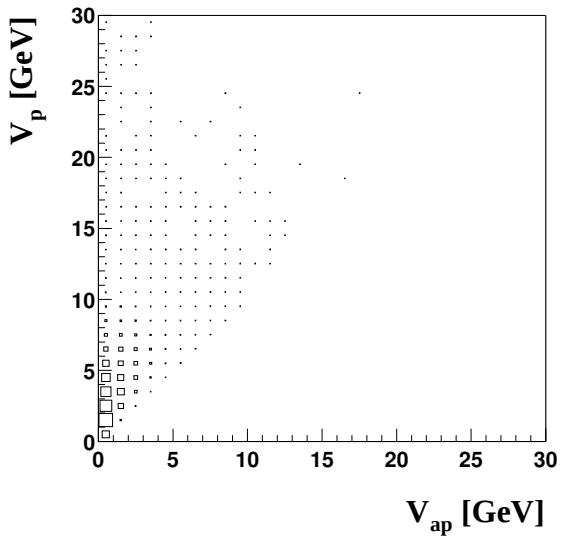

(c)

Figure 7.3: The $V_{ap} - V_p$ phase space is shown for (a) CC events, (b) NC events and (c) photo-production events. In cases (a) and (c), a selection of MC events was used whereas a data sample of selected NC events was used in (b).

The jet topology in CC events makes it is reasonable to think about selecting CC events by applying a cut on the track with the highest transverse momentum in the event. A trigger element based on the transverse momentum information of the highest p_T track that is found by the FTT can be implemented at the second level of the FTT. Figure 7.4 shows the trigger efficiency for selecting CC events as a function of the cut on the highest p_T track in the acceptance region of the FTT. For a jet with a polar angle larger than 50°, the trigger efficiency is shown for the scenario where at least one track was found by the FTT (open circles), $V_{ap} \leq 2$ GeV (triangles) and $V_{ap} \leq 1$ GeV (full circles). In this

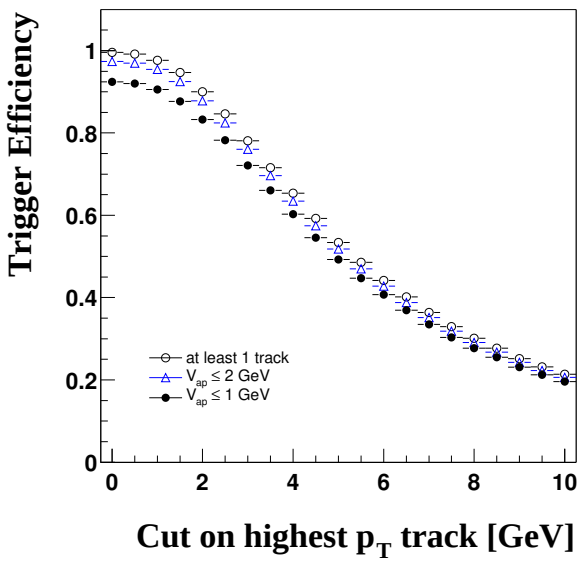

Figure 7.4: The efficiency of the FTT trigger elements "at least one track found by the FTT" (open circles), $V_{ap} \leq 2$ GeV (triangles) and $V_{ap} \leq 1$ GeV (full circles) is shown as a function of the highest p_T track found in the polar acceptance region of the FTT.

figure, the trigger efficiency drops rather quickly as the cut on the highest p_T track found by the FTT is increased.

Figure 7.5 shows the trigger efficiency of the trigger requirement $V_{ap} \leq 2$ GeV (full circles) and $V_{ap} \leq 1$ GeV (triangles) as a function of the cut on V_p. The polar angle of the jet is limited to regions above 50°. In both cases, the trigger efficiency drops off smoothly from 95% if no cut on V_p is applied to 70% if a cut $V_p > 10$ GeV is applied. It can be seen that in both scenarios, the trigger efficiency remains high over a large range of the cut variable $V_{p,\ FTT}$.

The feasibility of the above cut variables as trigger elements can be deduced from the resulting trigger rate. If the rate reduction is considered to be large enough and the loss in trigger efficiency is acceptable, the cut variable that is considered can be used as a trigger element for the proposed trigger. Hence, the next step is to look at the rate reductions resulting from the cuts that are put on the selection at the trigger level. The triggers to be studied at first are the sub-triggers ST66 and ST77.

7.3.2 Rate Reductions of Sub-Triggers ST66 and ST77

In this section, the rate reductions for ST66 and ST77 are presented, where the rate reductions are achieved through the use of FTT trigger elements available at L2 or L3. The respective sub-triggers have been used to estimate the respective rates.

Firstly, the behaviour of the respective trigger rates are studied as a function of the cut

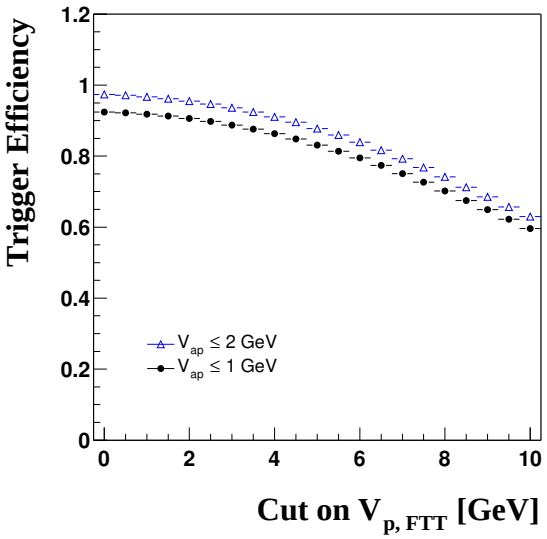

Figure 7.5: The efficiency of the FTT trigger elements $V_{ap} < 2$ GeV (full circles) and $V_{ap} < 1$ GeV (triangles) is shown as a function of the FTT measured on V_p cut variable. The CC Monte-Carlo was used.

V_p as measured by the FTT. From figure 7.6(a) it can be seen that the rate is reduced by approximately 30% if the cut $V_{ap} \leq 2$ GeV is applied. With the additional cut $V_p > 3$ GeV, the rate is reduced by 80% (ie factor 5 reduction) whilst maintaining high efficiency (see figure 7.5). Similarly, the rate is reduced by 40% if the cut $V_{ap} \leq 1$ GeV is applied. This requirement combined with the $V_p > 2$ cut again reduces the rate by a factor 5. Figure 7.6(b) shows the rate reduction for sub-trigger ST77 if similar cuts are applied. It can be seen that for equivalent FTT requirements, the rate of sub-trigger ST77 is reduced significantly more than in the case of sub-trigger ST66. Due to the lower Et_miss threshold and the lack of the LAr_T0 TE, sub-trigger ST77 triggers on a lot of background events that can be rejected with the additional FTT requirements. FTT reconstructed tracks are constrained by the vertex fit, so that the additional FTT cuts filter out a lot of these background events. Thus, the factor of 5 in rate reduction is already reached if looser cuts are applied. Both of the following cut scenarios reduce the rate by 80%:

(a) $V_{ap} \leq 2$ GeV and $V_p > 1.5$ GeV

(b) $V_{ap} \leq 1$ GeV and $V_p > 1$ GeV

If cut (a) is applied, the loss in trigger efficiency is approximately 3%. It is thus superior to cut (b) for which the loss in efficiency increases to 10%. Secondly, the rate behaviour of the respective sub-triggers ST66 and ST77 was studied as a function of a p_T cut made on the track with the highest p_T in the acceptance region of the FTT. In Figure 7.7, three cases are presented for sub-triggers ST66 and ST77 respectively. In the first example (open circles), at least one track has to be found by the FTT. In the second (triangles), only data with a value of V_{ap} below a threshold of 2 are accepted. In the third example, the cut $V_{ap} \leq 1$ GeV was applied. A significantly larger rate reduction for sub-trigger

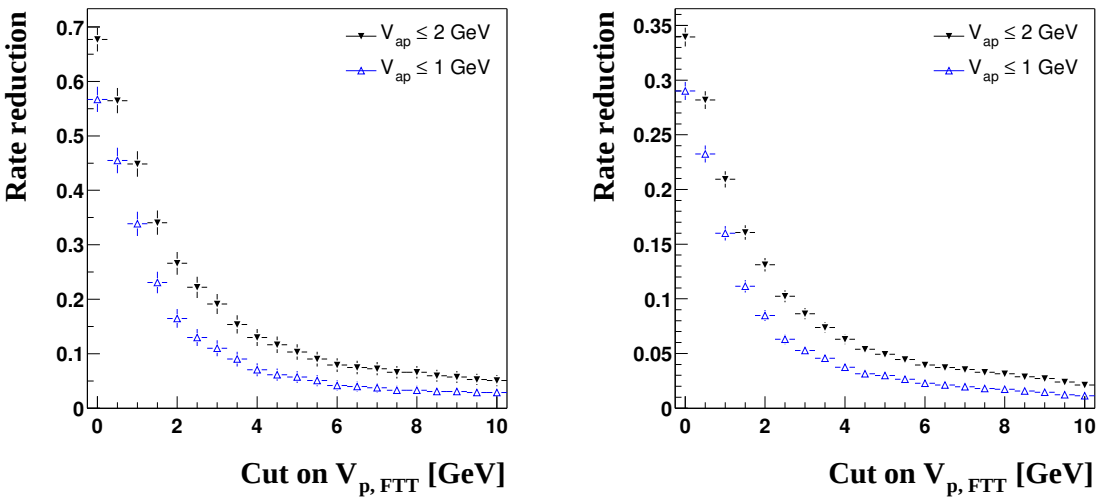

(a) *(b)*

Figure 7.6: (a) The rate reduction of an FTT validated ST66 is shown as a function of the cut on V_p that is measured by the FTT. (b) The rate reduction of an FTT validated ST77 is shown as a function of the cut on V_p that is measured by the FTT.

ST77 compared to sub-trigger ST66 is again seen in this figure. The requirement of at least one track with a p_T of 0.1 GeV in the acceptance region of the FTT reduces the rate by 20% and 60% for sub-triggers ST66 and ST77 respectively.

In the case of sub-trigger ST66, the rate reduction of a factor 5 is achieved if either of the following cuts is applied:

(a) $V_{ap} \leq 1$ GeV and $hpt > 1$ GeV,

(b) $V_{ap} \leq 2$ GeV and $hpt > 2$ GeV,

where *hpt* signifies the "highest p_T track found by the FTT at L2". If cut (a) is applied, the resulting trigger efficiency is approximately 90%. Applying cuts (b) actually worsens the trigger efficiency down to 87%.

In the case of sub-trigger ST77, the factor 5 in rate reduction is achieved if either of the following cuts are applied:

(a) $hpt > 1$ GeV,

(b) $V_{ap} \leq 1$ GeV and $hpt > 1$ GeV,

(c) $V_{ap} \leq 2$ GeV and $hpt > 1$ GeV.

If only the $hpt > 1$ GeV cut is applied, the resulting trigger efficiency is only reduced by 2% whereas the cut combinations (b) and (c) worsen the trigger efficiencies significantly

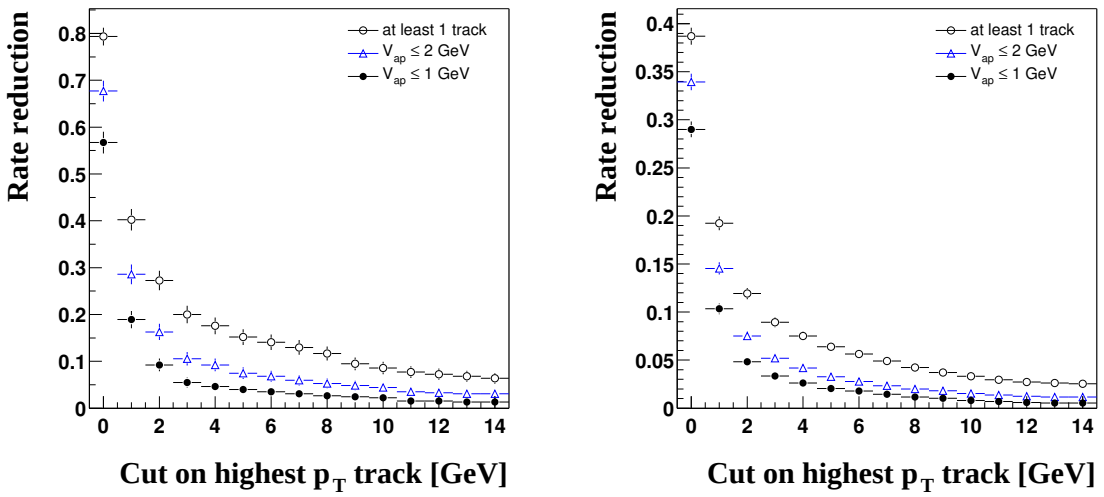

(a) *(b)*

Figure 7.7: (a) The rate reduction of an FTT validated ST66 is shown as a function of the cut on the highest p_T track as measured by the FTT. (b) The rate reduction of an FTT validated ST77 is shown as a function of the cut on the highest p_T track as measured by the FTT.

more. Thus, the trigger efficiency, if the cut combinations (b) or (c) are applied, is approximately 95% or 90% respectively.

7.3.3 Conclusion

Different FTT cuts have been applied to add additional requirements to the sub-triggers ST66 and ST77. In the case of sub-trigger ST66 a validation through the following combination of L3 FTT trigger elements would result in an efficiency loss of only 3%:

- $V_{ap} \leq 2$ GeV,
- $V_p > 1.5$ GeV.

Sub-trigger ST77 is more susceptible to background. The FTT validation of this sub-trigger through a requirement that at least one track was found in the FTT acceptance region already reduces the rate by 60%. Validating the sub-trigger with the following L2 FTT trigger element results in an inefficiency of only 2%:

- *hpt*> 1 GeV.

The FTT is thus able to reduce the rate of both ST66 and ST77 by a factor 5 without significant efficiency loss.

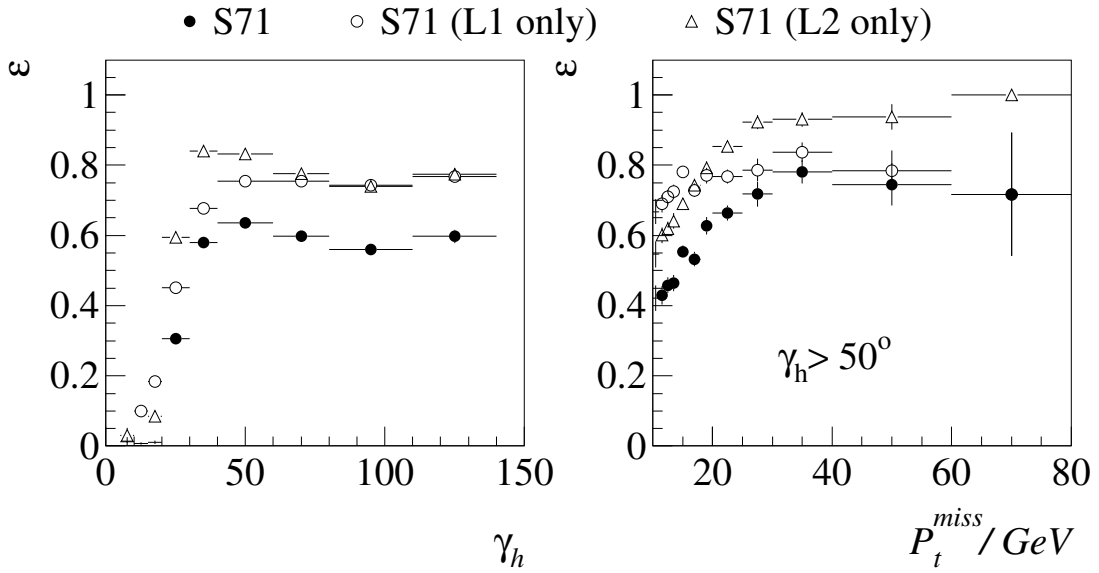

Figure 7.8: The efficiency of sub-trigger S71 is shown against γ_h (left) and the missing P_T (right). It can be seen that the efficiency is around 40 to 60% at low values of missing P_T.

7.4 A Redesigned Low P_t^{miss} Trigger

In 1997, the sub-trigger ST71 was designed and implemented to specifically improve the trigger efficiency for CC events where the hadronic final state particles have a low transverse momentum [79]. This allows charged current measurements to be made in an extended phase space. The efficiency is shown in figure 7.8 [79]. During HERA I, the sub-trigger ST71 had a rate of 30 Hz at L1. This rate was reduced to approximately 1 Hz by validating the logical trigger element combination of ST71 with the L2 Big_T_miss TE. With the upgrade, however, the H1 detector was modified, and some detector parts were removed or replaced. The CIP has been modified to better reject background events and the polar angle θ is not calculated at the trigger level to combine the chamber hits to tracks. As a consequence, the combination of a Big Ray with a BT is not possible at the trigger level. Furthermore, the Ray_T0, which was used to increase the efficiency of sub-trigger ST71 at low P_t^{miss} [79], is no longer available. This means that the sub-trigger ST71 needs to be reinvented, possibly by using the FTT.

In order to do this, the minimum bias sub-trigger ST32 is used as a basis. After the presentation of the trigger efficiencies of the various FTT trigger elements, the rate of a LAr_Etmiss TE validated sub-trigger ST32 is extracted assuming that the rate reduction for the L1 trigger logic for ST71 is the same as that for ST32 (see table 7.2). Then, the independent sub-trigger ST77 is used to estimate the rate reductions of the new sub-trigger. It was realised that sub-trigger ST77 is best for the rate estimate because it only relies on the LAr_Etmiss> 1 TE and not on any further calorimeter trigger element as is the case for sub-trigger ST66. Furthermore, it was shown in section 7.3.2 that the rate reduction of ST77 due to the requirement of FTT TEs is more significant than in the case

of sub-trigger ST66 due to the larger background content. Hence, it can be argued that a LAr_Etmiss> 0 TE triggers on even more background events and thus the resulting estimate of the rate reduction due to the applied FTT TEs is underestimated. As a consequence, the resulting rate estimate is conservative.

Sub-trigger	Combination of TEs	Unprescaled rate at L1 Hz
ST32	$zvtx_sig1 \wedge DCr\phi_Tc \wedge DCr\phi_T0 \wedge Ray_T0$	300

Table 7.2: The combination of trigger elements used by sub-trigger ST32. The unprescaled L1 trigger rate of ST32 during the HERA I running period is also shown.

In [79], the trigger efficiency of the Big_T_miss TE for events with $\gamma_h > 25°$ was found to be $83 \pm 0.1\%$. If the same cut is applied on the CC selection, a similar TE LAr_Etmiss> 0 selection has a trigger efficiency of $93 \pm 0.1\%$ (cf. figure 7.9(b)). The aim is to use this trigger element in conjunction with the FTT to set up a new trigger that has a rate which is reduced by a factor 5 compared to the rate of sub-trigger ST71. The trigger efficiencies of the different LAr_Etmiss thresholds are shown in figure 7.9. It can be seen that the efficiency to trigger on events with a low p_T hadronic final state of 12 GeV increases from approximately 40 % if the highest threshold is required, to above 60 % if the lowerest one is applied.

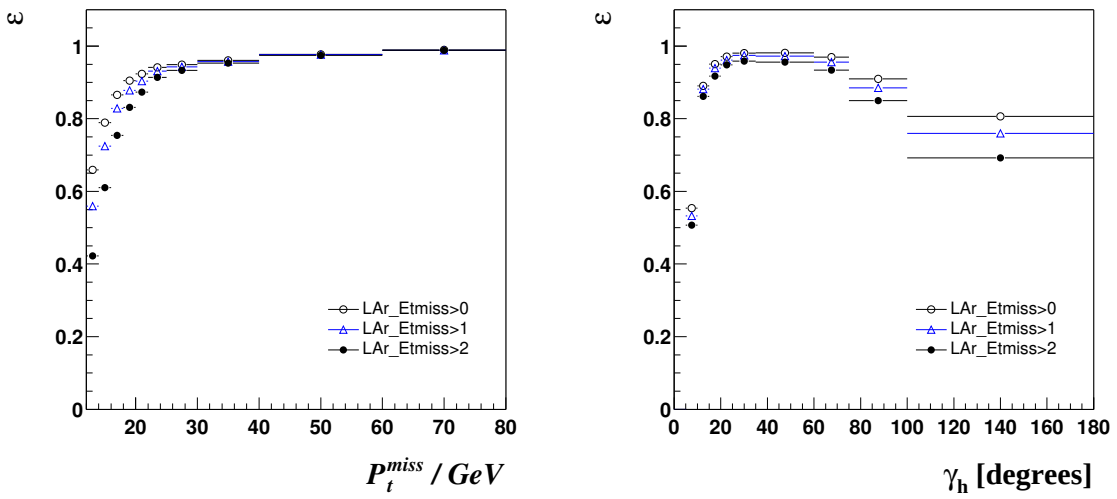

(a) *(b)*

Figure 7.9: The trigger efficiency of the LAr_Etmiss trigger element is shown as a function of (a) the offline reconstructed transverse momentum of the hadronic final state P_t^{miss} and (b) the net polar angle of the hadronic final state γ_h. The trigger efficiency is shown for $LAr_Etmiss > 0$ (open circles), $LAr_Etmiss > 1$ (full circles) and $LAr_Etmiss > 2$ (triangles)

Sub-trigger ST71 contains the DCRPh_Tc trigger element. In figure 7.10, the trigger efficiency of this trigger element is compared to a variety of potential FTT trigger elements. The DCRPh_Tc trigger element (full squares) is 87% efficient if no cut on the highest p_T

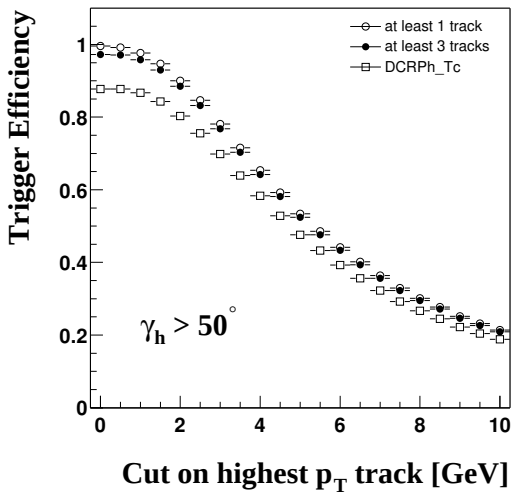

Figure 7.10: The trigger efficiency is shown for the DCRPh_Tc trigger element (open squares), the requirement of finding at least 1 FTT reconstructed track (open circles) and the requirement of finding at least 3 FTT reconstructed tracks (full circles). The trigger efficiency is shown as a function of the cut on the highest p_T track found in the FTT acceptance region.

track within the FTT acceptance is applied. The trigger efficiency of an FTT trigger element requiring at least 3 tracks in the acceptance region of the FTT (full circles) is 97%. This is only marginally worse than the trigger efficiency of a trigger element requiring that at least one of the tracks is found by the FTT (open circles). Hence, the trigger efficiency is improved by 10% by loosening the polar acceptance and track threshold requirements. A TE requiring that the highest p_T track found by the FTT is above a threshold of 2 GeV as well as at least three FTT reconstructed tracks above 0.1 GeV results in approximately the same efficiency as the one of the DCRPh_Tc TE.

Figure 7.11 shows the trigger efficiency of ST32 (open squares) as well as the combination of two FTT trigger elements with the requirement of a z-vertex significance peak (full circles) as a function of the vector sum of the hadronic final state transverse momentum P_t^{miss}. The two combinations have a similar efficiency.

Figure 7.12 shows the trigger efficiencies of the combination of two FTT trigger elements with the requirement of a z-vertex significance peak together with additional FTT requirements as a function of the vector sum of the hadronic final state P_t^{miss}. The comparison between the crossed scenario and the open circles scenario shows that a harsher cut on the highest p_T track found by the FTT, mainly affects events with a low P_t^{miss} hadronic final state. With the aim to improve the efficiency between 12 and 15 GeV, it looks like a harsher cut on V_p is preferable to a harsher cut on the *hpt*.

In order to determine the trigger rate of the new trigger, data from a L2-L4 transparent run from 1997 was used. With the high prescale of ST32, it was only possible to set an upper limit on the trigger rate for ST32 which is validated by the LAr_Etmiss TE. Taking advantage of the fact that the combination of L1 trigger elements belonging to sub-trigger

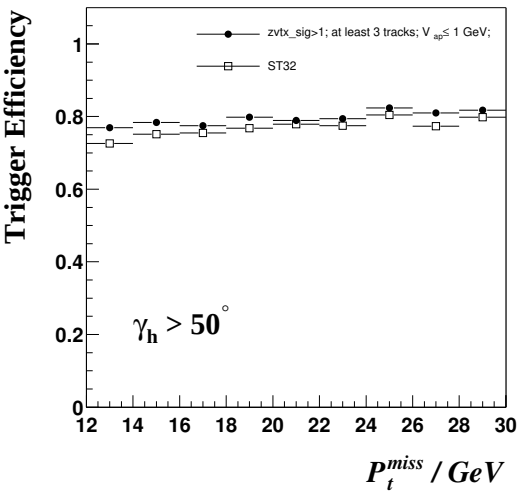

Figure 7.11: The trigger efficiency is shown for sub-trigger ST32 (open squares) and for the requirements of at least 3 FTT reconstructed tracks as well as a z-vertex significance peak and the requirement that $V_{ap} \leq 1$ GeV (full circles). The trigger efficiency is shown as a function of the missing transverse momentum P_t^{miss}.

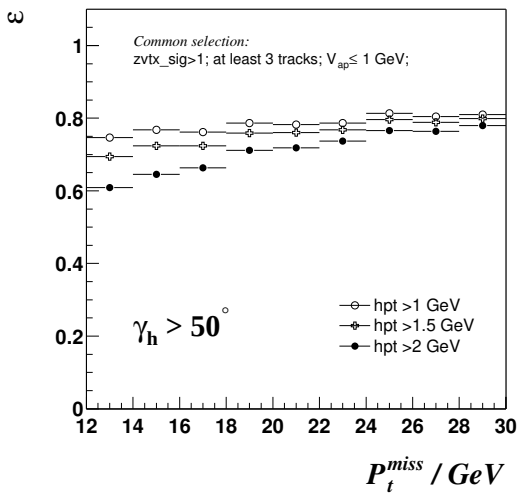

Figure 7.12: The trigger efficiency is shown as a function of the missing transverse momentum P_t^{miss} for the requirement of finding at least 3 FTT reconstructed tracks as well as a z-vertex significance peak and the requirement that $V_{ap} \leq 1$ GeV in all three cases. Additionally, a V_p cut as well as a cut on the highest p_T track were required.

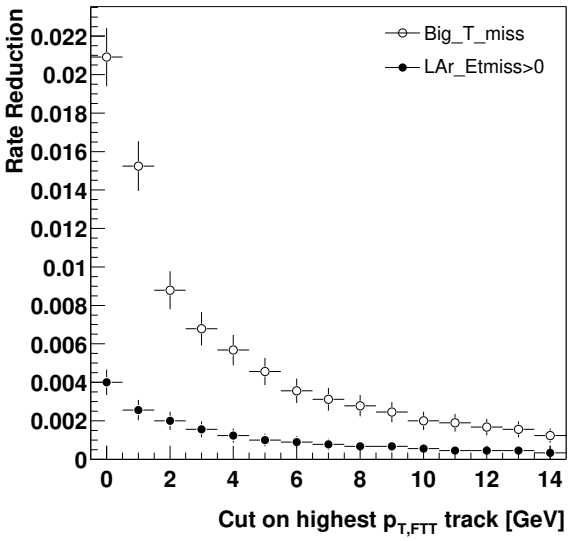

Figure 7.13: The rate reduction of the L1 trigger element combination belonging to sub-trigger ST71 due to the Big_T_miss TE (open circles) and the Et_miss> 0 TE (full circles) is shown as a function of the highest p_T track found by the FTT.

ST71 is similar to the combination of L1 trigger elements belonging to sub-trigger ST32, an alternative estimate of the rate reduction of ST32 can be deduced from sub-trigger ST71. Figure 7.13 shows the rate reduction of the L1 trigger element combination of sub-trigger ST71 as a function of the cut on the highest p_T track that is found by the FTT for two separate scenarios. In the first case (open circles), the rate reduction is due to the validated of ST71 through its L2 condition (Big_T_miss TE) as well as the FTT condition. In the second scenario (closed circles) the rate reduction is due to the validation of the same sub-trigger trough the $LAr_Etmiss > 0$ condition as well as the FTT condition. Knowing that the L1 rate of ST71 was 30 Hz on average, the average rate if the L2 condition of ST71 is applied, reduces the rate down to 0.66 Hz before any FTT requirements. With the LAr_Etmiss> 0 condition put on top of the L1 trigger elements ST71 the rate is reduced even further down to 0.12 Hz. Scaling the rate reduction factor with the unprescaled rate of sub-trigger ST32 then results in an estimated ST32 rate of 1.2 Hz, knowing the unprescaled L1 rate of ST32 is 300 Hz (cf. table 7.2).

Next, the rate reduction for ST32 due to the following combination of trigger elements is evaluated:

- $V_{ap} \leq 1$ GeV;
- $n_{tracks,min} = 3$;
- $zvtx_sig > 1$.

In order not to introduce a bias in the calculation of the rate reduction factor, sub-trigger ST77 was used as a monitor trigger. After the rate reduction factor was determined,

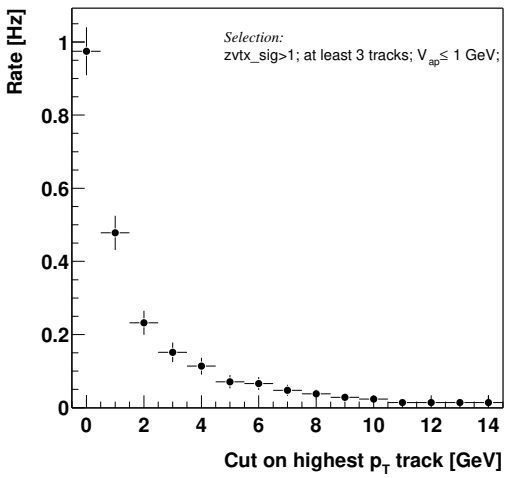

Figure 7.14: The rate of an FTT validated ST77 is shown as a function of the cut on the highest p_T online reconstructed track in the FTT acceptance region. Here, ST77 was used as a monitor trigger.

the rate of the potential new trigger was deduced by scaling the rate reduction factor to the previously estimated pre-upgrade rate of ST32 when the $LAr_Etmiss > 0$ condition is applied (cf. text related to figure 7.13). The resulting rate reduction is shown in figure 7.14 as a function of the cut on the highest p_T track found by the FTT. The requirement $hpt > 1$ GeV reduces the rate to approximately 0.5 Hz. The harsher cut $hpt > 2$ GeV reduces the rate to approximately 0.25 Hz.

In order to reduce the rate further, it was decided to investigate the rate as a function of V_p. Figure 7.15(a) shows the rate of the above mentioned combination of the trigger elements as a function of the cut on V_p as measured by the FTT. In all three cases, the cut on V_p does not affect the rate unless the highest p_T track found by the FTT is smaller than the cut on V_p. If the cut $V_p > 4.5$ GeV is applied, the rates of all three scenarios are equivalent with a rate below 0.2 Hz.

Figure 7.15(b) shows the corresponding trigger efficiency of each potential new CC sub-trigger. For all three scenarios, the trigger efficiency is similar. However, the scenario requiring a *hpt* greater than 1 GeV is preferred as the efficiency is slightly higher. Hence, the proposed CC trigger includes the trigger elements shown in table 7.3.

The trigger efficiency of the redesigned sub-trigger is thus slightly lower than that of sub-trigger ST71. In the range $12 < P_t^{miss} < 14$ GeV the trigger efficiency is approximately 35 %. However, this trigger can probably still be improved. For example, a trigger element similar to the Fwd_Ray_T0 could be implemented by requiring a coincidence between a track found by the CIP z-vertex trigger and the time of flight detector FTi2. The "OR" between this trigger element and the trigger element combination of the proposed CC trigger should raise the trigger efficency for forward jets. As most of the CC jets go into the forward region though, the rate for such a trigger needs to be checked in a test run.

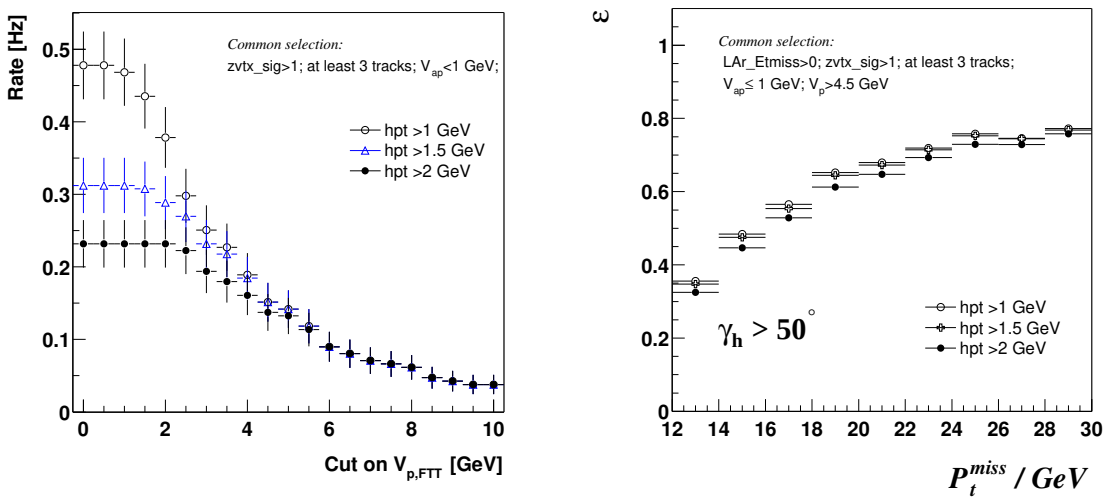

(a) *(b)*

Figure 7.15: (a) The rate of the potential redesigned CC sub-trigger is shown as a function of the cut on V_p as measured by the FTT. (b) The corresponding trigger efficiencies are shown as a function of the offline measured missing transverse momentum P_t^{miss}.

level	trigger element
$L1$	LAr_Etmiss> 0
	zvtx_sig> 1
$L2$	$n_{tracks,min} = 3$
	$hpt > 1$ GeV
$L3$	$V_{ap} \leq 1$ GeV
	$V_p > 4.5$ GeV

Table 7.3: The trigger levels and the corresponding trigger elements used by the proposed CC trigger are shown above.

7.4.1 Conclusion

It is concluded that with the help of the FTT, the existing sub-trigger ST71 can be replaced with a new sub-trigger. The LAr_Big_Ray TE as well as the Fwd_Ray_T0 TE are lost after the upgrade so the polar acceptance region of the new sub-trigger will be slightly smaller than that of the existing sub-trigger ST71. The trigger efficiency of sub-trigger ST71 was significantly improved with the introduction of a logical "OR" between the DCr-ϕ based TEs and the Fwd_Ray_T0 TE at L1. Although this trigger combination or a similar one would not completely replace the existing low P_t^{miss} trigger, the loss in trigger efficiency for events between 12 and 15 GeV could be limited to 5%. At the same time, a rate reduction by a factor 5 compared to the sub-trigger ST71 could be achieved.

7.5 Summary

In this chapter, the trigger efficiencies and rates of the current CC sub-triggers ST66 and ST77 have been presented. It was shown that a reduction of a factor 5 could be achieved when additional FTT requirements are applied. At the same time, the trigger efficiencies of the existing sub-triggers ST66 and ST77 are maintained.

Furthermore, it was shown that a redesigned low P_t^{miss} sub-trigger with a post-upgrade rate of less than 1 Hz after L3 is possible. Compared to the sub-trigger ST71 used during HERA I, the efficiency loss is only 5%, although TEs based on forward tracks are no longer available. This trigger efficiency may be regained by combining the trigger elements from the proposed low P_t^{miss} CC trigger with a trigger element requiring a coincidence between CIP and FTi2 through a logical "OR". In order to determine the exact rate and efficiency for a low P_t^{miss} trigger with these additional requirements, a test run is necessary.

Summary and Outlook

This thesis was concerned with the algorithms and the performance of the Fast Track Trigger. Part of this thesis was dedicated to the description of the first level trigger chain. It was found that the FTT L1 trigger elements could be delivered to the central trigger within approximately 2130 ns after the event t_0. Knowing that the central trigger needs to take a decision at a time of 2304 ns after the event occurred, the timing of the L1 chain is very tight. The validation of tracks occurring in the bunch crossing of origin currently takes 100 ns and can probably be improved.

Although the track segment finder has been written and simulated, it still needs testing on the actual hardware. This test will confirm whether the track segment finder also finds the right track segments if a known hit pattern is processed.

The rest of this thesis was dedicated on the design of new triggers. Due to the HERA upgrade, some of the HERA I trigger elements are no longer available. The aim of these studies was to maintain the efficiency of the HERA I triggers as well as reducing their rate by a factor 5 to meet the demands of HERA II. A new diffractive J/Ψ photo-production trigger that meets these requirements has been designed. This trigger would need to be tested once the FTT is running at HERA II. Depending on the rate of the trigger, the trigger efficiency can even be improved by loosening its requirements. Furthermore, a high $|t|$ proton-dissociative ρ^0 trigger was presented. With the help of the FTT, it is actually possible to trigger on ρ^0 events which a trigger efficiency much improved compared to HERA I.

Considering the rate increase of a factor 5, the charged current triggers have to be slightly modified to cope with the rate increase. With the help of the FTT, it has been shown that the rates of the present charged current triggers can be reduced by a factor of 5 with only an acceptable minor loss in efficiency relative to the HERA I efficiency. Charged current events which have a jet with a low p_T of approximately 12 to 15 GeV are hard to trigger at H1. With the help of the FTT, a cut based on the momentum present in both the neutrino and the hadron hemispheres was possible based on tracking information. Considering that the rate had to be reduced by a factor of 5 with respect to the rate of the existing low p_T trigger, an efficiency of 35% in the central region was achieved.

Appendix A

The Main Control unit of the Track Segment Finder

The language that was used to design of the algorithm was VHDL. The code presented here is used to control the sequence of states the algorithm is required to run through.

A.1 VHDL programming

One main building block, called 'entity', is used in the VHDL language. The 'entity only holds the input and output signals. It can thus be thought of as a black box. In the program shown below, the 'entity' is called *active_state*. Together with each 'entity' comes the 'architecture'. Here, the internal processing is described. The 'architecture' of the entity *active_state* presented here is called *RTL*. To find out more about VHDL programming a detailed description can be found in [80].

A.2 The Program

```
entity active_state is
   port(
      HClk       : in  std_logic;
      Clk80      : in  std_logic;
      Rst        : in  std_logic;
      Pien       : in  std_logic;
      FClr_N     : in  std_logic;
      busy       : in  std_logic;
      Status     : out std_logic_vector(2 downto 0)
    );
 end active_state;


architecture RTL of active_state is

   type triggerstate is (idle,
                         pre_L1active1,
```

```
                      pre_L1active2,
                      L1active,
                      L23active1,
                      L23active2,
                      L23active3);

  signal Clk10        : std_logic;
  signal next_state   : triggerstate;
  signal Status_s     : std_logic_vector(2 downto 0);
  signal count_s      : integer range 0 to 23;

begin

   Status <= Status_s;

   status_ctrl: process(Clk80, Rst)
   begin
     if Rst = '1' then
       next_state      <= idle;
       Status_s        <= "111";
       count_s         <= 0;
     elsif Clk80'event and Clk80 ='1' then
       Clk10 <= HClk;
       case next_state is
         when idle =>
           if Clk10 = '0' and HClk ='1' then
             next_state      <= pre_L1active1;
             Status_s        <= "000";
             count_s         <= 0;
           else
             next_state      <= idle;
             Status_s        <= "111";
             count_s         <= 0;
           end if;
         when pre_L1active1 =>
           if Clk10 = '0' and HClk ='1' then
             count_s         <= count_s + 1;
           else
             count_s         <= count_s;
           end if;
           if count_s = 22 then
             if Clk10 = '0' and HClk ='1' then
               next_state      <= pre_L1active2;
               Status_s        <= "001";
             else
               next_state      <= pre_L1active1;
               Status_s        <= "000";
             end if;
           end if;
         when pre_L1active2 =>
           if Pien = '1' then
             if Clk10 = '0' and HClk ='1' then
               next_state      <= L1active;
               Status_s        <= "011";
             else
               next_state      <= pre_L1active2;
               Status_s        <= "001";
             end if;
               else
                 next_state      <= pre_L1active2;
                 Status_s        <= "001";
               end if;
            when L1active =>
               if Clk10 = '0' and HClk ='1' then
                 if Pien = '1' then
                   next_state      <= L1active;
                   Status_s        <= "011";
                 else
                   next_state      <= L23active1;
                   Status_s        <= "010";
                 end if;
               else
```

```
                next_state      <= L1active;
                Status_s        <= "011";
              end if;
            when L23active1 =>
              if Clk10 = '0' and HClk ='1' then
                if FClr_N = '0' then
                  next_state      <= idle;
                  Status_s        <= "111";
                elsif busy = '1' then
                  next_state      <= L23active2;
                  Status_s        <= "100";
                else
                  next_state      <= L23active1;
                  Status_s        <= "010";
                end if;
              else
                if busy = '1' then
                  next_state      <= L23active2;
                  Status_s        <= "100";
                else
                  next_state      <= L23active1;
                  Status_s        <= "010";
                end if;
              end if;
            when L23active2 =>
              if Clk10 = '0' and HClk ='1' then
                if FClr_N = '0' then
                  next_state      <= idle;
                  Status_s        <= "111";
                elsif busy = '0' then
                  next_state      <= L23active3;
                  Status_s        <= "110";
                else
                  next_state      <= L23active2;
                  Status_s        <= "100";
                end if;
              else
                if busy = '0' then
                  next_state      <= L23active3;
                  Status_s        <= "110";
                else
                  next_state      <= L23active2;
                  Status_s        <= "100";
                end if;
              end if;
            when L23active3 =>
              if Clk10 = '0' and HClk ='1' then
                if FClr_N = '0' then
                  next_state      <= idle;
                  Status_s        <= "111";
                else
                  next_state      <= L23active3;
                  Status_s        <= "110";
                end if;
              else
                next_state      <= L23active3;
                Status_s        <= "110";
              end if;
            end case;
        end if;
    end process status_ctrl;

end RTL;
```

Bibliography

[1] G. D. Coughlan and J. E. Dodd. *The Ideas of Particle Physics: an Introduction for Scientists*. Cambridge University Press, second edition, 1994.

[2] D. Rutherford. *Phil. Mag.*, 21:669, 1911.

[3] R. Hofstader. *Rev. Mod. Phys.*, 28:214, 1956.

[4] E. D. Bloom et al. High-Energy Inelastic $e-p$ Scattering at 6° and 10°. *Phys. Rev. Lett.*, 23:930–934, 1969.

[5] Martin Breidenbach et al. Observed Behavior of Highly Inelastic Electron-Proton Scattering. *Phys. Rev. Lett.*, 23:935–939, 1969.

[6] K. Hagiwara et al. Review of Particle Physics. *Phys. Rev.*, D66:010001, 2002.

[7] Jr. Callan, Curtis G. and David J. Gross. High-Energy Electroproduction and the Constitution of the Electric Current. *Phys. Rev. Lett.*, 22:156–159, 1969.

[8] H1 collaboration. Measurement and QCD Analysis of Neutral and Charged Current Cross Sections at HERA. March 2003. Submitted to Eur. Phys. J. C., DESY 03-038.

[9] I. J. R. Aitchison and Hey A. J. G. *Gauge Theories in Particle Physics: A Practical Introduction*. Hilger, Bristol, UK, 1989.

[10] J. D. Bjorken. Asymptotic Sum Rules at Infinite Momentum. *Phys. Rev.*, 179:1547–1553, 1969.

[11] A. C. Benvenuti et al. A High Statistics Measurement of the Deuteron Structure Functions F_2 (x, Q^2) and R from Deep Inelastic Muon Scattering at High Q^2. *Phys. Lett.*, B237:592, 1990.

[12] S. Bethke. Determination of the QCD Coupling α_s. *J. Phys.*, G26:R27, 2000.

[13] Guido Altarelli and G. Parisi. Asymptotic Freedom in Parton Language. *Nucl. Phys.*, B126:298, 1977.

[14] T. Regge. Introduction to Complex Orbital Momenta. *Nuovo Cim.*, 14:951, 1959.

[15] H. L. Lai et al. Improved Parton Distributions from Global Analysis of recent Deep Inelastic Scattering and inclusive Jet Data. *Phys. Rev.*, D55:1280–1296, 1997.

[16] C. Adloff et al. Measurement of D* Meson Cross Sections at HERA and Determination of the Gluon Density in the Proton using NLO QCD. *Nucl. Phys.*, B545:21–44, 1999.

[17] P. D. Collins. *An Introduction to Regge Theory and High-Energy Physics*. Cambridge University Press, 1977.

[18] A. Donnachie and P. V. Landshoff. Total Cross-Sections. *Phys. Lett.*, B296:227–232, 1992.

[19] J. R. Forshaw and D. A. Ross. *Quantum Chromodynamics and the Pomeron*. University Press, Cambridge, UK, 1997.

[20] Aharon Levy. Measurements of Diffractive Processes at HERA. 2003.

[21] H1 collaboration. Elastic Photoproduction of J/ψ Mesons at HERA. 2003. Contributed paper to the International Europhysics Conference on High Energy Physics, EPS03 in Aachen, Germany, H1prelim-03-075.

[22] F. E. Low. A Model of the Bare Pomeron. *Phys. Rev.*, D12:163, 1975.

[23] H1 collaboration. Elastic Electroproduction of ρ Mesons at High Q^2 at HERA. 2003. Contributed paper to the International Europhysics Conference on High Energy Physics, EPS03 in Aachen, Germany, H1prelim-02-015.

[24] S. Chekanov et al. Measurement of Proton Dissociative Diffractive Photoproduction of Vector Mesons at large Momentum Transfer at HERA. *Eur. Phys. J.*, C26:389–409, 2003.

[25] H1 collaboration. Diffractive Photoproduction of J/ψ Mesons with Large Momentum Transfer at HERA. June 2003. Submitted to Phys. Lett. B., DESY 03-061.

[26] H1 collaboration. *ep* Physics beyond 1999. H1 Internal Note H1-10/97-531, October 1997.

[27] G. Hoffstaetter. Talk in HERA-Status Seminar, Zeuthen, 2002.

[28] B. Andrieu et al. Results from Pion Calibration Runs for the H1 Liquid Argon Calorimeter and Comparisons with Simulations. *Nucl. Instrum. Meth.*, A336:499–509, 1993.

[29] H. Behrend et al. Technical Proposal to build Silicon Tracking Detectors for H1. H1 Internal Note 92-226, May 1992.

[30] J. Burger et al. The Central Jet Chamber of the H1 experiment. *Nucl. Instrum. Meth.*, A279:217–222, 1989.

[31] H1 collaboration. Proposal for an Upgrade of the H1 Forward Track Detector for HERA 2000. June 1998. DESY PRC 98/06.

[32] BPC Working Group. Information available on Web: http://www-h1.desy.de/h1det/tracker/bpc/bpcpage.htm.

[33] B. Andrieu et al. The H1 Liquid Argon Calorimeter system. *Nucl. Instrum. Meth.*, A336:460–498, 1993.

[34] R. D. Appuhn et al. The H1 Lead/Scintillating-Fibre Calorimeter. *Nucl. Instrum. Meth.*, A386:397–408, 1997.

[35] W. Hildesheim, V. Reich, and M. Seidel. The Plug Calorimeter User's Guide. August 1994. H1 Internal Note H1-08/94-372.

[36] H. Itterbeck et al. Improvement of the Trigger Timing of the H1 Digital Muon System. February 1995. H1 Internal Note 95-427.

[37] P. Biddulph et al. The H1 Forward Muon Spectrometer. *Nucl. Instrum. Meth.*, A340:304–308, 1994.

[38] T. Ahmed et al. A Pipelined First Level Trigger for the H1 Forward Muon Spectrometer. *Nucl. Instrum. Meth.*, A364:456–472, 1995.

[39] K. Flamm. Messung von Strahluntergrund bei HERA für den Betrieb von H1. Master's thesis, Universität Hamburg, 1992.

[40] R. D. Appuhn et al. July 1996. Contributed paper to the 28th International Conference On High Energy Physics, Warsaw, Paper pa17-026.

[41] H. Bethe and W. Heitler. On the Stopping of Fast Particles and on the Creation of Positive Electrons. *Proc. Roy. Soc. Lond.*, A146:83, 1934.

[42] J.H. Köhne et al. Realization of a Second Level Neural Network Trigger for the H1 Experiment at HERA. H1 Internal Note H1-01/97-509, January 1997.

[43] J.C. Bizot et al. Status of Simulation for a Topological Level 2 Trigger. H1 Internal Note H1-02/92-212, February 1992.

[44] J.C. Bizot et al. Strategy Studies for the H1 Topological L2-Trigger (L2TT). H1 Internal Note H1-01/97-508, January 1997.

[45] Ch. Wissing. *Entwicklung eines Simulationsprogramms und Implementierung schneller Spurfitalgorithmen für den H1-Driftkammertrigger.* PhD thesis, Universität Dortmund, 2003.

[46] A. Campbell et al. Proposal to Merge Level-4 and Level-5 Systems of the H1 Experiment. Proposal submitted to the Physics Research Committee, DESY internal report PRC 99/03, March 1999.

[47] Ad9218. Technical report, Analogue Devices, July 2001. Annotation Note available on Web: http://www.analogue.com/technology/dataConverters/designTools.

[48] APEX 20K. Technical report, ALTERA, February 2002.

[49] N. Berger. Development of a z-Vertex Trigger based on Drift Chamber Signals at H1. Master's thesis, Eidgenössische Technische Hochschule Zürich, 2002.

[50] Veikko Karimaki. Effective Circle Fitting for Particle Trajectories. *Nucl. Instrum. Meth.*, A305:187–191, 1991.

[51] J. Naumann. *Entwicklung und Test der dritten H1-Triggerstufe.* PhD thesis, Universität Dortmund, 2003.

[52] D. Sankey. Personal communication.

[53] J. Samson. θ Fit in the FTT. Talk at FTT meeting, 2001.

[54] A. Schöning. Description of the L1 Linker. 2002. FTT Internal Note.

[55] Implementing High-Speed Search Applications with Altera CAM. Technical report, ALTERA, July 2001. Annotation Note 119.

[56] A. Schöning and Y. H. Fleming. Talk in FTT meeting, 2002.

[57] A. Schöning. Personal communication.

[58] R. Baldinger. Personal communication.

[59] A. Schöning. Description of the FTT Merging Scheme. April 2003. FTT Internal Note.

[60] S. A. Baird et al. A Fast Track Trigger with High Resolution for H1. 1999. Proposal submitted to the Physics Research Committee, DESY internal report PRC 99/06 and addendum PRC 99/07.

[61] Alan D. Martin, W. James Stirling, and R. G. Roberts. Parton Distributions Updated. *Phys. Lett.*, B306:145–150, 1993.

[62] Torbjörn Sjöstrand. High-Energy Physics Event Generation with PYTHIA 5.7 and JETSET 7.4. *Comput. Phys. Commun.*, 82:74–90, 1994.

[63] B. List. Diffractive J/ψ-Produktion in Elektron-Proton-Stössen am Speicherring HERA. Master's thesis, Technische Universität Berlin, 1993.

[64] D. Hoffmann. *Zwei-Elektron-Ereignisse im H1-Detektor.* PhD thesis, Universität Hamburg, 2000.

[65] X. Janssen. *Electroproduction diffractive de mésons Rho à HERA.* PhD thesis, Université Libre de Bruxelles, 2003.

[66] Torbjörn Sjöstrand and Mats Bengtsson. The Lund Monte Carlo for Jet Fragmentation and e^+ e^- Physics: JETSET version 6.3 - An Update. *Comput. Phys. Commun.*, 43:367, 1987.

[67] H1 collaboration. Guide to Simulation Program, H1SIM. H1 Internal Note H1-01/97-509, January 1997.

[68] R. Brun et al. GEANT3 User's Guide. CERN Report CERN-DD/EE/84-1, 1996.

[69] S. Peters. PhD thesis, Universität Hamburg, 1992. MPI-PhE/92-13.

[70] M. Rudowicz. PhD thesis, Universität Hamburg, 1992. MPI-PhE/92-14.

[71] R. L. Gluckstern. Uncertainties in Track Momentum and Direction, due to Multiple Scattering and Measurement Errors. *Nucl. Instrum. Meth.*, 24:381–389, 1963.

[72] U. Amaldi, editor. *Study of an $e-p$ Facility in Europe*, 1979. DESY ECFA 79/48.

[73] W. Buchmüller and G. Ingelmann, editors. *Physics at HERA*, 1992.

[74] H-C. Schultz-Coulon. Personal communication, 2002.

[75] O. Behrendt. Entwicklung von Algorithmen zur Identifikation von Vektormeson Ereignissen mit dem neuen H1 Spurtrigger. Master's thesis, Universität Dortmund, 2002.

[76] Ursula Bassler and Gregorio Bernardi. On the Kinematic Reconstruction of Deep Inelastic Scattering at HERA: The Σ Method. *Nucl. Instrum. Meth.*, A361:197–208, 1995.

[77] J. C. Bizot et al. Pure LAr Calorimeter L2TT Trigger Elements. July 1999. H1 Internal Note H1-07/99-574.

[78] T. Carli et al. Proposal to Upgrade the LAr Calorimeter Trigger. January 1999. H1 Internal Note H1-01/99-560.

[79] B. Heinemann. *Measurement of Charged Current and Neutral Current Cross Sections in Positron-Proton Collisions at sqrt(s)=300 GeV*. PhD thesis, Universität Hamburg, 2003.

[80] R. Lipsett, C. F. Schäfer, and C. Ussery. *VHDL: Hardware Description and Design*. Kluwer Academic Publishers: Boston/Dortrecht/London, September 2001.

Acknowledgements

I would like to thank all the people that have made this Ph.D possible. I would like to thank my supervisor Dr. Paul Newman for his continued support and advice. Although he currently is the Physics Coordinator for the H1 Experiment, he found time to discuss my progress and answer my physics questions. I would also like to thank the "Meister", Dr. André Schöning, for the support and advice he has given me during the design and implementation of the FTT-L1 Fast Track Trigger. I am also grateful for the office space that I was provided with by the ETH Zürich during the time I was working on the FTT track segment finding algorithm. This improved the communication between everyone involved on the project, which was very helpful. I would like to thank Dr. Ian Kenyon for the support he gave me, especially for arranging some further financial support during the first half of my fourth year.

I had the opportunity to stay out in Hamburg for most of my PhD. This was mainly due to the fact that my supervisor was permanently out at DESY. This enabled me to enjoy the great city of Hamburg for a little longer.

I would also like to thank my friends for the enjoyable time here in Hamburg. The FTT group included Nick Berger, Raphael Baldinger, Simon Baumgartner, Christoph Wissing, Olaf Behrendt and Jürgen Naumann. We always found some places to have some nice food. Especially the Greek restaurant "Kypros" and the cocktail bar "Bolero's" were on our favourite list.

Not to forget, the long nights in Hamburg ending up on the "Fischmarkt" and the grilling evenings on the beach together with my English mates, Dave South, Matt Beckingham, Paul Laycock, Nick Malden, Ethan Woehrling, Oliver Henshaw and Yves Coppens. It was always good to be out with the English crowd. Although the time I spend with them was far from just being filled with physics discussions, the latter kept me in touch with the Physics side of the H1 experiment. I would also like to thank Christian Veelken for the nice atmosphere in the Liverpool office, where I spent my last year to perform my trigger studies.

Finally, I would like to thank my family for their support throughout the last four years.